

Probing cold gas with Mg II and Ly α radiative transfer

Seok-Jun Chang^{1*} and Max Gronke¹

¹ *Max-Planck-Institut für Astrophysik, Karl-Schwarzschild-Straße 1, 85748 Garching b. München, Germany*

Accepted 2024 July 1. Received 2024 June 25; in original form 2023 July 14

ABSTRACT

The Mg II resonance doublet at 2796 Å and 2803 Å is an increasingly important tool to study cold, $T \sim 10^4$ K, gas – an observational driven development requiring theoretical support. We develop a new Monte Carlo radiative transfer code to systematically study the joined Mg II and Ly α escape through homogeneous and ‘clumpy’ multiphase gas with dust in arbitrary 3D geometries. Our main findings are: (i) The Mg II spectrum differs from Ly α due to the large difference in column densities, even though the atomic physics of the two lines are similar. (ii) the Mg II escape fraction is generally higher than that of Ly α because of lower dust optical depths and path lengths – but large variations due to differences in dust models and the clumpiness of the cold medium exist. (iii) Clumpy media possess a ‘critical covering factor’ above which Mg II radiative transfer matches a homogeneous medium. The critical covering factors for Mg II and Ly α differ, allowing constraints on the cold gas structure. (iv) The Mg II doublet ratio R_{MgII} varies for strong outflows/inflows ($\gtrsim 700 \text{ km s}^{-1}$), in particular, $R_{\text{MgII}} < 1$ being an unambiguous tracer for powerful galactic winds. (v) Scattering of stellar continuum photons can decrease R_{MgII} from two to one, allowing constraints on the scattering medium. Notably, we introduce a novel probe of the cold gas column density – the halo doublet ratio – which we show to be a powerful indicator of ionizing photon escape. We discuss our results in the context of interpreting and modeling observations as well as their implications for other resonant doublets.

Key words: radiative transfer – scattering – line: formation – galaxies: haloes galaxies: high-redshift

1 INTRODUCTION

The circumgalactic medium (CGM) plays a pivotal role in understanding galaxy formation and evolution. As an extended gaseous region surrounding galaxies, it serves as a bridge between the intergalactic medium and the galactic disk, facilitating the exchange of matter, energy, and feedback processes. Exploring the properties and dynamics of the CGM provides crucial insights into the mechanisms governing star formation, chemical enrichment, and the regulation of galactic outflows, ultimately shaping the growth and evolution of galaxies over cosmic time (see extensive reviews Tumlinson et al. 2017; Faucher-Giguere & Oh 2023).

Traditionally, the CGM has been studied using absorption lines, which involve observing the light from a bright background source passing through the CGM and absorbing specific wavelengths (Prochaska et al. 2013; Crighton et al. 2015; Bouché et al. 2016; Chen et al. 2020; Weng et al. 2023). This usually constrains knowledge to singular sight lines and thus requires stacking to assemble a comprehensive picture of the CGM. However, recent advancements in observational techniques and instrumentation have opened up new avenues for studying the CGM using emission instead (Steidel et al. 2010, 2011; Hennawi & Prochaska 2013; Leclercq et al. 2022; Dutta et al. 2023). One main advantage over the traditional absorption line approach is that the spatial information, such

as the surface brightness profile and spatially varying spectral shapes, allows us to infer the physical properties of the CGM without a need for a background source.

In both emission as well as absorption line studies, metal resonance doublet lines play a crucial role. The absorption features of the doublets in the quasar spectrum (e.g., Fox et al. 2007, 2009; Mas-Ribas et al. 2017; Schroetter et al. 2021; Ranjan et al. 2022) and the emission feature near the quasars and star-forming galaxies (e.g., Arrigoni Battaia et al. 2015; Hayes et al. 2016; Berg et al. 2019; Guo et al. 2020; Travascio et al. 2020; Leclercq et al. 2022; Dutta et al. 2023) have been utilized to study the kinematics and physical properties of CGM. Importantly, metal resonance doublets trace different temperature regions because of their different ionization energies. For instance, the doublet Mg II at 2796 Å and 2803 Å traces the cold medium with $T \lesssim 10^4$ K, because the ionization energy of Mg II (~ 15.0 eV) is comparable to that of H I (~ 13.6 eV). The doublets of atoms with high ionization energy > 60 eV, C IV $\lambda\lambda 1548, 1551$, N V $\lambda\lambda 1239, 1243$, O VI $\lambda\lambda 1032, 1038$, and Si IV $\lambda\lambda 1393, 1402$ trace the warm medium with $T \gtrsim 10^5$ K. The absorption lines of these metal doublets coincide in the quasar spectrum with strong Lyman- α (Ly α) absorption. The coexistence of high and low ionized absorption lines shows the multiphase structure of CGM in one line of sight (Churchill & Charlton 1999; Schroetter et al. 2021, see also Tumlinson et al. 2017).

* E-mail: sjchang@mpa-garching.mpg.de

Apart from its fundamental role as the fuel of (future) star

formation, studying the cold gas with $T = 10^4$ K is also crucial in order to understand the epoch of reionization in the early universe. This is because cold H I structures prevent the majority of ionizing photons to escape from galaxies and to reionize the intergalactic medium.

At high- z , Ly α – as the most prominent emission line – serves as a valuable tracer of cold gas due to its resonant nature, which allows the imprinting of physical properties on the observed Ly α line (see reviews by [Dijkstra 2014](#); [Dijkstra et al. 2019](#); [Ouchi et al. 2020](#)). One important example of such an imprint is the separation of Ly α peaks correlating with the neutral hydrogen column density ([Adams 1972](#); [Neufeld 1990](#)). It has, thus, been suggested that a narrow peak separation is an indication for Lyman continuum (LyC) escape $f_{\text{esc,LyC}}$ ([Verhamme et al. 2015](#); [Dijkstra et al. 2016](#); [Izotov et al. 2018a](#); [Flury et al. 2022b](#)). However, observing a clear Ly α spectrum becomes challenging at higher $z \gtrsim 4$ due to extinction by the neutral intergalactic medium (IGM) ([Laursen et al. 2011](#); [Byrohl & Gronke 2020](#); [Kulkarni et al. 2019](#); [Hayes et al. 2021](#); [Smith et al. 2022](#)). Moreover, at $z < 2$, the observed wavelength of Ly α is in Far-UV regime < 3000 Å, necessitating the use of the Hubble Space Telescope (HST) for Ly α observations.

To overcome the limitations of Ly α , the Mg II doublet emission is spotlighted as a promising new tool for studying the cold CGM. Like Ly α , the resonant nature of the Mg II doublet allows it to carry information about the cold medium ([Prochaska et al. 2011](#); [Henry et al. 2018](#); [Katz et al. 2022](#)). The Mg II emission undergoes less extinction by the neutral IGM than Ly α due to its small Mg II fraction (approximately $10^{-4.5}$ in solar metallicity). Because the vacuum wavelength of Mg II doublet emission is near 2800 Å, ground-based observations can capture Mg II at $0.1 < z < 2$, and it at $z > 6$ can be observable via the James Webb Space Telescope (JWST). Observations of the Mg II halo have already been made at $z < 2$ ([Rubin et al. 2011](#); [Rickards Vaught et al. 2019](#); [Zabl et al. 2021](#); [Burchett et al. 2021](#)).

The advent of integrated field spectrographs (IFS) such as MUSE (Multi Unit Spectroscopic Explorer; [Bacon et al. 2010](#)), KCWI (Keck Cosmic Web Imager; [Martin et al. 2010](#)), and HETDEX (Hobby-Eberly Telescope Dark Energy Experiment; [Hill et al. 2021](#)) allows us the study extended regions spatially resolved in emission. Notably, many studies have been carried out using Ly α ([Steidel et al. 2010](#); [Cantalupo et al. 2014](#); [Wisotzki et al. 2016, 2018](#); [Cai et al. 2019](#); [Arrigoni Battaia et al. 2019](#); [Li et al. 2021](#); [Lujan Niemeyer et al. 2022a,b](#); [González Lobos et al. 2023](#)) but more recently, also spatially resolved Mg II emission nebulae have been observed through IFS ([Chisholm et al. 2020](#); [Zabl et al. 2021](#); [Burchett et al. 2021](#); [Leclercq et al. 2022](#); [Dutta et al. 2023](#); [Guo et al. 2023b](#)).

Previous studies have explored the properties of Mg II in conjunction with Ly α and LyC to leverage Mg II as an analog of Ly α and a tracer of $f_{\text{esc,LyC}}$. [Chisholm et al. \(2021\)](#) proposed the doublet ratio of Mg II as a tracer of $f_{\text{esc,LyC}}$ at $z > 6$ using the JWST. These previous studies highlight the potential of Mg II as an analog of Ly α for probing the properties of the cold CGM. [Henry et al. \(2018\)](#) conducted simultaneous observations of Ly α and Mg II spectra in Green Pea galaxies at $z \sim 0.2 - 0.3$ to examine the relationship between the two lines. They discovered a linear correlation between the escape fractions of Ly α and Mg II, accompanied by a broad-

ening and redshifting of the Mg II spectrum at lower escape fractions. Furthermore, they established that the Mg II doublet ratio, represented by the ratio of Mg II $\lambda 2796$ to $\lambda 2803$, is contingent on $f_{\text{esc,LyC}}$ (also see [Chisholm et al. 2020](#); [Seive et al. 2022](#); [Izotov et al. 2022](#); [Xu et al. 2023](#)). Galaxies with low $f_{\text{esc,LyC}}$ exhibited a Mg II doublet ratio below 2, while the ratio approached 2 in cases with high $f_{\text{esc,LyC}}$. In a separate investigation, [Katz et al. \(2022\)](#) tested a method of measuring $f_{\text{esc,LyC}}$ using the doublet ratio post-processing a cosmological simulation. They highlighted the effectiveness of this method for optically thin Mg II lines in galaxies and proposed Mg II emission as an intriguing probe for studying galaxy kinematics at higher redshift in JWST observations.

Radiative transfer (RT) models that incorporate the scattering processes of metal resonance doublets are essential to interpret observational data correctly. While the study of Ly α radiative transfer has a long history (e.g. [Ahn et al. 2001, 2002](#); [Zheng & Miralda-Escudé 2002](#); [Hansen & Oh 2006](#); [Verhamme et al. 2006](#); [Duval et al. 2014](#); [Gronke et al. 2017](#); [Seon & Kim 2020](#); [Byrohl & Nelson 2022](#); [Chang et al. 2023](#)), less attention has been paid to other resonant lines. Previous work often employs Sobolev’s approximation ([Sobolev 1960](#); [Yoo et al. 2002](#); [Kasen et al. 2002](#)), which assumes large velocity gradients in the flow and generally is challenging to implement in complex geometries. A full treatment of Mg II and Fe II fluorescence lines was studied in [Prochaska et al. \(2011\)](#) through a Monte-Carlo RT method, focusing on a homogeneous, outflowing media. More recently, [Michel-Dansac et al. \(2020\)](#) presented a versatile, 3D Monte Carlo radiative transfer of resonant lines concentrating on post-processing cosmological simulations.

In this paper, we want to focus on the resonant line transfer of Mg II and Ly α in simplified, homogeneous, as well as multiphase geometries. This approach allows us to closely study the physics shaping observables, ultimately helping us to link them to physical quantities while at the same time circumventing convergence issues galactic and cosmological simulations usually suffer from (e.g., [Faucher-Giguère et al. 2010](#); [van de Voort et al. 2019](#); [Hummels et al. 2019](#)). For this purpose, we develop a new 3D radiative transfer simulation code – dubbed `RT-scat` – which can be used for Mg II and other resonance doublets. It is in parts based on the Ly α RT simulation code presented in [Seon et al. \(2022\)](#); [Chang et al. \(2023\)](#).

This paper is constructed as follows. In § 2, we describe the physics of radiative transfer, the method of our Monte Carlo simulation, and the geometry of our model, which consists of a spherical scattering medium surrounding a point emission source. § 3 and § 4 present the simulated results of homogeneous and multiphase media, respectively, considering monochromatic light and in situ Gaussian emission. In these sections, we perform a comparative analysis of the radiative transfer of Mg II and Ly α , focusing on their spectral profiles and escape fractions. In § 5, we study the scattering of the stellar continuum near Mg II doublet. Furthermore, we investigate the doublet ratio of Mg II $\lambda 2796$ and $\lambda 2803$ considering in situ Mg II emission and the continuum. In § 6, we discuss the implications of the results obtained from our Mg II and Ly α radiative transfer simulations. Finally, § 7 succinctly summarizes the main conclusions.

2 RADIATIVE TRANSFER FOR Mg II DOUBLET

Our simulation code for the Mg II resonance doublet RT-*scat* is based on the 3D Ly α Monte-Carlo radiative transfer code used previously in [Chang et al. \(2023\)](#) and *LaRT* used, e.g., in [Seon & Kim \(2020\)](#); [Seon et al. \(2022\)](#). Since the atomic structure of metal resonance doublets is identical to the hydrogen atomic fine structure of Ly α , we can easily adapt the atomic physics of Ly α RT to Mg II RT.

The fine structure of Ly α has two transition ($S_{1/2} - P_{1/2}$) and ($S_{1/2} - P_{3/2}$) commonly referred to 'H' and 'K' transitions, respectively. But, the energy difference between them is with $\sim 10^{-4}$ eV, corresponding to ~ 1.5 km s $^{-1}$ velocity separation of K and H transitions, too small to split the lines observationally. However, this effect becomes observable in metal resonant doublets such as Mg II, where the doublet is located at 2796 Å and 2803 Å. Hereafter, we will also refer to the Mg II doublet $\lambda\lambda$ 2796 & 2803 as 'K' & 'H' line, respectively.

We use a 3D grid-based Monte Carlo simulation on a Cartesian coordinate system. In a Monte-Carlo radiative transfer simulation, each photon package corresponds to a certain luminosity and is defined via a current wavelength λ (frequency ν), a position \mathbf{r} , a direction \mathbf{k} and a Stokes vector for polarization $\mathbf{S} = (I, Q, U, V)$. In the simulation, we consider two types of scattering media: homogeneous medium with uniform density and clumpy medium composed of small clumps. Here, we use a uniform density and a constant effective temperature in our 'smooth medium' models or for each clump in our 'clumpy medium' models. In this section, we briefly introduce the atomic physics of Mg II RT, the scattering geometry, and the method of our Monte Carlo simulation.

2.1 Scattering Cross Section

The scattering cross-section of each Mg II line is described by the Voigt profile function, which yields a scattering cross-section for the Mg II doublet

$$\sigma_\nu = \frac{\sqrt{\pi}e^2}{m_e c} \left[\frac{f_K}{\Delta\nu_{D,K}} H(x_K, a) + \frac{f_H}{\Delta\nu_{D,H}} H(x_H, a) \right], \quad (1)$$

where m_e is the electron mass and c is the light speed. $f_K = 0.608$ and $f_H = 0.303$ being the oscillator strengths of the Mg II K and H transitions, respectively. In this equation, $H(x, a)$ is the Voigt-Hjerting function given by

$$H(x, a) = \frac{a}{\pi} \int_{-\infty}^{\infty} \frac{e^{-y^2}}{(x-y)^2 + a^2} dy, \quad (2)$$

where $a = \Gamma/(4\pi\Delta\nu_D)$ is the natural width parameter. The damping constants of the K and H lines are $\Gamma_K = 2.60 \times 10^8$ s $^{-1}$ and $\Gamma_H = 2.57 \times 10^8$ s $^{-1}$, respectively. The dimensionless frequency parameter x is given by

$$x = (\nu - \nu_0)/\Delta\nu_D \quad (3)$$

where $\Delta\nu_D = \nu_0 v_{\text{th}}/c$ is the thermal Doppler width with the thermal velocity $v_{\text{th}} = \sqrt{2k_B T/m_{\text{atom}}}$, and ν_0 are the line center frequencies – which for the K and H lines are $\nu_{0,K} = 1.0724 \times 10^{15}$ s $^{-1}$ and $\nu_{0,H} = 1.0697 \times 10^{15}$ s $^{-1}$, respectively. Throughout the text, we will use x_H and x_K to specify the doublet lines and use $x = x_K$ if not specified. Note that if another random motion component is present, v_{th} be-

comes $\sigma_R = \sqrt{v_{\text{th}}^2 + v_{\text{turbulent}}^2}$. Hereafter, note that σ_R is the random motion component instead of v_{th} .

Fig. 1 shows the scattering cross-sections and curves of growth of Mg II and Ly α (in the left and right panel, respectively). We used $v_{\text{th}} \sim 2.67$ km s $^{-1}$ and 15 km s $^{-1}$ for Mg II and Ly α , i.e., the thermal velocities at $T \sim 10^4$ K, respectively.

In the left panel, we plot the cross sections in velocity space where

$$\Delta V = \left(\frac{v_0}{v} - 1 \right) c \approx -v_{\text{th}} x, \quad (4)$$

where v_0 for Mg II is $\nu_{0,K}$. The right panel of Fig. 1 shows that for a given column density, the equivalent width of Mg II is greater than that of Ly α at the same column density because the cross section of Mg II is larger than that of Ly α at the same thermal velocity since $f_K = 608$ is greater than the Ly α oscillator strength $f_{12} = 0.4162$. However, of course, generally, the Mg II column density N_{MgII} in a H I region is much smaller than N_{HI} . This is because the typical Mg II fraction is $\sim 10^{-5.47}$ (i.e., $n_{\text{MgII}} \sim 10^{-5.47} n_{\text{HI}}$), assuming solar relative abundances with an absolute metallicity of half solar metallicity ([Prochaska et al. 2011](#)); in the solar metallicity, the Mg fraction is $\sim 10^{-4.46}$ ([Holweger 2001](#)). Thus, Mg II photons scatter much less than Ly α photons escaping the same medium.

In this work, we study the Mg II column densities from $10^{11.5}$ to $10^{15.5}$ cm $^{-2}$ corresponding to $N_{\text{HI}} = 10^{17-21}$ cm $^{-2}$. In this N_{MgII} range, an optical depth at the line center τ_0 could be less than 1 at $N_{\text{MgII}} < 10^{12}$ cm $^{-2}$, and wing (Rayleigh) scattering is negligible. On the other hand, τ_0 of Ly α is always much larger than 1 ($\tau_0 > 10^4$) in this N_{HI} range. Therefore, as we will show below, the behavior of Mg II RT is entirely different from that of Ly α RT.

2.2 Geometry

In this study, we focus on three distinct geometries, 'Shell', 'Sphere', and 'Clumpy Sphere'. Fig. 2 shows schematic illustrations of these geometries. In the 'Shell' and 'Sphere' geometries, H I & Mg II atoms are uniformly distributed, and the source is at the center of the halos. The shell geometry consists of a thin H I medium including Mg II with a constant radial speed and a thickness 10% of a halo radius R_{H} . This geometry is widely used for Ly α RT and was shown to reproduce a range of observed Ly α spectral profiles ([Ahn et al. 2002](#); [Verhamme et al. 2006](#); [Dijkstra & Loeb 2008](#); [Gronke & Dijkstra 2016](#)). We adopt the shell geometry with a monochromatic source to test our simulation in § 3.1.

In the sphere geometry, H I & Mg II are distributed in the radius from $0.01R_{\text{H}}$ to R_{H} , and the radial velocity is proportional to the distance from the emission source r ($v(r) = v_{\text{exp}} r/R_{\text{H}}$). The H I & Mg II halos in those geometries are characterized by a H I column density N_{HI} , a Mg II column density $N_{\text{MgII}} = 10^{-5.5} N_{\text{HI}}$, a random motion speed σ_R , a maximum expansion velocity v_{exp} , and a dust absorption optical depth $\tau_{\text{d,abs}}$. In Table 1, we summarize these parameters and their ranges.

We assume the range of v_{exp} in the sphere geometry from -1000 km s $^{-1}$ (inflow) to 1000 km s $^{-1}$ (outflow). When an expansion velocity $v_{\text{exp}} \gtrsim 750$ km s $^{-1}$, which is the velocity separation of Mg II doublet, the Mg II transfer faces that the photons near the K line are scattered by the H transition of

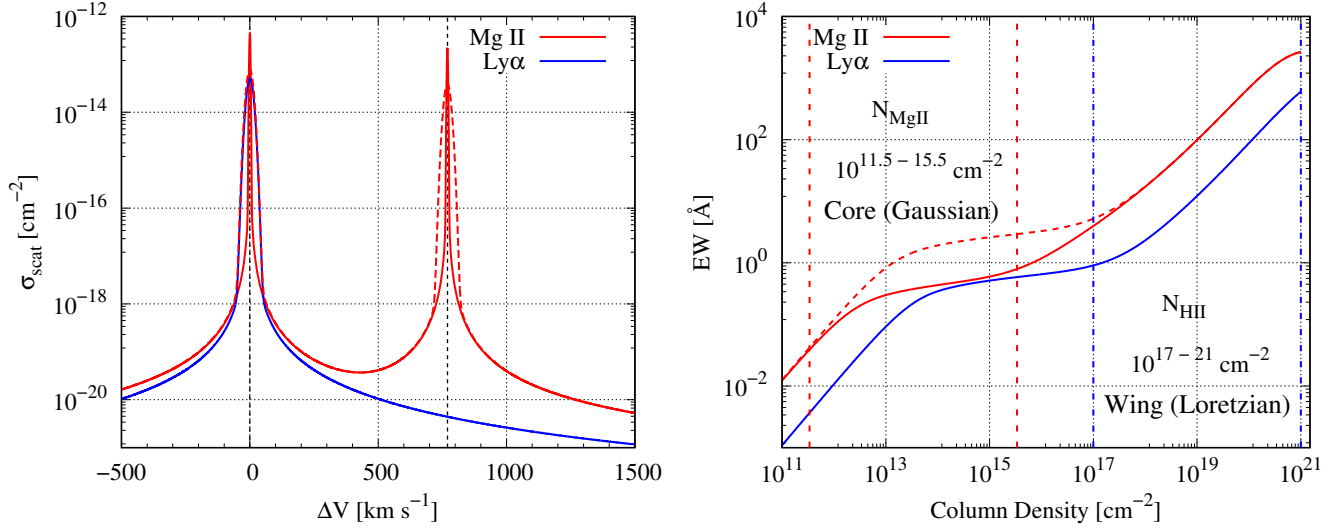


Figure 1. *Left panel:* Scattering cross section of Mg II doublet (red) and Ly α (blue) as a function of the Doppler factor ΔV defined in Eq. (4). The solid and dashed red lines are for $v_{\text{th}} \sim 2.67 \text{ km s}^{-1}$ and 15 km s^{-1} , the thermal velocities of Mg II and H I at temperature $T = 10^4 \text{ K}$, respectively. Note that to the oscillator strength, the scattering cross-section of Mg II is larger than that of Ly α . The black vertical lines in the left panel indicate the line centers of the Mg II K and H lines. *Right panel:* Curve of growth of Mg II and Ly α versus column density. The red and blue vertical lines represent reasonable ranges of Mg II and H I column densities, respectively, assuming solar metallicity. The equivalent width of the Mg II doublet is larger than that of Ly α at the same column density.

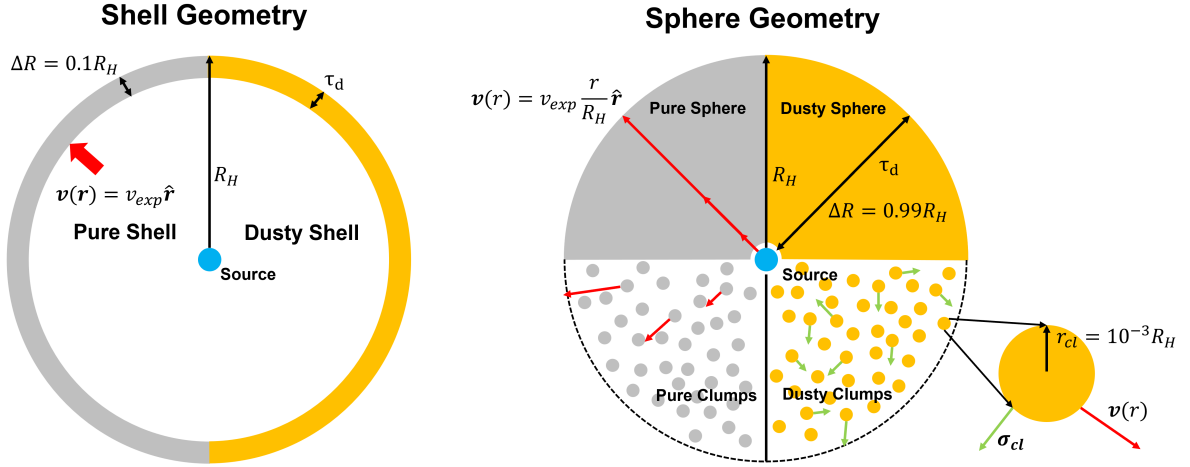


Figure 2. The schematic illustration of ‘Shell’ (left) and ‘Sphere’ (right) geometries. Both models possess a centrally located emission source. In the ‘Shell’ geometry, the Mg II and H I filled region has a thickness of $\Delta R = 0.1 R_H$, where R_H represents the total radius. The radial velocity $v(r)$ and the number density of Mg II & H I are constant. In contrast, the ‘Sphere’ geometry features a thicker H I and Mg II filled region with $\Delta R = 0.99 R_H$. In this case, the radial velocity $v(r)$ is proportional to the distance from the source. The ‘Clumpy Sphere’ (lower half of the right panel) mimics a multiphase system in which cold clumps with size of $10^{-3} R_H$ fill an otherwise empty spherical region with radius R_H . The clumps can exhibit two types of kinematics: an outflow characterized by $v(r)$ and a random motion σ_{cl} . In both models, since the dust-to-gas ratio is fixed, the dust distribution is characterized by a dust optical depth τ_d .

the outflowing medium. Otherwise, H photons are scattered by the K transition in the inflowing medium. In this case, Mg II doublet lines are mixed by scattering, and the ratio of the K and H lines varies. Therefore, we assume an extensive inflow and outflow speed range from 0 to 1000 km s^{-1} , including a speed higher than the line separation of Mg II doublet.

The ‘Clumpy Sphere’ geometry consists of spherical cold

clumps of radius r_{cl} embedded within a spherical region with radius R_H . Apart from the total column density and bulk flow, this setup is characterized by two more parameters, namely a covering factor f_c and a clump’s random motion σ_{cl} . The covering factor f_c is the mean number of clumps in the line of sight from the source to a halo surface. The clump’s random motion σ_{cl} represents a random motion for each clump drawn from a Gaussian probability distribution.

Note that the size of clumps r_{cl} does not affect the radiative transfer process when $r_{\text{cl}} \ll R_{\text{H}}$ – the only important parameter is the mean number of clumps per sightline f_c (Hansen & Oh 2006; Chang et al. 2023). We thus set the clump to halo radius ratio $r_{\text{cl}}/R_{\text{H}} = 10^{-3}$. This value allows us to study and consider the range $f_c = [1, 100]$ in a computationally feasible manner.¹ Since we assume spherical halo and H I clump, the total Mg II column density of the clumpy medium is $\frac{4}{3}f_c N_{\text{MgII,cl}}$ where $N_{\text{MgII,cl}}$ is a clump’s column density. The ranges of these parameters for the clumpy sphere are shown in Table 1. We will discuss Mg II RT in the clumpy medium in § 4.

2.3 Emission Mechanism

The formation of Mg II doublet emission feature is influenced by the intrinsic radiation and the physical properties of the cold gas. The cold gas properties have been studied via the absorption feature of Mg II doublet in QSO spectra (Prochaska et al. 2013; Bouché et al. 2016; Schroetter et al. 2021; Weng et al. 2023). However, the powering mechanism of the intrinsic Mg II emission is still unclear. When Mg II emission mainly originates from collisional excitation of Mg II or recombination of Mg III, the intrinsic profile is a Gaussian with width set by the random motion of the emission region. Also, in this case, the line ratio of Mg II is intrinsically ~ 2 because the statistical weight of $P_{3/2}$ state for the K line is 2 times higher than that of $P_{1/2}$ state for the H line. Alternatively, Mg II can be generated by scattering of stellar continuum near 2800 Å. In this case, the doublet ratio of Mg II is not 2 even though the scattering cross section of the K line is 2 times higher than the H line (Prochaska et al. 2011). The observable information of escaping Mg II photons depends on the density field, kinematics, and physical properties of cold CGM.

Here, we assume three types of the central source,

- (i) a monochromatic case: the source emits line center photons. While this is unrealistic, it helps us understand the basic principles of Mg II transfer. In this case, we use the canonical doublet ratio of 2.
- (ii) a Gaussian case: the intrinsic profile is Gaussian profile with width $\sigma_{\text{src}} = 100 \text{ km s}^{-1}$. Also, in this case, we use an intrinsic doublet ratio of 2.
- (iii) a stellar continuum case: the incident radiation is a flat continuum near Mg II.

In addition, we consider the synthesized source composed of the Gaussian and stellar continuum components, characterized by the equivalent width of the intrinsic Gaussian emission EW_{int} in Section 5.2. The parameters for the source are shown in Table 1.

2.4 Dust Extinction

UV radiation is affected by absorption and scattering by dust grains (Cardelli et al. 1989; Seon & Draine 2016, also see re-

views Mathis 1990; Salim & Narayanan 2020). Our simulation considers dust absorption and scattering adopting the dust scattering phase function in Henyey & Greenstein (1941) and albedo $\alpha_{\text{d}} (= 0.5718 \text{ at } 2800 \text{ \AA} \text{ and } 0.3258 \text{ at } 1216 \text{ \AA})$ adopting the fiducial dust model for the diffuse interstellar medium of the Milky Way described in Draine (2003a,b).

In the calculation, we also consider the contribution of free electrons in the optical constants of graphite, as described in Draine & Lee (1984). We consider one dust property for Mg II doublet at 2796 and 2803 Å because the absorption optical depth of the K and H lines are very similar, with a 0.2% difference between them, and the difference of α_{d} is 0.1 %. Note that in this Milky Way model – and hence in our simulations – the dust absorption optical depth of Ly α is 2.53 larger than for Mg II. The ratio of the dust absorption optical depth of Ly α and Mg II is 3.79 and 9.26 in the LMC and SMC models, respectively. Therefore, a lower metallicity can cause a larger difference in the escape fraction of Ly α and Mg II. As illustrated in Fig. 2, we characterize the dust absorption optical depth for Mg II by $\tau_{\text{d,abs}} = (1 - \alpha_{\text{d}})\tau_{\text{d}}$, where τ_{d} is the dust extinction optical depth. Consequently, in the ‘clumpy’ model, a clump’s dust optical depth in the radius r_{cl} is $3\tau_{\text{d,abs}}/4f_c$ as a clump’s column density $N_{\text{MgII,cl}} = 3N_{\text{MgII}}/4f_c$.

Note that this simplified treatment of dust implies a fixed dust-to-gas ratio per simulation, i.e., perfectly mixed dust into the gas. While this does not represent realistic astrophysical conditions, we focus in this work on the radiative transfer effects only, thus leaving more complex dust structures – which are supported by our simulation framework – for future work. We specify the treatment of dust further in Appendix A.

2.5 Monte Carlo Simulation

Our Monte-Carlo radiative transfer simulation, RT-scatter, follows five steps,

- (i) Initializing the scattering gas geometry and kinematics characterized by the parameters explained in § 2.2 on a 3D Cartesian grid with 200 cells per dimension. For the smooth medium, the physical properties of each cell are determined based on the position of the cell’s center. In the clumpy medium, clumps are randomly generated within each cell, and the physical properties are assigned based on the position of the clump’s center. The medium between clumps is considered empty. The velocity of a clump is determined by random motion and radial velocity. In this simulation, a constant clump radius and clump column density are assumed, although different values can be considered.
- (ii) Generating an initial photon at the central source. The central source emits initial photons isotropically. The number of photons generated depends on the source type. For monochromatic sources, 10^5 photons are generated at the line center. For Gaussian emission, the initial wavelength follows a Gaussian distribution with a width of 100 km s^{-1} . The simulation generates 10^5 and 10^7 photons for the Gaussian emission of Ly α and Mg II doublet, respectively. In the Gaussian and monochromatic cases, the intrinsic Mg II doublet ratio is 2. In the case of a flat continuum for Mg II, 10^8 photons are generated in the velocity range from -2000 km s^{-1} of the K line to $+2000 \text{ km s}^{-1}$ of the H line.
- (iii) Finding a scattering location by considering the cross sec-

¹ Since at fixed f_c , the total number of clumps and the volume filling fraction increase and decrease with decreasing r_{cl} , respectively, the clump radius cannot be too large, while too small values significantly increase the computational cost.

Table 1. Parameters of the spherical geometry (cf. right panel of Fig. 2).

Parameter	Range	Note
N_{MgII}	$10^{11.5-15.5} \text{ cm}^{-2}$	Total Mg II column density
N_{HI}	$10^{17-21} \text{ cm}^{-2}$	Total H I column density
v_{exp}	-1000 km s^{-1} (inflow) – $+1000 \text{ km s}^{-1}$ (outflow)	Maximum expansion velocity
$\tau_{\text{d,abs}}$	0 – 10	Dust absorption optical depth of Mg II
σ_{R}	$2.7^{\dagger} - 30 \text{ km s}^{-1}$	Random velocity of scattering medium
f_{c}^*	1 – 100	Covering factor
σ_{cl}^*	0 – 100 km s^{-1}	Clumps' random velocity
r_{cl}^*	$10^{-3} R_{\text{H}}$ (fixed)	Clump radius
σ_{src}^{**}	0 km s^{-1} (monochromatic) & 100 km s^{-1} (Gaussian)	Width of intrinsic emission
$\text{EW}_{\text{int}}^{**}$	0 (flat continuum) – 100	Intrinsic equivalent width of Mg II emission

\dagger : thermal speed of Mg II at $T = 10^4 \text{ K}$, $*$: used in the clumpy spherical geometry, $**$: parameters describing the emitting source

tions for scattering with the atom (H I or Mg II) and dust as a function of frequency. First, a dimensionless free path of the photon, $\tau_f = -\ln r_u$, is generated, where r_u is a uniform random number between 0 and 1. The simulation then converts the free path to a physical distance to determine the location of the next scattering event. In the smooth medium, when the photon passes through a cell, ν is fixed at the frequency in the rest frame of the cell. The physical distance is computed based on the physical properties of each cell. Using the rest frame wavelength, the total scattering cross section σ_{tot} is the sum of the cross sections for scattering with H I or Mg II, σ_{ν} (as described in Eq. (2.1)), and the dust cross section, σ_{dust} (explained in § 2.4). In the case of the clumpy medium, the simulation identifies the closest clump in the direction of the photon and computes the free path assuming the wavelength in the rest frame of the clump and considering the sub-grid geometry.

- (iv) Computing the frequency ν , direction \mathbf{k} , and Stokes vector \mathbf{S} of the scattered photon. After determining the scattering position, the simulation selects which type of scattering the photon undergoes using a uniform random number. The computation of \mathbf{k} and \mathbf{S} for scattered Ly α photons, considering the $S_{1/2} - P_{1/2}$ and $S_{1/2} - P_{3/2}$ transitions, is described in Section 2.2 of Chang et al. (2023). Since the atomic structure of Ly α and Mg II doublet are identical, the scattering phase function for Ly α is used in Mg II scattering in our simulation. The computation of these vectors for dust-scattered photons is explained in Section 2.6 of Seon et al. (2022).
- (v) Repeatedly executing steps (iii) and (iv) until the photon breaks free from the 3D grid. Once it escapes, ν is converted to the frequency in the observed frame. The simulation collects the escaping photon for further analysis. After that, a new initial photon is continuously generated until the total number of photons generated so far is less than the total number specified in step (ii).

3 RESULTS: SMOOTH MEDIUM

In this section, we present our numerical results in a smooth medium with two types of sources: a monochromatic light and an in situ Gaussian emission with the width $\sigma_{\text{src}} = 100 \text{ km s}^{-1}$. Regarding the geometries considered, in § 3.1, we investigate the monochromatic light case in a shell geometry to test our simulation and compare it with analytic solutions. Additionally, we consider a spherical geometry in § 3.1

and § 3.2, for both monochromatic and Gaussian emission sources, respectively. In all cases, the intrinsic doublet ratio of Mg II K and H lines is fixed to the fiducial value of 2. We investigate the formation of the spectral profile of Mg II lines, the escape fraction, and the doublet ratio of escaping Mg II photons. We also compare Mg II and Ly α radiative transfer under the same physical conditions.

3.1 Monochromatic Source

In order to study Mg II radiative transfer, we first focus on the most simplified conditions and assume a shell geometry with a central point source emitting monochromatic light with frequencies at the line center of the Mg II K and H lines. Fig. 3 shows Mg II spectra of the static shell for three random velocities of the scattering medium $\sigma_{\text{R}} = 2.7, 15, \text{ and } 30 \text{ km s}^{-1}$ and various $N_{\text{MgII}} = 10^{11.5-15.5} \text{ cm}^{-2}$. Note that for illustration purposes, the spectra shown in Fig. 3 are composed of only scattered photons and normalized to the peak flux value.

The top panels of Fig. 3 show that the spectrum becomes broader with increasing N_{MgII} . At $N_{\text{MgII}} \lesssim 10^{11.5} \text{ cm}^{-2}$, both profiles of Mg II doublet converge to a single Gaussian with width σ_{R} because the optical depth at the line center τ_0 is less than unity. In the bottom panels, the profiles become broadened with more substantial flux at the line center as σ_{R} increases.

As discussed in § 2.1 (Fig. 1), Mg II transfer differs from Ly α transfer because of the different range of Mg II and H I column densities and consequently very different optical depths. In the case of Ly α , the extremely high optical depth leads to a double peaked spectrum with zero flux at the line center (see the gray dashed line in the left bottom panel of Fig. 3). On the other hand, Mg II spectra show non-zero flux at the line center due to much lower optical depth as compared to Ly α .

In the following sections, we show (1) a comparison between the simulation results and analytic solutions, (2) the escape fraction of Mg II dusty media, and (3) the doublet ratio of Mg II.

3.1.1 Simulation Comparing with Analytic Solution

We compare the simulated results of the shell geometry without dust and analytic solutions from the literature (Osterbrock 1962; Adams 1972; Neufeld 1990). In Fig. 4, we show three values of the Mg II K line (from top to bottom panel):

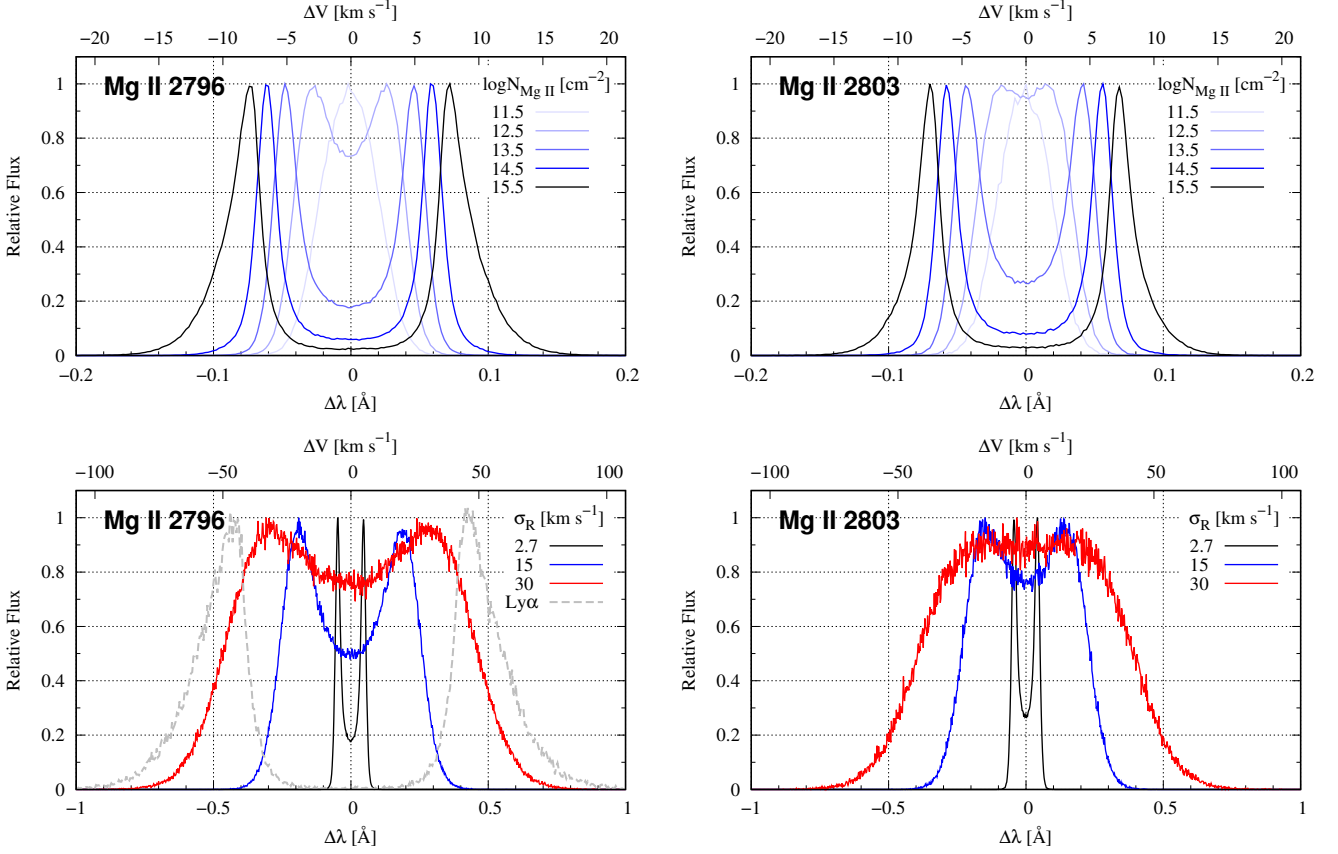


Figure 3. Mg II spectra of scattered photons in a static shell geometry with monochromatic emission. The left panel corresponds to the Mg II λ 2796 (K line), while the right panel represents the Mg II λ 2803 (H line). The top panel shows the spectrum for various Mg II column densities N_{MgII} at $\sigma_{\text{Ran}} = 2.7 \text{ km s}^{-1}$. The bottom panel displays the spectrum for various random speeds σ_{Ran} at $N_{\text{MgII}} = 10^{13.5} \text{ cm}^{-2}$. The gray dashed line in the left bottom panel represents the Ly α spectrum of the static medium with the monochromatic light at an H I column density $N_{\text{HI}} = 10^{18} \text{ cm}^{-2}$. The Mg II spectrum broadens as N_{MgII} or σ_{Ran} increase.

the fraction of directly escaping photons (the fraction of escaping photons without scattering), the peak separation of double peaked spectra, and the mean number of scattering N_{scat} as a function of N_{MgII} for $\sigma_{\text{R}} = 2.7, 15, \text{ and } 30 \text{ km s}^{-1}$. In the top panel, the direct escape fraction decreases with increasing N_{MgII} because more photons experience scattering. In the middle and bottom panels, the profiles of ΔV_{peak} and N_{scat} (solid lines) are comparable to analytic solutions (dashed lines). Note that here the escaping frequency (here expressed as velocity) v_{esc} is simply given by $\tau_{\nu} = N_{\text{MgII}}\sigma_{\nu} = 1$ where σ_{ν} is the scattering cross section following a Voigt profile Eq. (1).

In the bottom panel of Fig. 4, the numerical results of N_{scat} follow the analytic solution, given by $N_{\text{scat}} = 1/\text{erfc}(v_{\text{esc}}/v_{\text{th}})$ (Osterbrock 1962; Neufeld 1990). In summary, two statistical values from our simulation in the shell model, ΔV_{peak} and N_{scat} , closely match the analytic solutions.

Note that these solutions imply that the photon escapes via a single long flight and, hence, are also applicable to Ly α radiative transfer but only for low/intermediate optical depths ($a\tau_0 \lesssim 1$, i.e., $\tau_0 \lesssim 2 \times 10^4$ or $N_{\text{HI}} \lesssim 10^{17} \text{ cm}^{-2}$ for $T \sim 10^4 \text{ K}$). For more common optical depths, Ly α photons escape via consecutive wing-scatterings, also known as ‘excursion’ (Adams 1972).

3.1.2 Escape fraction f_{esc}

The escape fraction of Mg II depends on how much dust the photons encounter on their escape path and, thus – as in Ly α – primarily on the dust content but also on the Mg II column density N_{MgII} , the kinematics, and the structure of the gas.

Fig. 5 shows the escape fraction f_{esc} of the K line as a function of dust absorption optical depth $\tau_{\text{d,abs}}$ in a homogeneous medium. One obvious trend is that f_{esc} decreases with increasing $\tau_{\text{d,abs}}$. In the left panel, we show f_{esc} for various $N_{\text{MgII}} = 10^{11.5-15.5} \text{ cm}^{-2}$. If the incident photons experience only dust absorption, the profile of f_{esc} is equivalent to the simple dust extinction curve $\exp(-\tau_{\text{d,abs}})$. However, one can note from Fig. 5 that f_{esc} profiles are usually steeper than this dust extinction function (shown as the black dotted line). This is because a larger N_{MgII} leads to more scatterings and a longer path length l_{path} of each photon to escape from the scattering medium.

Fig. 6 illustrates this point further and shows the average path length the photons travel in the scattering medium l_{path} of the emergent Mg II K line in a dust-free medium in units of the physical thickness of scattering medium $\Delta R = R_o - R_i$. The longer l_{path} , the greater the dust extinction the photon

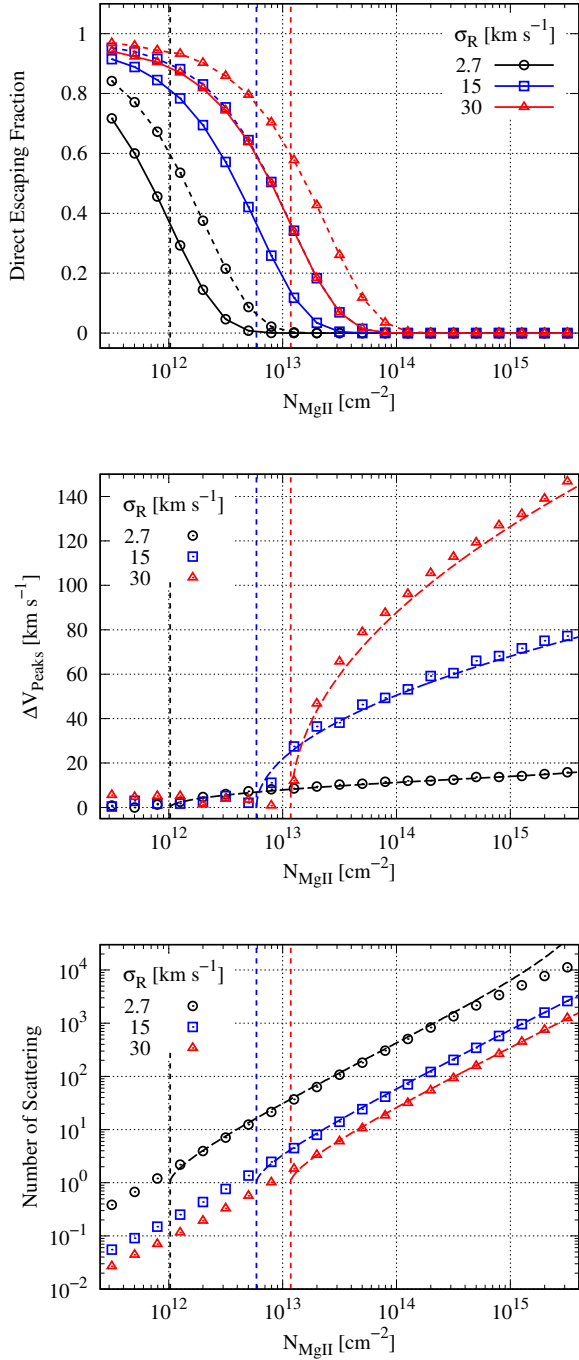


Figure 4. The fraction of directly escaping photons (top), velocity offset of the spectral peaks ΔV_{peak} (middle), and the number of scattering N_{scat} (bottom) of the Mg II K line as a function of Mg II column density N_{MgII} , in the shell model with the monochromatic source. The vertical dashed lines denote the K line center optical depths of unity. The solid and dashed lines in the top panel represent the direct escape fraction of the K and H lines, respectively. The colors of the lines represent the thermal motion of scattering medium $\sigma_{\text{Ran}} = 2$ (black), 15 (blue), and 30 (red). The dashed lines in the middle and bottom panels are the analytic solutions of ΔV_{peak} and N_{scat} , respectively. The dashed lines in these panels represent the analytic solutions for ΔV_{peak} and N_{scat} , respectively. Overall, the simulated values closely follow the analytic solutions,

experiences. Hence, f_{esc} decreases with increasing N_{MgII} at the same $\tau_{\text{d,abs}}$ – as seen in Fig. 5.

The left panel of Fig. 5 shows that the profile of f_{esc} is similar to the simple dust extinction curve $\exp(-\tau_{\text{d,abs}})$ at low N_{MgII} ($\sim 10^{11.5} \text{ cm}^{-2}$) and $\tau_{\text{d,abs}} < 1$. However, even though most photons escape without Mg II scattering at this low N_{HI} , overall f_{esc} in $\tau_{\text{d,abs}} > 1$ is smaller than $\exp(-\tau_{\text{d,abs}})$. Due to the fact that our simulation considers dust scattering and absorption together, multiple dust scatterings occur in the medium with $\tau_{\text{d,abs}} > 1$. These multiple dust scatterings cause a longer path length through the dusty medium, and thus $f_{\text{esc}} < \exp(-\tau_{\text{d}})$. In conclusion, an increased dust optical depth decreases the escape fraction in two ways: by directly destroying the Mg II photons and by increasing the path length of escaping photons.

Interestingly, for column densities $N_{\text{MgII}} > 10^{14} \text{ cm}^{-2}$, the escape fraction f_{esc} does not depend on N_{MgII} as shown in the left panel of Fig. 5 where f_{esc} for $N_{\text{MgII}} = 10^{14.5}$ and $10^{15.5} \text{ cm}^{-2}$ are identical. In this high N_{MgII} regime ($\tau_0 > 10$), the initial monochromatic light must experience numerous scatterings to escape the scattering medium and has a longer l_{path} . However, Fig. 6 shows the profile of l_{path} for the static shell case (black solid line) becomes flattened near $N_{\text{MgII}} \sim 10^{15} \text{ cm}^{-2}$. As N_{MgII} increases in this high N_{MgII} regime, a free path for each Mg II scattering gets shorter; the free path near the line center is $\sim \tau_0^{-1}$. Hence, the total path length slightly increases due to the short free path. We expect that the f_{esc} profile does not depend on N_{MgII} before N_{MgII} reaches the value ($> 10^{17} \text{ cm}^{-2}$), which is enough for the Lorentzian part of Voigt profile to be optically thick like Ly α RT.

The central panel of Fig. 5 shows f_{esc} for three random velocities $\sigma_{\text{R}} = 2.7, 15, \text{ and } 30 \text{ km s}^{-1}$. We find that f_{esc} at $N_{\text{MgII}} = 10^{13.5} \text{ cm}^{-2}$ increases with increasing σ_{R} at the same $\tau_{\text{d,abs}}$ – but the dependence on σ_{R} is negligible at larger column densities $N_{\text{MgII}} = 10^{15.5} \text{ cm}^{-2}$. This is supported by Fig. 6, where the path lengths through the scattering medium l_{path} for $\sigma_{\text{R}} = 2.7 \text{ km s}^{-1}$ (black curves) is longer than those at $\sigma_{\text{R}} = 30 \text{ km s}^{-1}$ (blue curves) at $N_{\text{MgII}} < 10^{15} \text{ cm}^{-2}$. l_{path} for $\sigma_{\text{R}} = 2.7 \text{ km s}^{-1}$ and $= 30 \text{ km s}^{-1}$ are similar at $N_{\text{MgII}} 10^{15.5} \text{ cm}^{-2}$.

In the right panel of Fig. 5, we show that f_{esc} in and out-flowing medium is greater than that of the static medium. This is simply because, for the considered monochromatic source, most atoms are out of resonance and do not interact with the medium; in other words, the path length l_{path} is ~ 1 (cf. Fig. 6. This short l_{path} due to an outflow medium leads to less interactions with dust and aids the escape of Mg II photons. Specifically, Fig. 6 shows that overall l_{path} for out-flowing cases is $\sim 3\Delta R$ which is 5–7 times smaller than that for static cases at $N_{\text{MgII}} = 10^{15.5} \text{ cm}^{-2}$.

In addition to the effects described above, the geometry of the scattering medium also affects the escape fraction f_{esc} . The right panel of Fig. 5 shows that in the static case, the escape fraction from a shell geometry is smaller than that of a filled sphere. This is because the width of the shell is much smaller than its radius. Hence, the escape through the shell model is similar to a semi-infinite slab where (straight) crossing sightlines can, in principle, intercept the slab for an infinite distance. This is different in the spherical model, where the maximum crossing path length from the central source to the surface is equal to the sphere’s radius. This effect was

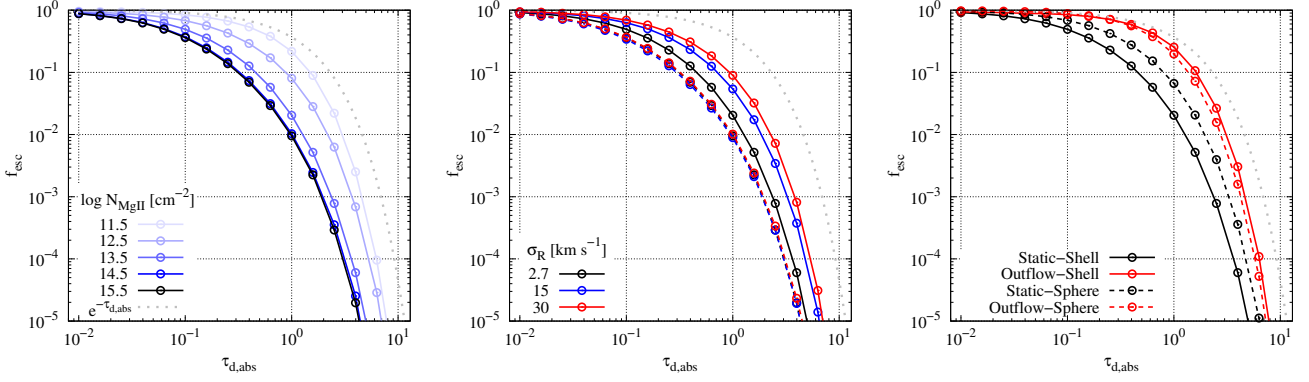


Figure 5. Escape fractions f_{esc} of Mg II as a function of dust absorption optical depth $\tau_{\text{d,abs}}$ for various N_{MgII} (left), random motion speed σ_{R} (center), kinematics-geometry (right panel). The gray dotted lines are a simple dust extinction curve $\exp(-\tau_{\text{d,abs}})$. *Left:* f_{esc} profiles of static shell geometry in the range of $N_{\text{HI}} = 10^{11.5}$ to $10^{15.5} \text{ cm}^{-2}$. The shades of blue represent different N_{MgII} values. *Center:* f_{esc} profiles for three $\sigma_{\text{R}} = 2.7$ (black), 15 (blue), and 30 (red). The solid and dashed lines correspond to two distinct N_{MgII} values: $10^{13.5}$ and $10^{15.5} \text{ cm}^{-2}$, respectively. *Right:* f_{esc} profiles of static and outflowing media at $N_{\text{MgII}} = 10^{13.5} \text{ cm}^{-2}$. ‘Static’ and ‘Outflow’ represent $v_{\text{exp}} = 0$ and 10 km s^{-1} , respectively. The solid and dashed lines are for the shell and sphere geometry, respectively.

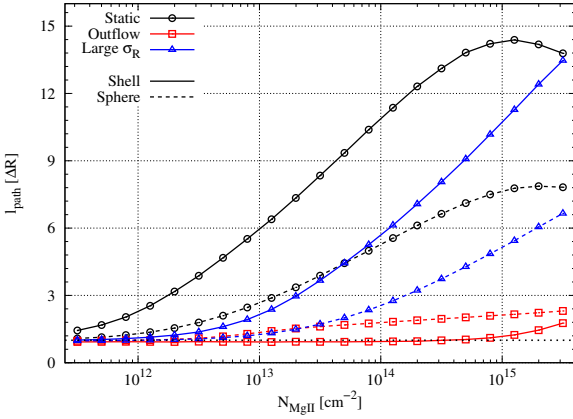


Figure 6. The path length l_{path} of escaping Mg II K photons as a function of N_{MgII} in a unit ΔR , which is $0.1R_{\text{H}}$ and $0.99R_{\text{H}}$ in the shell (solid) and sphere (dashed line) geometries, respectively. The black and red lines are identical to the ‘static’ and ‘outflow’ cases in the right panel of Fig. 5. The blue lines represent a static case with $\sigma_{\text{R}} = 30 \text{ km s}^{-1}$. In the static cases, l_{path} of the shell geometry is longer than that in spherical geometries (cf. Adams 1975). In outflowing cases, the sphere geometry has a longer path due to the different velocity distributions of the scattering medium.

studied in (Adams 1975) in detail and numerically again, e.g., in (Seon & Kim 2020, ; see their Appendices B & C).

However, for the outflowing cases, this order is reversed, and f_{esc} in the sphere is slightly smaller than in the shell. This is because the radial velocity $v(r)$ is constant in the shell and proportional to the distance from the source in the sphere. Thus, in the shell, the monochromatic light becomes quickly optically thin because the shell has only one radial velocity, whereas, in the sphere, several photons of monochromatic light can be scattered by the slowly moving inner halo. Fig. 6 also shows this effect through the small difference of l_{path} of the outflowing shell (red solid) and sphere (red dashed).

3.1.3 Mg II doublet ratio

The previous section shows that the escape fraction f_{esc} depends on a Mg II column density N_{MgII} at the same dust absorption optical depth $\tau_{\text{d,abs}}$ due to variations in the path length through the dusty medium l_{path} . A longer l_{path} leads to a decreased f_{esc} because the escaping photons get more chance to be absorbed by dust. Since the scattering cross section of Mg II K is twice that of the H line, l_{path} of the K line can be larger than l_{path} for the H line. Thus, the doublet ratio of Mg II can decrease in a dusty medium. To understand this effect, we clearly define the doublet ratio of Mg II K and H lines R_{MgII} . Generally, the Mg II doublet ratio of the Mg II emission case

$$R_{\text{MgII}}^{\text{E}} = \frac{\int_{\lambda_{\text{K}} - \Delta\lambda_{300}}^{\lambda_{\text{K}} + \Delta\lambda_{300}} F(\lambda) d\lambda}{\int_{\lambda_{\text{H}} - \Delta\lambda_{300}}^{\lambda_{\text{H}} + \Delta\lambda_{300}} F(\lambda) d\lambda} \quad (5)$$

where $F(\lambda)$ is the Mg II spectrum as a function of a wavelength, $\lambda_{\text{K,H}}$ is the line center wavelength of Mg II K,H line, and $\Delta\lambda_{300} \sim 2.8 \text{ \AA}$ is the wavelength shift corresponding to 300 km s^{-1} . Indeed, if the Mg II K and H lines can not be mixed via scattering processes, the doublet ratio can become the ratio of the escaping fraction. Hence, as we set the intrinsic doublet ratio of the K and H line emission to its canonical value of 2, the doublet ratio of the monochromatic light case is given by

$$R_{\text{MgII}}^{\text{E}} = \frac{2f_{\text{esc,K}}}{f_{\text{esc,H}}}, \quad (6)$$

where $f_{\text{esc,K}}$ and $f_{\text{esc,H}}$ are escape fractions of Mg II K and H lines, respectively.

Fig. 7 shows examples of this behavior. It displays R_{MgII} profiles as a function of N_{MgII} in the same setups as shown in Fig. 5. As expected, R_{MgII} decreases with increasing $\tau_{\text{d,abs}}$ at $N_{\text{MgII}} < 10^{13} \text{ cm}^{-2}$ since K line photons experience more dust absorption than H line photons. Also, expected for the same reason is the decreasing trend of R_{MgII} with increasing column density for $N_{\text{MgII}} > 10^{13} \text{ cm}^{-2}$. However, for larger column densities, this trend is reversed, and there is a characteristic minimum in the Mg II doublet ratio at the line

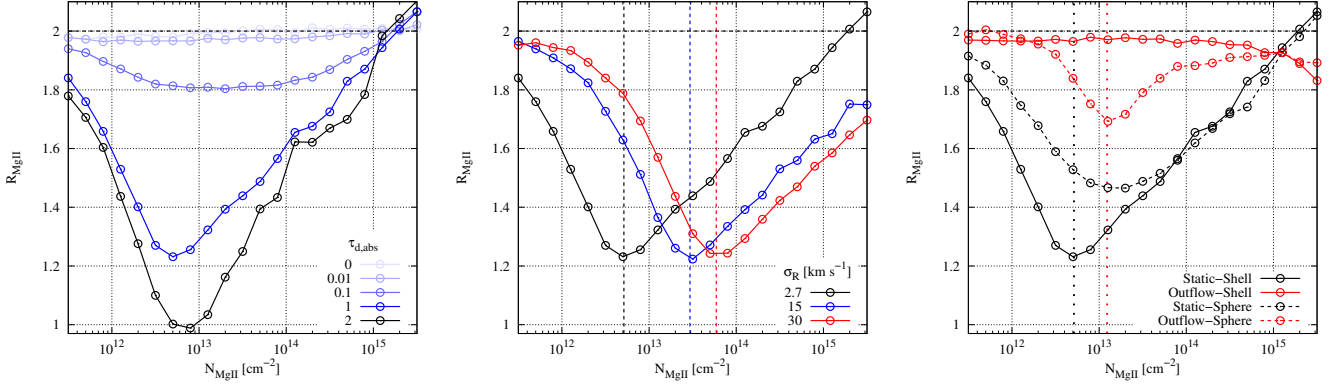


Figure 7. The Mg II doublet ratio R_{MgII} of the monochromatic light case as a function of N_{MgII} for various $\tau_{\text{d,abs}}$ (left), σ_{R} (center), and kinematics-geometry (right). The left panel displays R_{MgII} for the static shell with $\tau_{\text{d,abs}} = 0$ (dust free) – 2. (since f_{esc} is too small to be observed for $\tau_{\text{d,abs}} > 2$; cf. Fig. 5). The central panel shows R_{MgII} for three different σ_{R} while $\tau_{\text{d,abs}} = 1$ is fixed. The vertical dashed lines in the corresponding color represent $\tau_0 = 5$. The right panel shows R_{MgII} of static and outflowing media and highlights the differences between the shell and the sphere geometries while $\sigma_{\text{R}} = 2.7 \text{ km s}^{-1}$ is fixed. The vertical dotted lines indicate $\tau_0 = 5$ (black) and 12 (red). For $\tau_{\text{d,abs}} \geq 1$, R_{MgII} depends on N_{MgII} . As N_{MgII} increases, R_{MgII} decreases up to a specific optical depth ($\tau_0 \approx 5$). For larger column densities, R_{MgII} increases again.

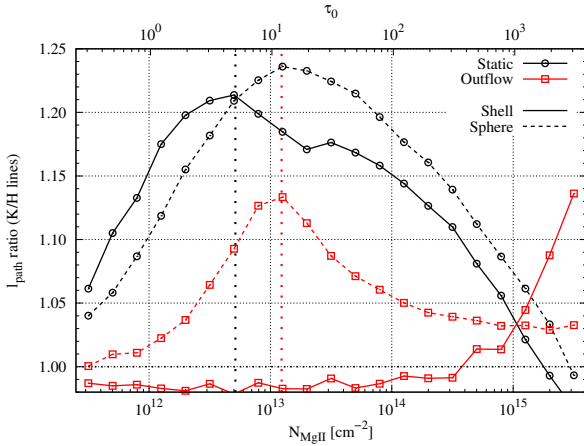


Figure 8. The ratio of l_{path} of Mg II K and H photons for a static/outflowing medium in the shell/sphere geometry. The vertical dashed lines represent $\tau_0 = 5$ (black) and 12 (red) as the dashed lines in the right panel of Fig. 7.

center optical depth of the K line $\tau_0 \approx 5$ (corresponding to $N_{\text{MgII}} \approx 10^{13} \text{ cm}^{-2}$).

The central panel of Fig. 7 shows R_{MgII} for three σ_{R} in the static medium versus the column density. The minimum R_{MgII} exists at the vertical dashed lines representing the value of N_{MgII} for $\tau_0 = 5$ of different σ_{R} . The right panel shows R_{MgII} for the static and outflow cases of the shell and sphere. Also, the dip of R_{MgII} profiles of the static shell lies at the vertical lines for $\tau_0 = 5$.

To understand R_{MgII} profile near $\tau_0 = 5$, Fig. 8 shows the ratio of the path lengths of Mg II K and H lines as a function of N_{MgII} . The peak of the ratio of l_{path} of the static shell appears at the vertical black dotted line. For the static sphere case, this peak is slightly shifted to $\tau_0 = 12$ (marked with the red vertical dotted line in Fig. 8). This is because the escape path l_{path} in the sphere is generally shorter than that of the

shell – as seen in the left panel of Fig. 6 and discussed in §3.1.2.

For $\tau_0 < 1$ corresponding to $N_{\text{MgII}} < 10^{12} \text{ cm}^{-2}$, both of Mg II lines are optically thin, and most photons directly escape without scattering; $l_{\text{path}} \sim 1$ and the ratio of $l_{\text{path}} \sim 1$. Thus, the difference of l_{path} between two lines is too small to affect the interaction with dust.

For $\tau_0 \gg 1$ ($N_{\text{MgII}} > 10^{15} \text{ cm}^{-2}$), both of Mg II lines are optically thick, and all photons must experience multiple scatterings before escaping; $l_{\text{path}} > 10$. But, in this high N_{MgII} regime, the profile of l_{path} versus N_{MgII} flattens as seen in Fig. 6. Hence, in this case, the factor of 2 difference between the cross section of the K and H lines is negligible. Consequently, l_{path} of the two lines are similar (cf. Fig. 8).

Only in the intermediate regime, $\tau_0 \sim 5$, the two times larger scattering cross section makes a notable difference in the l_{path} ratio. It is also noteworthy that in this regime, the doublet ratio of Mg II lines R_{MgII} strongly depends on $\tau_{\text{d,abs}}$ (cf. left panel in Fig. 7).

For an outflowing medium, we find that the doublet ratio R_{MgII} is very different. The right panel of Fig. 7 shows the profiles of R_{MgII} for static and outflow cases. The profiles R_{MgII} of the outflow case are flat in the shell and have a minor dip in the spherical case. As shown in Fig. 6, in the outflowing shell case, $l_{\text{path}} \sim 1$ regardless of N_{MgII} . Because of constant radial velocity, all monochromatic light directly escapes. In the outflowing sphere case, the inner sphere with a slowly outflowing medium causes the monochromatic light to scatter. However, the optical depth of this inner halo is smaller than the total optical depth τ_0 . If the source is not monochromatic, the variation of R_{MgII} in the outflowing medium becomes significant. We will discuss it in the following sections using Gaussian emission.

3.2 Gaussian Source

In this section, we simultaneously run the simulation for Ly α and Mg II in the smooth spherical geometry. We adopt the

Gaussian profiles as incident radiation for Ly α and Mg II doublet with the same intrinsic width $\sigma_{\text{src}} = 100 \text{ km s}^{-1}$. The random speed of the scattering medium σ_{R} is fixed at the thermal speed with $T = 10^4 \text{ K}$, $\sim 2.7 \text{ km s}^{-1}$, and 14 km s^{-1} for Mg II and H I media, respectively. The ratio of Mg II and H I column densities $N_{\text{MgII}}/N_{\text{HI}}$ is fixed at $10^{-5.5}$ following solar metallicity. Even though the atomic physics affecting the radiative transfer for Mg II and Ly α are alike, we will see that the results of the two lines are not similar due to the very different column densities in the neutral medium. The following sections compare spectra and escape fractions of Mg II and Ly α . Furthermore, we show the doublet ratio of Mg II for various N_{MgII} and expansion velocities v_{exp} .

These different ranges of the Mg II and H I column densities lead to very different scattering effects. As $N_{\text{HI}} > 10^{19} \text{ cm}^{-2}$, the Lorentzian part of the scattering cross section ($\Delta V > 3v_{\text{th}}$), starts becoming optically thick (see the left panel of Fig. 1). This leads to multiple Ly α scattering even though the wavelength of the incident photon is far from the line center.

On the other hand, in the range of $N_{\text{MgII}} = 10^{11-16} \text{ cm}^{-2}$, the Lorentzian part is always optically thin for Mg II photons. This means that only photons in the Gaussian part ($\Delta V \lesssim 3v_{\text{th}}$) of the rest frame of an Mg II atom undergo scattering. Because of these two very different scattering behaviors and thus different escape paths, comparing emergent Mg II and Ly α observables can lead to additional insights into the physical parameters of the scattering medium (see § 6 where we discuss this further).

3.2.1 Mg II & Ly α spectra

Fig. 9 shows the emergent spectra of Mg II and Ly α for various column densities, N_{MgII} and N_{HI} , at an expansion velocity $v_{\text{exp}} = 200 \text{ km s}^{-1}$. The right panel shows the total integrated Ly α spectra for various $N_{\text{HI}} = 10^{18-21} \text{ cm}^{-2}$. The Ly α spectrum becomes more extended and redshifted with increasing N_{HI} ; the spectral peaks move to the redward. However, Mg II spectra for $N_{\text{MgII}} = 10^{12.5-15.5} \text{ cm}^{-2}$ (shown in the left panel of Fig. 9) possess absorption-like features in the blueward part of the spectrum and the steep asymmetric profile redwards. Also – as opposed to the Ly α spectra – the spectral peak is always at the line center.

It is noteworthy that for $N_{\text{MgII}} \leq 10^{13.5} \text{ cm}^{-2}$, the H and K lines of the emergent Mg II spectra differ. Specifically, the blue absorption features of the K line are roughly two times stronger than that of the H line due to the larger cross-section of the K line. Also, some blueward photons can directly escape because of the low optical depth at the line center $\tau_0 \leq 1$. But, at in the high $N_{\text{MgII}} \geq 10^{14.5} \text{ cm}^{-2}$ regime, the spectra of K and H lines are nearly identical because τ_0 of both lines $\gg 1$ akin to Ly α transfer. Consequently, those spectra are very similar to the Ly α spectrum with $N_{\text{HI}} = 10^{18} \text{ cm}^{-2}$.

In summary, Mg II transfer for large N_{MgII} is analogous to Ly α transfer for the low N_{HI} , leading to similar spectral shapes in Mg II H and K lines. On the other hand, for lower N_{MgII} , the absorption features of the K and H lines differ.

Fig. 10 shows the Mg II (Ly α) spectra for four expansion velocities $v_{\text{exp}} = 100, 200, 500,$ and 1000 km s^{-1} at $N_{\text{MgII}} = 10^{15.5}$ ($N_{\text{HI}} = 10^{21} \text{ cm}^{-2}$). The left panel shows that Mg II spectra for $v_{\text{exp}} = 100-500 \text{ km s}^{-1}$ are very similar on the redward side because here, most photons directly escape from

the source. The blueward side, however, shows absorption features from $-v_{\text{exp}}$ to 0 km s^{-1} .

In the right panel of Fig. 10, the Ly α spectra show a very different trend with varying v_{exp} . Here, the red wing is more extended and red-shifted with increasing v_{exp} . This trend continues even to very large outflow velocities. For the Mg II spectrum, this is very different. For the largest outflow velocity shown ($v_{\text{exp}} = 1000 \text{ km s}^{-1}$), the spectrum is composed of a weak K line and a strong H line. This is because if the outflow velocity is stronger than the peak separation of the Mg II doublet $\sim 750 \text{ km s}^{-1}$, the K line photons can be scattered by the H transition, leading to a redistribution near the K line.

Thus, the scattering of the H transition in the strong outflow can suppress the flux of the K line. For that reason, the doublet ratio of Mg II decreases with increasing the outflow velocity, especially $v_{\text{exp}} > 750 \text{ km s}^{-1}$. Otherwise, in the case of an inflowing medium, the doublet ratio increases with increasing inflow velocity. We will measure the doublet ratio and discuss it in § 3.2.3.

Dust affects Mg II spectra in a different way compared to Ly α . Fig. 11 shows the spectra of Mg II (Ly α) for three dust optical depths $\tau_{\text{d,abs}} = 0, 0.1,$ and 1.0 at $N_{\text{MgII}} = 10^{14.5} \text{ cm}^{-2}$ ($N_{\text{HI}} = 10^{20} \text{ cm}^{-2}$). The spectra at $\tau_{\text{d,abs}} = 0.1$ are similar to those from the dust free medium ($\tau_{\text{d,abs}} = 0$). At $\tau_{\text{d,abs}} = 1$, the spectral profile of Ly α has a less extended red wing. This is because the photons in the red wing of the spectrum, on average, undergo more scatterings with atomic hydrogen, thus have a longer path length, and are more likely to be absorbed by dust. Therefore, the strength of the red extended wing decreases with increasing $\tau_{\text{d,abs}}$.

This picture is reversed for Mg II (shown in the left panel of Fig. 11). Here, the red wing of at $\tau_{\text{d,abs}} = 1$ is stronger than at $\tau_{\text{d,abs}} = 0.1$. This is because, without dust, the red part of the Mg II spectrum is mainly composed of directly escaping photons. As the dust scattering does not strongly depend on the wavelength in the range of several tens of Å, all the escaping photons can be scattered by outflowing dust forming a red wing² Importantly, note that this effect cannot be observed if a radiative transfer simulation does not consider dust scattering.

3.2.2 Escape fractions of Mg II and Ly α

The Mg II escape fraction of monochromatic light depends on both the column density and the kinematics because of the Mg II scattering effects discussed in the previous section. But with a width of the intrinsic profile $\sigma_{\text{src}} \gg$ the random speed of scattering medium σ_{R} in a static medium, most initial photons escape without any Mg II scattering, and the path length of these escaping photons is $\sim R_{\text{H}}$.

Fig. 12 shows $f_{\text{esc,MgII}}$ and $f_{\text{esc,Ly}\alpha}$, escape fractions of Mg II doublet and Ly α , respectively. The top panel shows $f_{\text{esc,MgII}}$ in a static medium which follows $\exp(-\tau_{\text{d,abs}})$ since only a small fraction of photons near the line center experience scatterings with Mg II atoms. Consequently, the $f_{\text{esc,MgII}}$ profile does not depend on the Mg II column density N_{MgII} .

In a smooth medium, the escape fraction of Ly α is always

² For very low column densities $N_{\text{HI}} < 10^{17} \text{ cm}^{-2}$, Ly α spectra show a similar trend (not shown here).

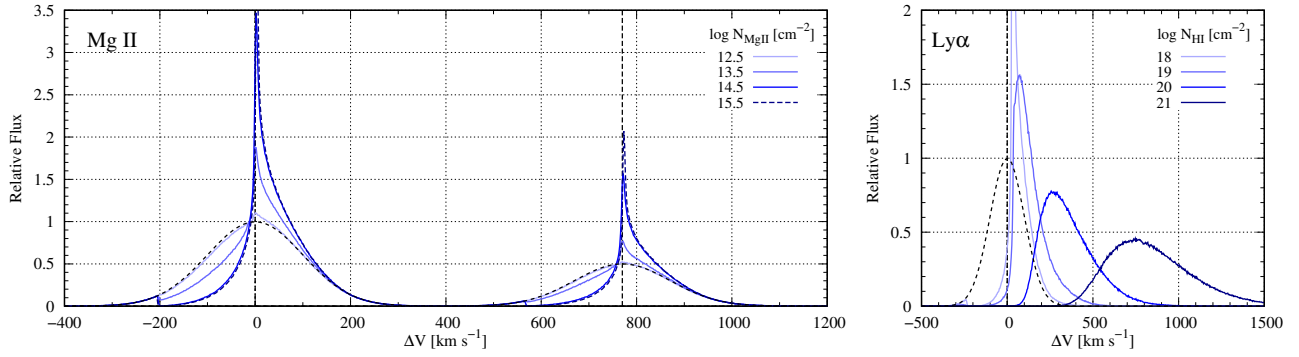


Figure 9. The spectra of Mg II (left) and Ly α (right) for various Mg II & H I column densities at $v_{\text{exp}} = 200 \text{ km s}^{-1}$. The dashed black lines represent the intrinsic Gaussian profile. Note that in the left panel, the Mg II spectra for $N_{\text{MgII}} = 10^{14.5}$ (blue) and $10^{15.5} \text{ cm}^{-2}$ (dashed dark blue) are nearly identical.

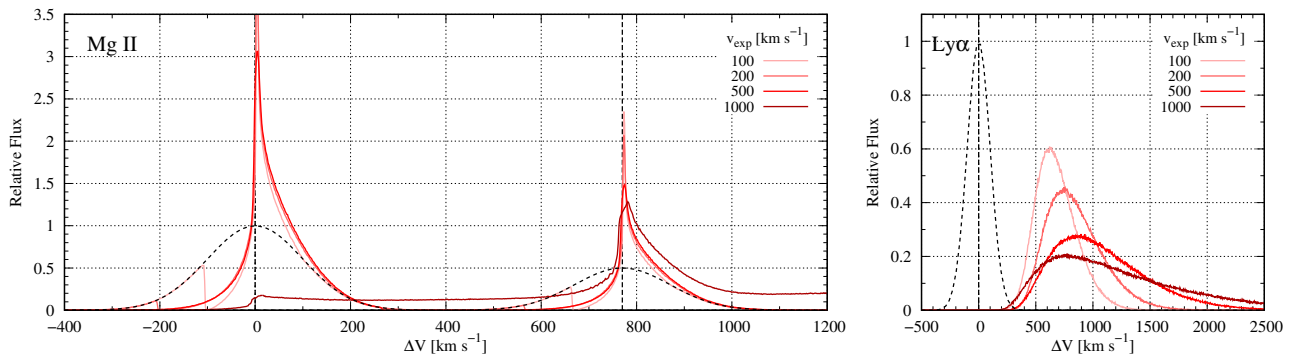


Figure 10. The spectra of Mg II (left) and Ly α (right) for various expansion velocities v_{exp} at $N_{\text{MgII}} = 10^{15.5} \text{ cm}^{-2}$ and $N_{\text{HI}} = 10^{21} \text{ cm}^{-2}$, respectively.

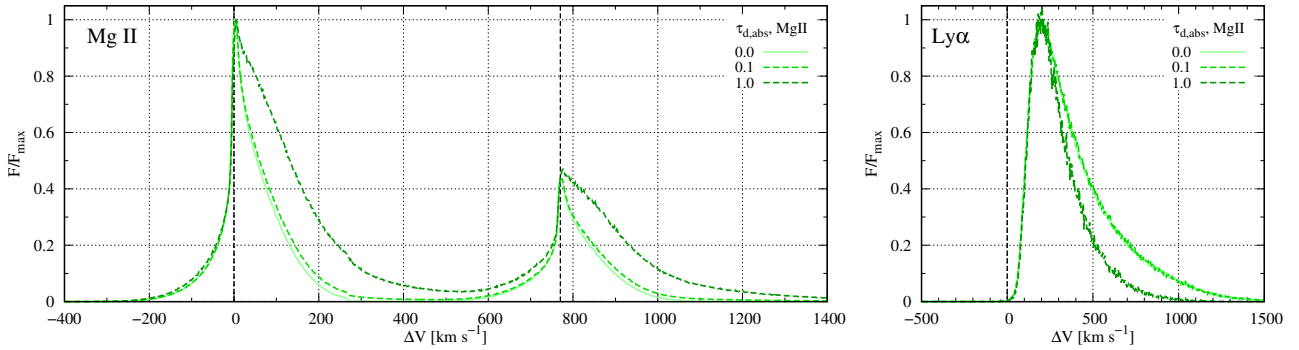


Figure 11. The normalized spectra of Mg II (left) and Ly α (right) for various dust optical depth $\tau_{\text{d,abs}}$ at $N_{\text{MgII}} = 10^{14.5} \text{ cm}^{-2}$ ($N_{\text{HI}} = 10^{20} \text{ cm}^{-2}$) and $v_{\text{exp}} = 500 \text{ km s}^{-1}$. The solid line is the spectrum of the dust free medium ($\tau_{\text{d,abs}} = 0$). The green dashed lines represent the spectra from the dust medium at $\tau_{\text{d,abs}} = 0.1$ and 1.0 . The spectrum is the total integrated spectra divided by the peak value. The spectra of Mg II (Ly α) at $\tau_{\text{d,abs}} = 1$ show a stronger (weaker) red wing compared to the dust-free case.

smaller than that of Mg II for two reasons. Firstly, $\tau_{\text{d,abs}}$ of Ly α is ~ 2.53 times higher than that of Mg II. Secondly, $N_{\text{HI}} \gg N_{\text{MgII}}$ causes more scatterings and a longer path length. The top panel of Fig. 12 shows that $f_{\text{esc,Ly}\alpha}$ decreases with increasing N_{HI} . In the high column density regime ($N_{\text{HI}} \geq 10^{18} \text{ cm}^{-2}$), Ly α photons experience multiple scatterings – even if the photon’s intrinsic wavelength is in the Lorentzian part of the cross section. This scattering process increases

the path length of Ly α photons significantly. Thus, unlike for Mg II, the dependence on the column density is not negligible for Ly α radiative transfer due to the different range of column densities between N_{HI} and N_{MgII} in astrophysical systems.

Even without radiative transfer effects (i.e., for extremely low column densities $N_{\text{HI}} < 10^{17} \text{ cm}^{-2}$), the different dust cross sections and corresponding $\tau_{\text{d,abs}}$ values cause a large difference between Ly α and Mg II escape fractions

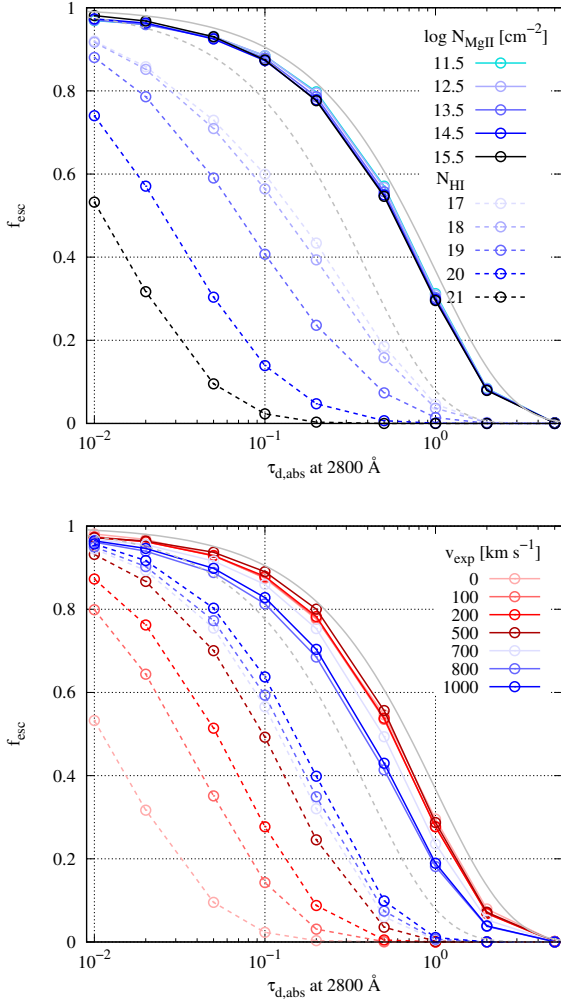


Figure 12. Escape fractions f_{esc} of Mg II (solid) and Ly α (dashed lines), $f_{\text{esc,MgII}}$ and $f_{\text{esc,Ly}\alpha}$, in the smooth medium versus the dust absorption optical depth at 2800Å, $\tau_{\text{d,abs}}$. In the top panel, each line color represents various column densities, and v_{exp} is fixed at 0 km s $^{-1}$. In the bottom panel, the color corresponds to various v_{exp} while N_{MgII} (N_{HI}) is fixed at $10^{15.5}$ cm $^{-2}$ (10^{21} cm $^{-2}$). The solid and dashed gray lines are the simple dust extinction function $\exp(-\tau_{\text{d,abs}})$ for Mg II and Ly α , respectively. Overall, the dashed line is smaller than the solid line since the dust optical depth of Ly α is 2.53 times higher than that of Mg II. The profile of $f_{\text{esc,Ly}\alpha}$ strongly depends on v_{exp} and N_{HI} . The profile of $f_{\text{esc,MgII}}$ only slightly varies, with changing v_{exp} and N_{MgII} .

as illustrated in Fig. 12. In this figure, we consider the Milky Way dust model where the dust cross section for Ly α is 2.53 times larger than the one for Mg II. However, it is noteworthy that this ratio can be significantly larger in other dust models. In the dust model of the Small and Large Magellanic Clouds (SMC and LMC, respectively) the ratios are 3.79 and 9.26, respectively (Draine 2003a,b). In these models, the Ly α escape fraction becomes significantly smaller. We explore the different dust models in Appendix A.

The bottom panel of Fig. 12 shows $f_{\text{esc,MgII}}$ and $f_{\text{esc,Ly}\alpha}$ for various expansion velocities v_{exp} at fixed column densities $N_{\text{MgII}} = 10^{15.5}$ cm $^{-2}$ and $N_{\text{HI}} = 10^{21}$ cm $^{-2}$. We find that

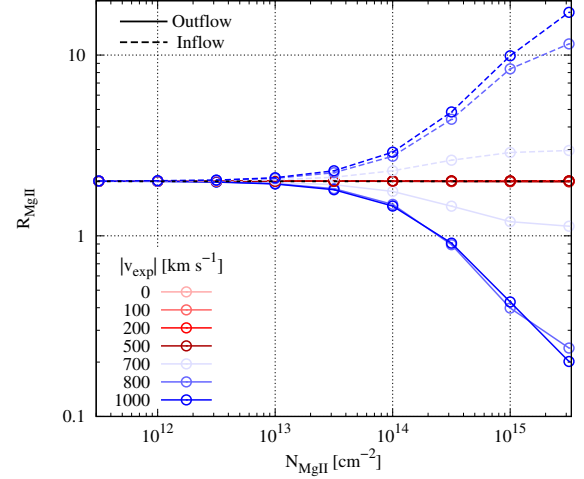


Figure 13. The Mg II doublet ratio R_{MgII} of the Gaussian emission case for various v_{exp} . The solid and dashed lines represent outflow and inflow cases, respectively.

$f_{\text{esc,MgII}}$ in $v_{\text{exp}} > 700$ km s $^{-1}$ becomes $\sim 10\%$ smaller compared to lower outflow velocities and that the dependence on v_{exp} is negligible in the low v_{exp} regime. In this high v_{exp} regime, the outflowing medium induces scatterings of the K photons in both the blueward and redward by H transition, thus increasing their path length in the exposure to dust. Note that for an inflowing medium with similar absolute velocities $v_{\text{exp}} < -700$ km s $^{-1}$, this difference decreases to $\sim 5\%$ due to the intrinsic doublet ratio of Mg II of 2. This dependence on v_{exp} becomes imperceptible as $N_{\text{MgII}} < 10^{13}$ cm $^{-2}$.

In the bottom panel of Fig. 12, we confirm that $f_{\text{esc,Ly}\alpha}$ increases with increasing expansion velocity v_{exp} .³ This is because the rapidly moving medium induces a large Doppler shift to the scattering photons, which escape easily with a short path length. Note, however, that even for the highest outflow velocities ~ 1000 km s $^{-1}$, $f_{\text{esc,Ly}\alpha}$ is still lower than the simple dust extinction function $\exp(-\tau_{\text{d,abs}})$ because the large column density $N_{\text{HI}} = 10^{21}$ cm $^{-2}$ makes the H I region optically thick over $\Delta V \pm 1000$ km s $^{-1}$ (see the left panel of Fig. 1). This dependence on v_{exp} becomes weaker as N_{HI} decreases and for $N_{\text{HI}} < 10^{19}$ cm $^{-2}$ and large outflow velocities $|v_{\text{exp}}| > 700$ km s $^{-1}$ $f_{\text{esc,Ly}\alpha}$ follows $\exp(-\tau_{\text{d,abs}})$.

3.2.3 Mg II doublet ratio

As shown in Fig. 10, Mg II K and H photons can be mixed by the strong outflow or inflow medium ($|v_{\text{exp}}| > 700$ km s $^{-1}$). To investigate the behavior of these mixed photons by scattering processes, we measure the doublet ratio R_{MgII} of the Mg II spectra adopting Eq. 5. Fig. 13 shows the doublet ratio of the Gaussian emission case as a function of N_{MgII} for

³ Here, we consider only an outflowing medium ($v_{\text{exp}} > 0$ km s $^{-1}$) but note that $f_{\text{esc,Ly}\alpha}$ of an inflowing medium with the same absolute velocity is identical.

various v_{exp} . The doublet ratio R_{MgII} is invariant for bulk velocities $|v_{\text{exp}}| < 700 \text{ km s}^{-1}$ regardless of other parameters. At $v_{\text{exp}} > 700 \text{ km s}^{-1}$ and $N_{\text{MgII}} > 10^{13.5} \text{ cm}^{-2}$, R_{MgII} decreases with increasing v_{exp} and N_{MgII} because the strong outflow allows the K line photons to be scattered by the H line transition. In the strong inflow case, $v_{\text{exp}} < -700 \text{ km s}^{-1}$, R_{MgII} increases with decreasing v_{exp} and N_{MgII} ; H line photons move to the blueward of the K line as shown in Fig. 10. As a result, R_{MgII} can vary by resonance scattering at $v_{\text{exp}} > 700 \text{ km s}^{-1}$.

4 CLUMPY MEDIUM

4.1 Scattering processes in clumpy medium

Resonant line transfer through a multi-phase clumpy medium is fundamentally different than through a single-phase smooth medium. The main reason for this is that while in a homogeneous medium, photons can escape through ‘excursion’ or ‘single-flight’ (as discussed above), in a clumpy medium, a third form of escape via ‘random walk’ between the dense clumps exists (Neufeld 1991; Gronke et al. 2017). The main additional parameter controlling radiative transfer effects in a clumpy medium is the mean number of clumps per line of sight f_c (Hansen & Oh 2006).

This implies, for instance, that a clumpy medium can enhance the Ly α escape fraction due to the so-called surface scattering effect (Neufeld 1991; Hansen & Oh 2006 but see, e.g., Laursen et al. 2013; Duval et al. 2014). This effect occurs in the multi-phase clumpy medium when the hot inter-clump medium is optically thin or empty, the cold clumps are optically thick ($\tau_{\text{cl}} \gg 1$), and relatively few clumps exist (see below for an exploration of the transition in a clumpier medium). If these conditions are fulfilled, the photons cannot penetrate the clumps. Instead, they undergo several scatterings merely on the surface of the clump. In that case, the Ly α photons escape from the clumpy medium through a shorter path length within the cold gas. If the clumps are dusty, the escaping photons have less exposure to dust (Neufeld 1991). Therefore, the escape fraction of Ly α in a clumpy medium increases with increasing clump’s H I column density $N_{\text{HI,cl}}$.

If the multiphase medium becomes very clumpy, that is, if the mean number of clumps per line of sight f_c is greater than some critical value, it is advantageous for the Ly α photons to escape as in a homogeneous medium and the spectra (Gronke et al. 2016, 2017), as well as the surface brightness profiles and polarization signal (Chang et al. 2023), converge to the homogeneous one.

Here, we adopt the algorithm to describe the scattering process in a clumpy medium described in Chang et al. (2023) to investigate the emergent spectra and escape fractions of Mg II and Ly α in a clumpy medium. The right panel of Fig. 2 shows the scattering geometry composed of a central source and a clumpy spherical medium, additionally regarding the covering factor f_c . The total H I column density N_{HI} in the clumpy medium is $4/3 f_c N_{\text{HI,cl}}$ where $N_{\text{HI,cl}}$ is clump’s H I column density; in the case of Mg II, $N_{\text{MgII}} = 4/3 f_c N_{\text{MgII,cl}}$. In this section, we investigate Mg II & Ly α radiative transfer and study the emergent spectra, escape fractions, and the doublet ratio R_{MgII} . Also, our simulation considers two types of sources, a monochromatic light and Gaussian emission in § 4.2 and 4.3, respectively.

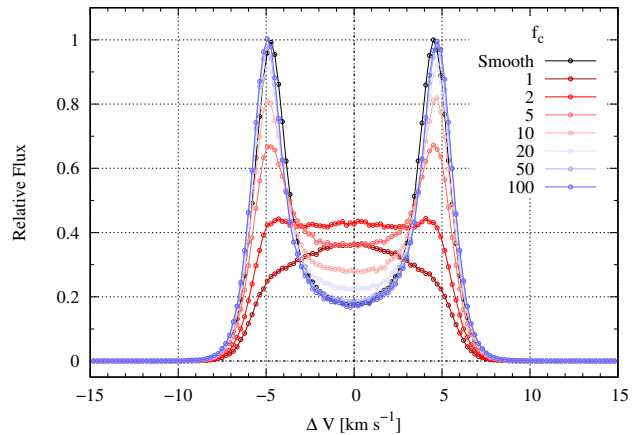


Figure 14. Mg II K line spectra of the clumpy sphere for various covering factors $f_c = 1 - 100$. N_{MgII} is fixed at $10^{13.5} \text{ cm}^{-2}$. The spectra from the clumpy sphere become similar to the spectrum of the smooth sphere with increasing f_c .

4.2 Monochromatic Source

4.2.1 Mg II spectrum

Fig. 14 shows the spectra of the Mg II K line for various covering factors f_c at $N_{\text{MgII}} = 10^{13.5} \text{ cm}^{-2}$ adopting a monochromatic intrinsic emission. This figure clearly shows that Mg II spectrum from a clumpy medium becomes similar to that from a smooth medium as f_c increases like Ly α in a clumpy medium as shown in the previous work (Gronke et al. 2016, 2017; Chang et al. 2023).

The black solid line in Fig. 14 is the spectrum of a smooth medium with the same column density N_{MgII} . While the spectra of a clumpy medium with large f_c resemble that of a homogeneous one, the peak structure is washed out at $f_c \leq 2$. In this low f_c case, all clumps are optically thick for the monochromatic light from the source as $N_{\text{MgII,cl}} \approx N_{\text{MgII}}$. Thus, the clumps are hard to penetrate for the photons, which go through several scatterings merely on the surface of the clumps. This implies that the photons ‘random walk’ between the clumps experience less overall column density (as opposed to a homogeneous medium) and less line broadening.

Fig. 14 also shows that the Mg II spectrum with $f_c \geq 50$ is a clear double-peaked profile, which is identical to that of the smooth medium. We discuss the critical covering factor for this behavior and compare it with that of Ly α in § 4.3.1.

4.2.2 Escape fraction f_{esc}

Fig. 15 shows the escape fraction f_{esc} of the K line and Mg II doublet ratio R_{MgII} as a function of N_{MgII} for various covering factors f_c . The left panel shows that f_{esc} increases with decreasing f_c . Note that since the total column density is kept constant, a smaller f_c means a higher $N_{\text{MgII,cl}}$. The increase of $N_{\text{MgII,cl}}$ leads to a shorter path length l_{path} within the scattering medium of the escaping photon due to the surface scattering effect described in § 4.1.

In a smooth medium, f_{esc} decreases with increasing N_{MgII} because of more scatterings causing a longer l_{path} (as discussed in § 3.1.2). Similarly, for $f_c > 10$, the escape fraction

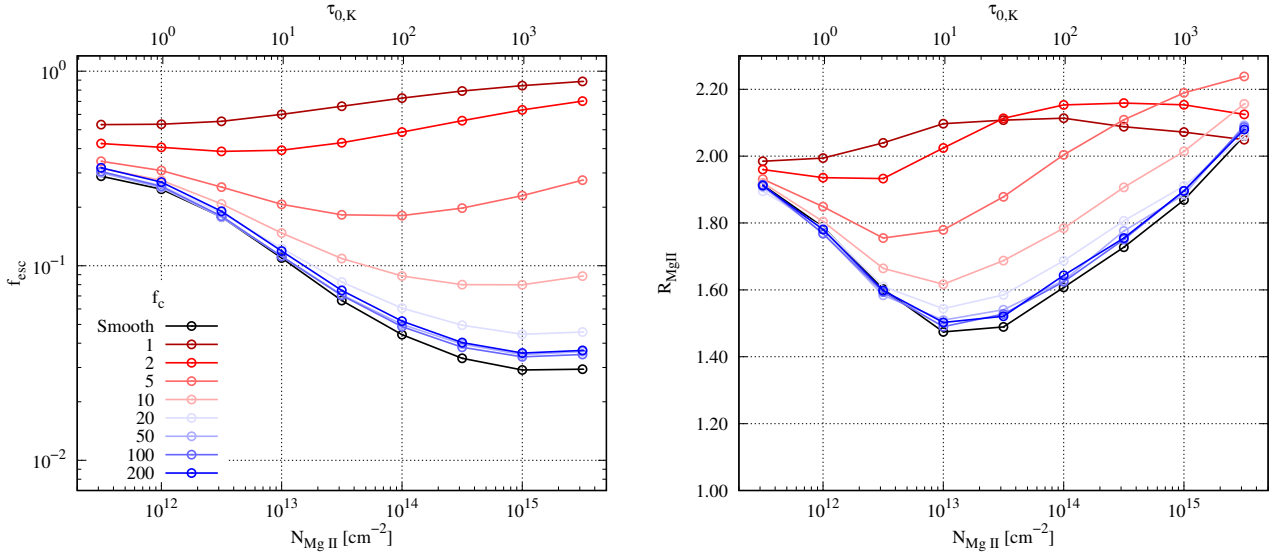


Figure 15. The escaping fraction f_{esc} (left) and doublet ratio R_{MgII} (right) of the monochromatic light case as a function of $N_{\text{MgII}} = 4/3f_c N_{\text{MgII,cl}}$ comparing results of the clumpy medium for various covering factor f_c to the smooth medium. σ_R and $\tau_{\text{d,abs}}$ are fixed at 2.7 km s^{-1} and 1, respectively. The colors of lines represent $f_c = 1$ (red) - 200 (blue) of a clumpy medium and static smooth medium (black). As f_c increases, the profiles of f_{esc} and R_{MgII} in the clumpy medium become similar to those in the smooth medium.

is close to the one of a homogeneous medium. However, for $f_c \leq 2$, the trend is clearly reversed: higher column densities imply a higher escape fraction. This can be explained through the enhanced the surface scattering effect as discussed in § 4.1.

4.2.3 Mg II doublet ratio

In the right panel of Fig. 15, we show the doublet ratio of the monochromatic light case, defined in Eq. 6, emergent from a clumpy medium with total column density N_{MgII} . As before, in the escape fraction, the R_{MgII} for $f_c > 10$ is similar to the smooth medium. This means there is also a characteristic minimum of R_{MgII} at $\tau_0 \sim 12$ in the spherical geometry (cf. § 3.1.2 for a discussion of this effect).

The trends of R_{MgII} versus f_c are more complicated at $f_c < 10$. Generally R_{MgII} increases with decreasing f_c , however for $N_{\text{MgII}} \gtrsim 10^{14} \text{ cm}^{-2}$ this trend is non-monotonous and intermediate $f_c \sim 5$ leads to the highest doublet ratios (even larger than the fiducial value of 2). To understand this effect, it is important to recall that the cross section of the K line is a factor of 2 larger than that of the H line. Hence, the surface scattering effect is stronger for the K line than the H line, leading to $R_{\text{MgII}} > 2$.

4.3 Gaussian Source

This section shows the results of Mg II & Ly α transfer in a clumpy medium with Gaussian emission with intrinsic width $\sigma_{\text{src}} = 100 \text{ km s}^{-1}$. We study the dependence of the Mg II radiative transfer process on the covering factor f_c and compare it to Ly α . We will mainly focus on the spectral profile and the escape fraction f_{esc} .

4.3.1 Spectrum and critical covering factor $f_{c,\text{crit}}$

As discussed in § 4.2 and Fig 14 for large enough f_c resonant line transfer through a multiphase, clumpy medium resembles that through a homogeneous medium. Gronke et al. (2017) investigated this high f_c regime for Ly α radiative transfer and found a critical covering factor $f_{c,\text{crit}}$ above which the photons escape through a homogeneous medium. This prior investigation provides analytic solutions for $f_{c,\text{crit}}$ in various situations: static media, outflowing media, and media composed of randomly moving clumps. In this section, we expand upon this work and find similar critical covering factors for Mg II.

Fig. 16 shows the Mg II & Ly α spectra of a clumpy medium for various f_c and a smooth medium at the same total column densities, $N_{\text{MgII}} = 10^{14.5} \text{ cm}^{-2}$ & $N_{\text{HI}} = 10^{20} \text{ cm}^{-2}$ and $v_{\text{exp}} = 200 \text{ km s}^{-1}$. The spectra at $f_c = 1$ are different from those of a smooth medium (black solid line) and comparable to the intrinsic profile (black dashed line). This is because while, on average, each line-of-sight intercepts one clump, this is not sufficient to fully sample the kinematics of the clumps. On the other hand, for $f_c = 100$, the Mg II and Ly α spectra are identical to those of a smooth medium. We confirm that both spectra of Mg II and Ly α in the clumpy medium become similar to those of the smooth medium at high enough f_c .

To investigate this dependence on f_c of the spectrum further, we measure the similarity of the spectra from the clumpy and smooth media. Fig. 17 shows maps of the similarity $C \cap S$, which is a fraction of the common area overplotting the spectra of the clumpy and smooth media at the same total column density; the range of $C \cap S$ is from 0 to 1. Specifically, we define this similarity parameter as

$$C \cap S = \frac{\int \min(F_{\text{Clumpy}}, F_{\text{Smooth}}) d(\Delta V)}{\int F_{\text{Smooth}} d(\Delta V)} \quad (7)$$

where F_{Clumpy} (F_{Smooth}) is the spectrum as a function of

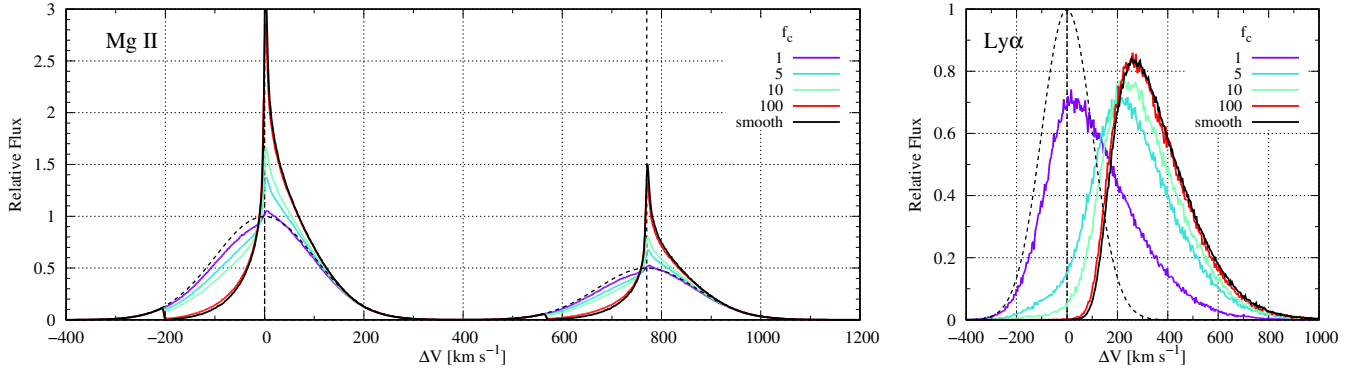


Figure 16. Integrated spectra of Mg II (left) & Ly α (right) for various f_c at $N_{\text{MgII}} = 10^{14.5} \text{ cm}^{-2}$ & $N_{\text{HI}} = 10^{20} \text{ cm}^{-2}$. The width of the intrinsic Gaussian profile σ_{src} and v_{exp} are fixed at 100 km s^{-1} and 200 km s^{-1} , respectively. The color and black lines represent the spectra of the clumpy medium and smooth medium, respectively, at the same total column density $N_{\text{MgII}} = 4/3 f_c N_{\text{MgII,cl}}$. The black dashed line is the intrinsic spectrum. The vertical dashed lines represent the line center of Mg II K & H lines and Ly α .

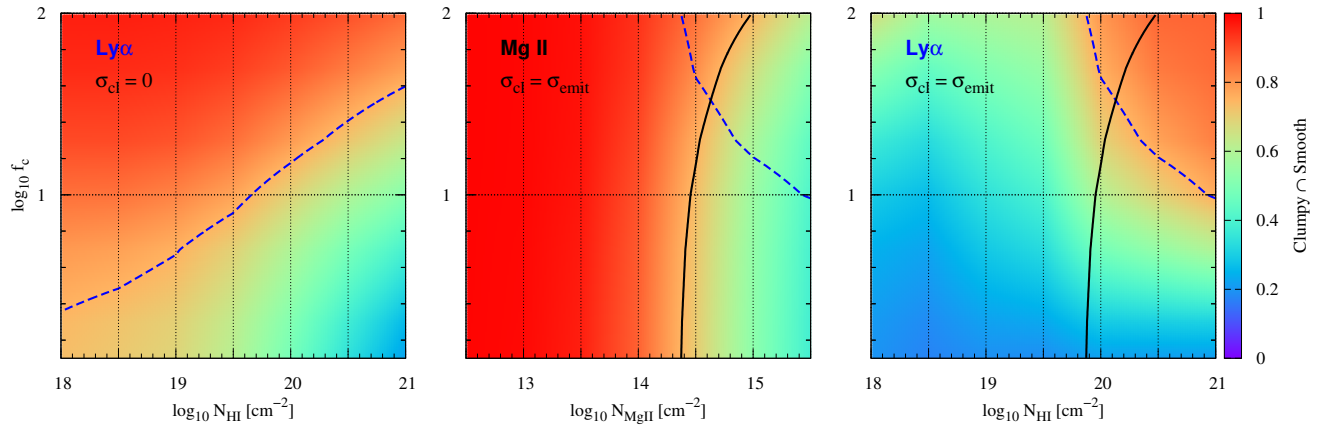


Figure 17. The 2D map of the similarity between Mg II (Ly α) spectra from a clumpy and smooth medium as a function of N_{MgII} (N_{HI}) and covering factor f_c . The similarity is the fraction of the common area of the two types of spectra as defined in Eq. (7). The left panel shows the similarity maps of Ly α in the static medium with the clumps' random velocity $\sigma_{\text{cl}} = 0 \text{ km s}^{-1}$ and $v_{\text{exp}} = 0 \text{ km s}^{-1}$. The center and right panels show the similarity maps of Mg II and Ly α , respectively, with the random motion (σ_{cl} and σ_{R}) being identical to the intrinsic emission width $\sigma_{\text{src}} = 100 \text{ km s}^{-1}$. The black solid and blue dashed contours represent $\text{Clumpy} \cap \text{Smooth} = 0.8$ of Mg II and Ly α , respectively. Here, the dashed lines represent the critical covering factor $f_{c,\text{crit}}$, which is high enough f_c for the spectra from a clumpy medium similar to that from a smooth medium. The map of Mg II in the static medium ($\sigma_{\text{R}} = v_{\text{th}} \sim 2.7 \text{ km s}^{-1}$) is not plotted here and is completely red ($\text{Clumpy} \cap \text{Smooth} \sim 1$) because most initial photons directly escape without scattering due to $\sigma_{\text{src}} \gg v_{\text{th}}$.

the velocity ΔV of the clumpy (smooth) medium, which corresponds to the colored (black) solid line shown in Fig. 16.

At $\text{C}\Omega\text{S} = 1$, the spectrum of the clumpy medium is identical to that of the smooth medium. Each panel shows the map of $\text{C}\Omega\text{S}$ as a function of a column density N_{MgII} (N_{HI}) - f_c . The first–third and second panels of Fig. 17 are maps for Ly α and Mg II, respectively. The black (blue) contour means $\text{C}\Omega\text{S} = 0.8$ for Mg II (Ly α). Hereafter, we define that these contours represent the critical covering factor $f_{c,\text{crit}}$ because 80% similarity is enough for the spectrum of the clumpy medium to be similar to that of the smooth medium.

In the left panel of Fig. 17, we compute the map $\text{C}\Omega\text{S}$ for Ly α in the static clumpy medium with $v_{\text{exp}} = 0 \text{ km s}^{-1}$ and the clump's random motion $\sigma_{\text{cl}} = 0 \text{ km s}^{-1}$. The critical covering factor $f_{c,\text{crit}}$ of Ly α (blue dashed line) increases with

increasing N_{HI} . Gronke et al. (2017) already noted this behavior of $f_{c,\text{crit}}$. Equation 7 in their work suggested the analytic solution for $f_{c,\text{crit}}$ of Ly α in the static medium that $f_{c,\text{crit}}$ is proportional to $\sqrt{N_{\text{HI}}}$.

In the case of Mg II, we do not plot the map because $\text{C}\Omega\text{S}$ of Mg II is always ~ 1 regardless of f_c and N_{MgII} . When $N_{\text{MgII}} = 10^{11.5-15.5} \text{ cm}^{-2}$, only the Gaussian part of the Voigt profile ($\Delta V \lesssim 3v_{\text{th}}$) becomes optically thick (see the left panel of Fig. 1). In both clumpy and smooth media, most intrinsic Mg II photons directly escape without scattering since the width of the intrinsic profile $\sigma_{\text{src}} = 100 \text{ km s}^{-1}$ is much broader than v_{th} of Mg II at 10^4 K ($\sim 2.7 \text{ km s}^{-1}$). Therefore, the spectral profiles from smooth and clumpy media are similar to the profile of incident radiation; hence,

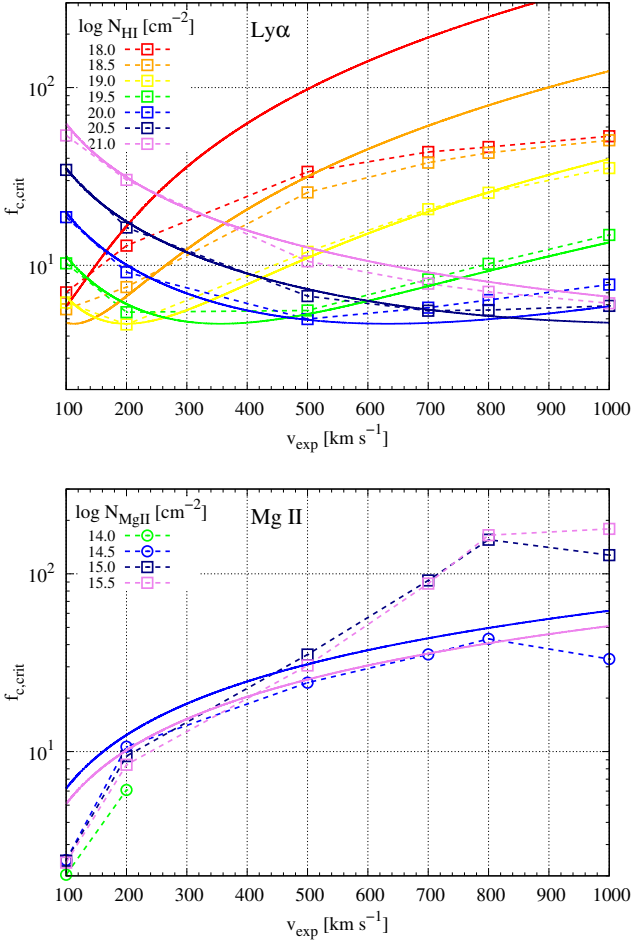


Figure 18. The critical covering factor $f_{c,\text{crit}}$ of Ly α (top) and Mg II (bottom panel) as a function of expansion velocity v_{exp} when the fraction of directly escaping photons is less than 80%. $f_{c,\text{crit}}$ represents the value of f_c when $C \cap S = 0.8$. The dashed lines are $f_{c,\text{crit}}$ from the simulation, and the colors represent the various column densities. The solid lines in the top and bottom panels show Eq. (8) and (10), respectively.

$C \cap S \sim 1$.

In the randomly moving clumpy medium, the critical covering factor $f_{c,\text{crit}}$ of Mg II and Ly α show different behavior. The center and right panels of Fig. 17 exhibit $C \cap S$ of Mg II and Ly α in the clumpy medium with the random motion of clumps $\sigma_{\text{cl}} = 100 \text{ km s}^{-1}$, corresponding to the width of the intrinsic Gaussian profile σ_{src} . The right panel shows that $f_{c,\text{crit}}$ of Ly α (blue dashed line) decreases with increasing N_{HI} . This behavior is similar to the analytic solution in Equation 12 of Gronke et al. (2017) for Ly α RT in the randomly moving clumps $f_{c,\text{crit}} \propto 1/\sqrt{\ln(4/3N_{\text{HI,cl}})}$. However, the center panel of Fig. 17 shows that $f_{c,\text{crit}}$ for Mg II is steeply increasing with increasing $N_{\text{MgII}} (\geq 10^{14.5} \text{ cm}^{-2})$ – i.e., a very different behavior as predicted.

To understand this inverse relation, it is important to recall that for $N_{\text{MgII}} < 10^{14} \text{ cm}^{-2}$, $C \cap S$ is always > 0.8 because most photons ($> 80\%$) directly escape without scattering. Due to the different trends of $f_{c,\text{crit}}$, $f_{c,\text{crit}}$ of Ly α

(blue contour) is smaller than that of Mg II (black contour) in the randomly moving clumpy medium at $N_{\text{MgII}} < 10^{14} \text{ cm}^{-2}$ ($N_{\text{HI}} < 10^{19.5} \text{ cm}^{-2}$). Consequently, the different trends and values of $f_{c,\text{crit}}$ for Ly α & Mg II allow us to constrain the clumpiness of cold gas. We will discuss these prospects further in § 6.6.

In an outflowing clumpy medium, $f_{c,\text{crit}}$ behaves very differently (Gronke et al. 2017). In Equation 13 of their work, when v_{exp} is higher and smaller than the particular velocity \hat{v}_{max} , $f_{c,\text{crit}}$ is proportional to v_{exp}^2 and $1/v_{\text{exp}}$, respectively. Here, \hat{v}_{max} is proportional to $N_{\text{HI}}^{1/3}$ and $\sim 100 \text{ km s}^{-1}$ at $N_{\text{HI}} = 10^{19} \text{ cm}^{-2}$. Fig. 18 shows $f_{c,\text{crit}}$ (dashed lines) defined as the similarity $C \cap S = 0.8$ as a function of v_{exp} for Mg II and Ly α for various column densities.

In the top panel of Fig. 18, we show the Ly α results and confirm that $f_{c,\text{crit}}$ depends on N_{HI} . As v_{exp} increases, $f_{c,\text{crit}}$ increases and decreases at $N_{\text{HI}} \leq 10^{19} \text{ cm}^{-2}$ and $\geq 10^{20} \text{ cm}^{-2}$, respectively. In the bottom panel, $f_{c,\text{crit}}$ of Mg II increases with increasing v_{exp} . This means it follows the trend of Ly α in the low N_{HI} regime ($< 10^{19} \text{ cm}^{-2}$), which is sensible because generally $N_{\text{MgII}} \ll N_{\text{HI}}$.

To compare the trend of $f_{c,\text{crit}}$ from our simulation and in the analytic solutions, we find modified analytic solutions of $f_{c,\text{crit}}$ as a function of v_{exp} , which is necessary since the previous solutions do not capture the full trend observed. The modified analytic solution of $f_{c,\text{crit}}$ is given by

$$f_{c,\text{crit}}(v_{\text{exp}}) = \sqrt{\frac{N_{\text{HI}}}{10^{17} \text{ cm}^{-2}} \frac{x_* v_{\text{th}}}{v_{\text{exp}}}} + \frac{\sqrt{\pi} v_{\text{exp}}^2}{a_v N_{\text{HI}} v_{\text{th}}^2 \sigma_0}, \quad (8)$$

where $x_* \approx 3.26$, $a_v \approx 4.7 \times 10^{-4}$, and $\sigma_0 \approx 5.9 \times 10^{-14} \text{ cm}^2$ (at $T = 10^4 \text{ K}$). The modified solution is composed of the equations for $f_{c,\text{crit}}$ in Gronke et al. (2017). The first term $\propto \sqrt{N_{\text{HI}}}$ is from their equation 9 for the static medium. The second term $\propto 1/v_{\text{exp}}$ and the third term $\propto v_{\text{exp}}^2$ are from their equation 13. In the top panel of Fig. 18, the modified analytic solutions (solid lines) are comparable to the simulated $f_{c,\text{crit}}$ at $N_{\text{HI}} > 10^{19} \text{ cm}^{-2}$. However, $f_{c,\text{crit}}$ at $N_{\text{HI}} < 10^{19} \text{ cm}^{-2}$ and $v_{\text{exp}} > 500 \text{ km s}^{-1}$ shows the difference between simulated values and analytic solutions because of the approximation of the scattering cross section.

The analytic solution of $f_{c,\text{crit}}$ for Ly α cannot be readily adopted to Mg II because Gronke et al. (2017) assumes that the scattering cross section is the approximation of the Lorentzian function due to the high optical depth at the line center ($\tau_0 \gg 1$) to derive the analytic solution. In other words, they consider the Voigt-Hjerting function $H(x, a)$ in Eq. (2) is $\sim a/\sqrt{\pi}x^2$. However, in Mg II RT, when $N_{\text{MgII}} < 10^{16} \text{ cm}^{-2}$, the optical depth in the Lorentzian part of the Mg II cross section is much less than unity ($\tau_v = N_{\text{MgII}} \sigma_v \ll 1$), as shown in the left panel of Fig. 1. Thus, to derive the analytic solution of $f_{c,\text{crit}}$ for Mg II, we should instead approximate the cross section as purely Gaussian.

For a clumpy medium with bulk velocity to behave as a homogeneous medium, the entire velocity range has to be covered by clumps. This means, in our case, that the velocity range from 0 to v_{exp} has to be covered by clumps along each line of sight. For each clump, the velocity width of the optically thick region ($\tau > 1$) ΔV_{clump} is given by

$$\Delta V_{\text{clump}} = 2v_{\text{th}} \sqrt{2 \log(N_{\text{MgII}} \sigma_0)}, \quad (9)$$

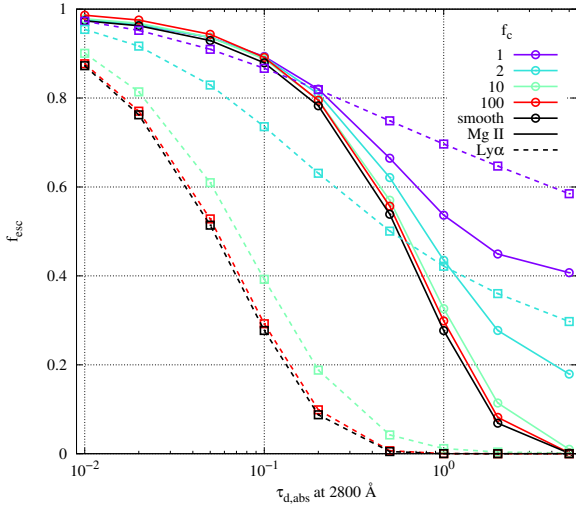


Figure 19. Escape fractions f_{esc} of Ly α (dashed) and Mg II (solid) versus the optical depth of dust absorption at 2800 Å ($\tau_{\text{d,abs}}$) for various covering factor f_c in the static medium ($v_{\text{exp}} = 0 \text{ km s}^{-1}$). The column densities N_{MgII} and N_{HI} is fixed at $10^{15.5} \text{ cm}^{-2}$ and 10^{21} cm^{-2} . The colors represent different f_c . The black solid and dashed lines are the profiles of f_{esc} of Mg II and Ly α at the same N_{MgII} and N_{HI} , respectively, in Fig. 5. The dust optical depth of Ly α is 2.53 times higher than of Mg II. f_{esc} of Ly α is higher than that of Mg II when $\tau_{\text{d,abs}} \geq 1$ and $f_c \leq 10$.

since $H(x, a) \approx e^{-x^2}$ in the approximation of the Gaussian function. In this equation, v_{th} and σ_0 are the thermal speed of Mg II atom at 10^4 K and the scattering cross section at the line center of the Mg II K line, respectively. Since on average f_c clumps can be found per line-of-sight the velocity range covered is $f_c \Delta v_{\text{clump}}$ (i.e., $v_{\text{exp}} = f_{c,\text{crit}} \Delta v_{\text{clump}}$), and hence

$$f_{c,\text{crit}}(v_{\text{exp}}) = \frac{v_{\text{exp}}}{2v_{\text{th}}\sqrt{2\log(N_{\text{MgII}}\sigma_0)}}. \quad (10)$$

In the bottom panel of Fig. 18, we compare the analytic solutions of $f_{c,\text{crit}}$ for Mg II (solid lines) and numerical $f_{c,\text{crit}}$ profiles as a function of v_{exp} (dashed lines). At $N_{\text{MgII}} < 10^{15}$, the analytic solution is comparable to $f_{c,\text{crit}}$ from the simulation. But, when $N_{\text{MgII}} > 10^{15}$ and $v_{\text{exp}} \geq 700 \text{ km s}^{-1}$, the numerical $f_{c,\text{crit}}$ is higher than the analytic value. This gap originates from the physical properties of Mg II doublet. As discussed § 3.2.3, the K line is suppressed by scattering of the H transition in the strong outflow. This induces the mixing of K and H line photons, which is not considered in our simple analytical estimate. Consequently, since our analytic solution is for the K line transition, in the strong outflow/inflow regime ($|v_{\text{exp}}| \geq 700 \text{ km s}^{-1}$), $f_{c,\text{crit}}$ shows the value higher than the analytic solution.

These different trends of $f_{c,\text{crit}}$ for Mg II and Ly α open the possibility of studying the structure of a multiphase gas; we will discuss this further in § 6.6.

4.3.2 Escape fraction f_{esc}

Fig. 19 shows the Mg II and Ly α escape fractions as a function of $\tau_{\text{d,abs}}$ for various f_c at $N_{\text{MgII}} = 10^{15.5} \text{ cm}^{-2}$ and $N_{\text{HI}} = 10^{21} \text{ cm}^{-2}$. We confirm that both escaping fractions of Mg II

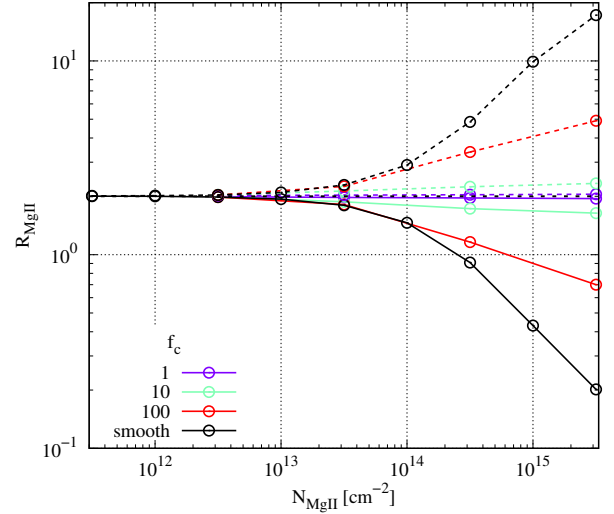


Figure 20. Mg II doublet ratio of the Gaussian emission case in a clumpy medium for various f_c at $v_{\text{exp}} = 1000 \text{ km s}^{-1}$. The solid and dashed lines represent outflow and inflow, respectively. The colors of lines represent various f_c . The solid black line is the result of the smooth medium corresponding to the dark blue line for $v_{\text{exp}} = 1000 \text{ km s}^{-1}$ in Fig. 7. R_{MgII} approaches the intrinsic line ratio 2 with decreasing f_c .

and Ly α increase with decreasing f_c due to the ‘surface scattering’ effect (cf. § 4.1).

Furthermore, we find that the Ly α escape fraction is higher than that of Mg II lines at $f_c < 10$ and $\tau_{\text{d,abs}} > 1$. In the smooth medium, the escape fraction of Ly α is always smaller than that of Mg II because of the dust optical depth of Ly α ~ 2.5 times higher than of Mg II (see Fig. 12 and discussion in § 2.4). In addition, the path length of Ly α is longer than that of Mg II because of the much higher column density.

However, in a clumpy medium, this can be reversed, i.e., the Ly α path length through the scattering medium is shorter, and thus, the escape fraction is higher compared to Mg II. Surface scatterings induce a short path length when a clump is optically thick for incident photons; it causes less interaction with dust in a clump. Thus, the escape fraction increases with decreasing f_c (increasing $N_{\text{HI,cl}}$). This surface scattering effect is much stronger for Ly α than for Mg II photons because $N_{\text{HI}} \gg N_{\text{MgII}}$. We will discuss its details in § 6.1.

4.3.3 Mg II doublet ratio

In the smooth medium, we confirmed that the doublet ratio R_{MgII} varies at $N_{\text{HI}} = 10^{14} \text{ cm}^{-2}$ and $|v_{\text{exp}}| > 700 \text{ km s}^{-1}$ (see § 3.2.3). However, we find that this trend becomes weaker as f_c decreases. Fig. 20 shows the doublet ratio (for the Gaussian emission case defined in Eq. 5) in the clumpy medium for various f_c at $v_{\text{exp}} = 1000 \text{ km s}^{-1}$. The black solid line is the result of the smooth medium in Fig. 7. When f_c decreases, overall R_{MgII} approaches the intrinsic ratio 2. At $f_c = 1$, one finds, on average, only a single clump per line of sight with a distinct expanding velocity. If this expanding velocity is less than 700 km s^{-1} , the line ratio is invariant. In summary, we

note that the variation of R_{MgII} by strong inflow and outflow is sensitive to f_c .

5 Mg II SCATTERING OF STELLAR CONTINUUM

5.1 Mg II emission from flat continuum

Mg II emission features can be generated by stellar continuum radiation near 2800 Å (i.e., continuum pumping). For instance, Xu et al. (2023) measured the equivalent width of Mg II emission to be around 2 – 10 Å, which means the contribution of the stellar continuum is not negligible. When the continuum radiation is scattered by Mg II in an outflowing medium, the escaping spectrum exhibits a P-Cygni profile (Prochaska et al. 2011). Interestingly, as we will show, in this case, the Mg II doublet ratio is not necessarily two. In this section, we investigate the emergent spectrum and the doublet ratio of Mg II, considering a flat continuum as incident radiation.

Fig. 21 displays spectra assuming an intrinsically flat continuum. Each panel shows the dependence on N_{MgII} , v_{exp} , $\tau_{\text{d,abs}}$, and f_c . The spectra are normalized by dividing by the continuum level. A P-Cygni profile appears in most spectra due to the outflow.

Furthermore, to study the trend varying those parameters, in Fig. 22, we measure the equivalent widths of emission $|\text{EW}_{\text{emis}}|$ and absorption $|\text{EW}_{\text{abs}}|$ of the spectra from the flat continuum in the range of the wavelength from $\lambda_{\text{K}} - \Delta\lambda_{300}$ to $\lambda_{\text{H}} + \Delta\lambda_{300}$ (corresponding the velocity range from -300 km s^{-1} of the K line to $+300 \text{ km s}^{-1}$ of the H line). Thus, the equivalent widths are given by

$$|\text{EW}_{\text{emis}}| = \frac{\int_{\lambda_{\text{K}} - \Delta\lambda_{300}}^{\lambda_{\text{H}} + \Delta\lambda_{300}} (F(\lambda) - F_c) d\lambda}{F_c}, \quad \text{when } F(\lambda) > F_c$$

$$|\text{EW}_{\text{abs}}| = -\frac{\int_{\lambda_{\text{K}} - \Delta\lambda_{300}}^{\lambda_{\text{H}} + \Delta\lambda_{300}} (F(\lambda) - F_c) d\lambda}{F_c}, \quad \text{when } F(\lambda) < F_c \quad (11)$$

where the continuum flux F_c is the flux level near 2880 Å (-1500 km s^{-1} from the K line).

To investigate the doublet ratio of the spectrum with a continuum, we measure the ratio of $|\text{EW}_{\text{emis}}|$ of K and H lines in the right panel of Fig. 22. The ratio of $|\text{EW}_{\text{emis}}|$ represents the doublet ratio of Mg II emission features in the emergent spectrum with a continuum resembling the doublet ratio of the intrinsic emission case in Eq (5). To compute the $|\text{EW}_{\text{emis}}|$ ratio, we calculate the $|\text{EW}_{\text{emis}}|$ of both the K and H lines within a velocity range of $\pm 300 \text{ km s}^{-1}$ from their respective centers. Consequently, the $|\text{EW}_{\text{emis}}|$ of the K line is determined by the equation

$$|\text{EW}_{\text{emis,K}}| = \frac{\int_{\lambda_{\text{K}} - \Delta\lambda_{300}}^{\lambda_{\text{K}} + \Delta\lambda_{300}} (F(\lambda) - F_c) d\lambda}{F_c}, \quad \text{when } F(\lambda) > F_c. \quad (12)$$

Similarly, $|\text{EW}_{\text{emis,H}}|$ follows the same equation within the identical velocity range $\pm 300 \text{ km s}^{-1}$ from the line center of the H line. Hence, we define the Mg II doublet ratio of the spectrum with a continuum,

$$R_{\text{MgII}}^{\text{C}} = \frac{|\text{EW}_{\text{emis,K}}|}{|\text{EW}_{\text{emis,H}}|}. \quad (13)$$

In this section, we specify that the doublet ratio R_{MgII} is $R_{\text{MgII}}^{\text{C}}$ since the Mg II spectrum has a continuum.

5.1.1 Dependence on N_{MgII}

The left top panel of Fig. 21 shows Mg II spectra for three $N_{\text{MgII}} = 10^{12.5}$, $10^{13.5}$, and $10^{14.5} \text{ cm}^{-2}$ at $v_{\text{exp}} = 200 \text{ km s}^{-1}$. The red emission and blue absorption features become stronger with increasing N_{MgII} . In the left and center panels of Fig. 22, $|\text{EW}_{\text{emis}}|$ and $|\text{EW}_{\text{abs}}|$ increase with increasing N_{MgII} . In the dust free cases (solid lines), the profile of $|\text{EW}_{\text{emis}}|$ is akin to that of $|\text{EW}_{\text{abs}}|$ because the photons from the blueward become the emission features in the redward via scattering in an outflowing medium.

In the left top panel of Fig. 21, at $N_{\text{MgII}} = 10^{13.5} \text{ cm}^{-2}$, the absorption feature in the blueward of the K line is two times stronger than that of the H line. At $N_{\text{MgII}} = 10^{14.5} \text{ cm}^{-2}$, the two blue absorption features are similar since this high N_{MgII} regime is enough to cause nearly all continuum photons in the blueward of K and H lines to undergo scattering. This effect is shown more quantitatively in the right panel of Fig. 22 showing R_{MgII} as a function of N_{MgII} . The trend from the intrinsic $R_{\text{MgII}} \sim 2$ to $R_{\text{MgII}} \sim 1$ at $N_{\text{MgII}} \gtrsim 10^{15} \text{ cm}^{-2}$ is apparent (but to various strengths) for a variety of dust optical depths and outflow velocities.

In the right panel of Fig. 22, R_{MgII} decreases with decreasing N_{MgII} in the low N_{MgII} regime ($N_{\text{MgII}} < 10^{13} \text{ cm}^{-2}$) because of the noisy spectrum. Measuring the doublet ratio of the noisy spectrum at $N_{\text{MgII}} = 10^{12.5} \text{ cm}^{-2}$ in the left top panel of Fig. 21, some noise can be counted as emission features and contribute equally increasing $|\text{EW}_{\text{emis}}|$ of K and H lines. Hence, the doublet ratio from the noise fluxes is ~ 1 . The doublet ratio is underestimated in this low N_{MgII} regime. However, since the emission is hard to be observable, we focus on the trend of R_{MgII} at $N_{\text{MgII}} > 10^{13} \text{ cm}^{-2}$.

In short, if the absorption is saturated, the emission doublet ratio will be – per construction – ~ 1 , whereas for lower optical depths, the different values of the cross section play a role and lead to ratios closer to the fiducial ratio of ~ 2 . We will discuss this effect further and argue that it might explain observations of Chisholm et al. (2020) in § 5.2.

5.1.2 Dependence on $\tau_{\text{d,abs}}$

The left bottom panel of Fig. 21 shows the spectra normalized by the continuum level for four values of dust extinction $\tau_{\text{d,abs}} = 0, 0.1, 0.5,$ and 1 . Even though the absorption features do not strongly depend on $\tau_{\text{d,abs}}$, the emission features weaken with increasing $\tau_{\text{d,abs}}$. This is due to the same effect found for the Gaussian emission case discussed in Fig. 11.

How this variation in dust content affects R_{MgII} is shown with dashed lines for $\tau_{\text{d,abs}} = 1$ in the right panel of Fig. 22. As discussed, the absorption feature is unaffected by dust, and the profile of $|\text{EW}_{\text{abs}}|$ at $\tau_{\text{d,abs}} = 1$ is identical to that of a dust-free medium. However, when the continuum photon undergoes scattering to become the red emission features seen, the path length of the scattered photon is longer than the direct escaping photons. Thus, $|\text{EW}_{\text{emis}}|$ decreases with increasing $\tau_{\text{d,abs}}$. In other words, dust extinction decreases the strength of the Mg II emission features from the continuum pumping.

Because the increase in path length causing the decrease in the escape probability depends on the different cross sections of the two lines, the line ratio is slightly decreased with increasing dust content, as shown by the dashed line in the right

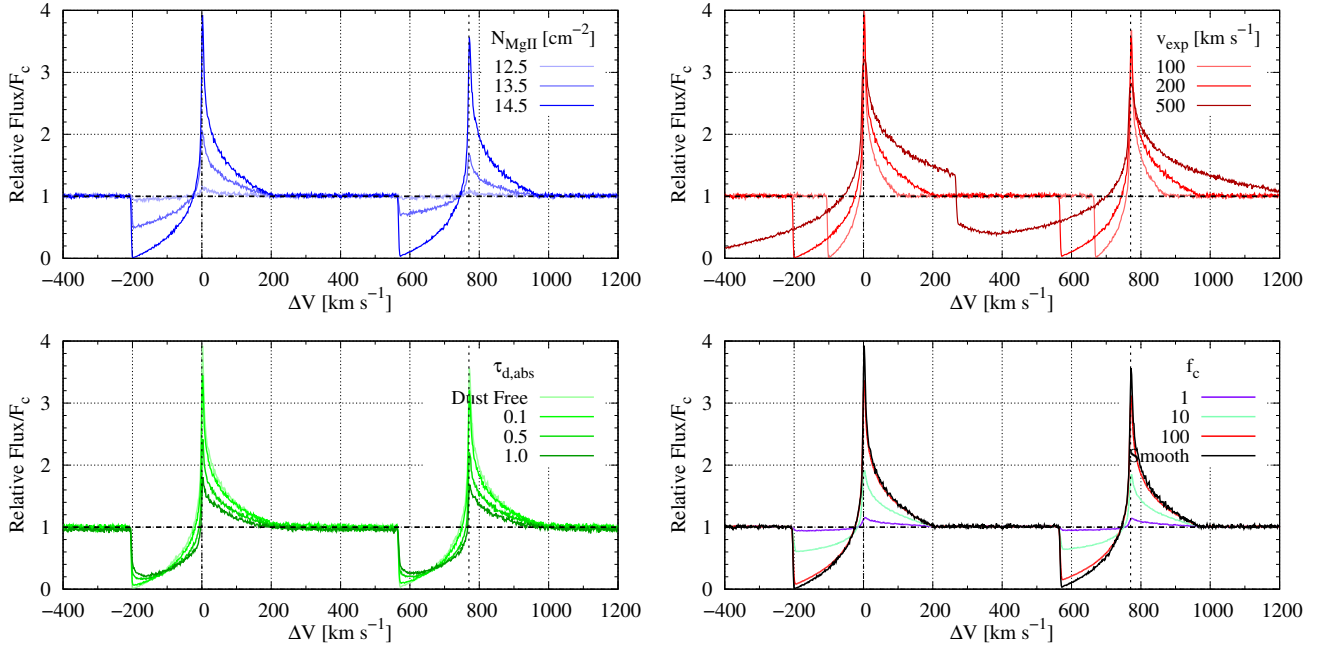


Figure 21. Mg II spectra assuming an flat continuum for various N_{MgII} (left top), v_{exp} (right top), $\tau_{\text{d,abs}}$ (left bottom), and f_c (right bottom). The left top panel shows the blue spectra for $N_{\text{MgII}} = 10^{12.5-14.5}$ when v_{exp} is fixed at 200 km s^{-1} . The red spectra in the right top panel are for three $v_{\text{exp}} = 100, 200,$ and 500 km s^{-1} at $N_{\text{MgII}} = 10^{14.5} \text{ cm}^{-2}$. In the bottom panels, N_{HI} and v_{exp} are fixed at $10^{14.5} \text{ cm}^{-2}$ and 200 km s^{-1} . Most spectra are from the dust free medium ($\tau_{\text{d,abs}} = 0$) except the spectra with $\tau_{\text{d,abs}} > 0$ in the left bottom panel. In the right bottom panel, the black line is the spectrum of the smooth medium, which is identical to the spectra at $N_{\text{MgII}} = 10^{14.5} \text{ cm}^{-2}$ in the left top panel. The blue, green, and red colors represent $f_c = 1, 10,$ and 100 at the same N_{MgII} . The spectra are shown in units of normalized flux, i.e., the relative flux divided by the continuum level F_c .

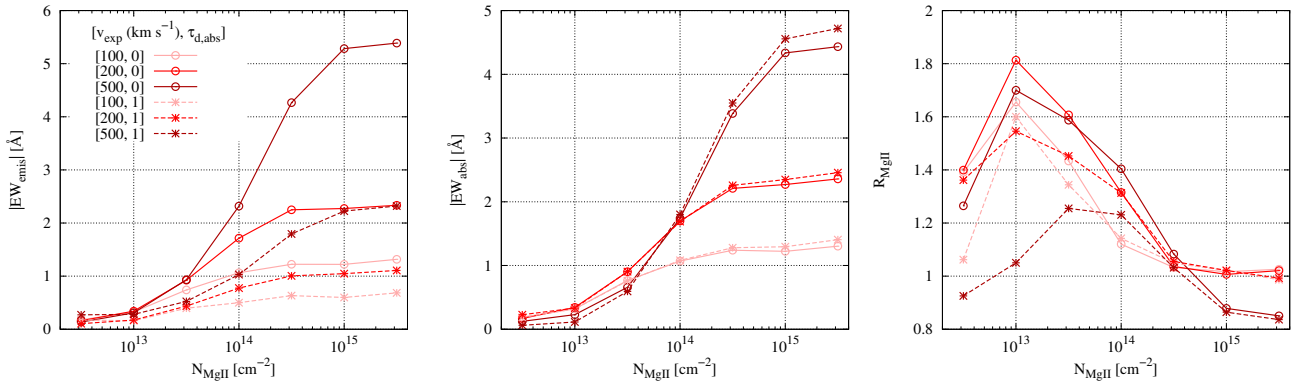


Figure 22. Equivalent width of Mg II emission (left) and absorption (center) features as a function of N_{MgII} . The right panel shows the Mg II doublet ratio of the spectrum with the continuum defined in Eq. (13), which is the ratio of the equivalent widths of Mg II K and H emission lines. The line colors represent various v_{exp} . The solid and dashed lines are for the dust-free and dusty medium at $\tau_{\text{d,abs}} = 1$, respectively.

panel of Fig. 22. This effect is negligible at $N_{\text{MgII}} \geq 10^{15} \text{ cm}^{-2}$ since the ratio of the path lengths of the lines is ~ 1 (see Fig. 8). Thus, R_{MgII} does not strongly depend on the dust optical depth.

5.1.3 Dependence on v_{exp}

The right top panel of Fig. 21 shows the Mg II spectra for three $v_{\text{exp}} = 100, 200,$ and 500 km s^{-1} at $N_{\text{MgII}} = 10^{14.5} \text{ cm}^{-2}$. When v_{exp} increases, the widths of the emission and

absorption become broader. A higher v_{exp} causes scattering in a wider range of incident continuum radiation. Accordingly, $|EW_{\text{emis}}|$ as well as $|EW_{\text{abs}}|$ increase with increasing v_{exp} , which can be seen in the left and center panels of Fig. 22, respectively. Since both K and H lines show the same behavior, R_{MgII} does not strongly depend on v_{exp} (also because here we focus on the $v_{\text{exp}} < 700 \text{ km s}^{-1}$ case) as shown in the right panel of Fig. 22.

5.1.4 Dependence on f_c

Lastly, the right bottom panel of Fig. 21 displays Mg II spectra for various degrees of clumpiness, characterized by f_c at $N_{\text{MgII}} = 10^{14.5} \text{ cm}^{-2}$. The trend of spectra varying f_c is similar to that found in the previous section for the Gaussian source.

As seen before, the spectrum of the clumpy medium shown in Fig. 21 becomes similar to that of the smooth medium with increasing f_c . At $f_c = 1$, the scattering is negligible, and the escaping spectrum is flat like the incident radiation. At $f_c = 10$, even though the absorption feature is weaker than that of the smooth medium, the doublet ratio of emission features is still ~ 1 . The amount of photons undergoing scattering decreases with decreasing f_c .

The Mg II doublet ratio varies through scattering by the fast-moving medium ($v_{\text{exp}} > 700 \text{ km s}^{-1}$) as shown in Fig. 7. In this case, R_{MgII} converges to the intrinsic ratio 2 with decreasing f_c (see Fig. 20) because the number of photons moving from the K/H line to the H/K line by the strong outflow/inflow decreases. However, since R_{MgII} in the clumpy medium is mainly determined by the ratio of scattered K and H photons which hinge on N_{MgII} , R_{MgII} is not sensitive for f_c and still depends on the total column density N_{MgII} .

5.2 Stellar continuum with in situ Mg II emission

Mg II emission is observed alongside continuum radiation with measured equivalent widths (EW) $\sim 2 - 10 \text{ \AA}$ (Henry et al. 2018; Xu et al. 2023). It is commonly also more spatially extended than UV continuum (Leclercq et al. 2022; Dutta et al. 2023; Guo et al. 2023b). Chisholm et al. (2020) reported that the Mg II doublet ratio in the central region, including the source galaxy, is higher than in the region surrounding the galaxy. They found the doublet ratio of inside and outside are ~ 2 and 1.3, respectively.

In the previous sections, we identified two mechanisms to change the Mg II doublet ratio, (1) scattering in strong outflow/inflow and (2) scattering of the flat continuum. In § 3.2.3, we showed that the doublet ratio varies when the expansion speed v_{exp} is higher than the velocity separation of K and H lines, $\sim 750 \text{ km s}^{-1}$. Furthermore, in § 5.1, we noted that considering the flat continuum as the incident radiation, the doublet ratio decreases with increasing N_{MgII} ; $R_{\text{MgII}} \sim 1$ at $N_{\text{MgII}} > 10^{14} \text{ cm}^{-2}$.

In this section, we combine the two emission mechanisms introduced in the previous sections and consider the incident radiation, including a flat continuum and in situ Gaussian emission, to investigate the Mg II spectra and the behavior of the Mg II doublet ratio under more realistic conditions. Hence, hereafter, we define that the doublet ratio R_{MgII} is $R_{\text{MgII}}^{\text{E}}$ in Eq. (5) ($R_{\text{MgII}}^{\text{C}}$ in Eq. (13)) if the spectrum is without (with) a continuum. Furthermore, we separate in this section the Mg II spectra originating from the central and halo regions as opposed to simply focusing on the integrated spectrum as we have in the previous sections.

5.2.1 Central versus Halo Mg II emission

Fig. 23 shows the simulated Mg II spectra of the source consisting of a flat continuum and an in situ Gaussian emission with the width $\sigma_{\text{src}} = 100 \text{ km s}^{-1}$ and the intrinsic

equivalent width $\text{EW}_{\text{int}} = 5 \text{ \AA}$. N_{MgII} and v_{exp} are fixed at 10^{15} cm^{-2} and 200 km s^{-1} , respectively. The spectrum shown is smoothed with a Gaussian profile with a width of 30 km s^{-1} , corresponding to the spectral resolution of $R \sim 10^4$ in order to be more easily compared to observations.

The left panel of Fig. 23 shows the total integrated spectrum. The center and right spectra are ‘central’ and ‘halo’ spectra composed of escaping photons at the projected radius $r_p < 0.1R_{\text{H}}$ and $> 0.1R_{\text{H}}$, respectively. The red and blue dashed lines represent the spectrum of the continuum and emission to visualize the contribution of the two types of sources independently.

The right panel of Fig. 23 shows that the halo spectrum is an emission feature without continuum radiation because the halo spectrum is composed of only scattered photons. For most photons, the medium is optically thin, and they directly escape as the ‘central spectrum’. This is not the case for the photons in the range from the systemic velocity to $\Delta V = -v_{\text{exp}}$, which are scattered and make up the ‘halo spectrum’. Hence, in the center panel of Fig. 23, the central spectrum has stronger absorption and weaker emission features than the total spectrum in the left panel due to the absence of scattered photons. In addition, the central spectrum from the continuum does have significant emission features and looks like the incident radiation with the absorption feature by scattering medium in the line of sight.

The contribution of the stellar continuum and in situ emission determines the Mg II doublet ratio R_{MgII} . Fig. 23 shows that the doublet ratio R_{MgII} is always ~ 1 and 2 from continuum and Gaussian emission, respectively – both in the central and halo spectra. However, the observable doublet ratio R_{MgII} differs between the central and the halo region. The central panel of Fig. 23 shows the central spectrum with $R_{\text{MgII}} \sim 2$. The emission feature from the continuum (red dashed line) is much weaker than that from the in situ emission (blue dashed line) because most initial photons in the blueward are spatially diffused via scattering and classified as the halo spectrum. Thus, $R_{\text{MgII}} \sim 2$ as the in situ emission dominates the emission features of the center spectrum. In the right panel of Fig. 23, the strengths of the K line emissions from the continuum ($R_{\text{MgII}} \sim 2$) and in situ emission ($R_{\text{MgII}} \sim 1$) are comparable in the halo spectrum. Hence, R_{MgII} is ~ 1.3 and smaller than in the central spectrum. The left panel of Fig. 23 shows that R_{MgII} of the total spectrum is ~ 1.6 . Both directly escaping photons of the in situ emission with $R_{\text{MgII}} \sim 2$ (central spectrum) and scattering photons with $R_{\text{MgII}} \sim 1.3$ (halo spectrum) contribute to the formation of the Mg II emission features above the continuum.

In summary, the combination of continuum and Gaussian in situ Mg II emission can lead to doublet ratios $R_{\text{MgII}} < 2$ also with moderate ($< 700 \text{ km s}^{-1}$) velocities if $N_{\text{MgII}} > 10^{14} \text{ cm}^{-2}$. This is because the absorption of the continuum part is saturated, resulting in $R_{\text{MgII}} \sim 1$ of the scattered emission, whereas, for the Gaussian component, the ratio remains close to its fiducial value $R_{\text{MgII}} \sim 2$. The (weighted) averaging of these two mechanisms leads thus to $R_{\text{MgII}} < 2$ with a lower value – due to the larger contribution from the continuum – found in the halo spectrum. This is a plausible mechanism to explain the low doublet ratios observed, and we will investigate this more systematically below.

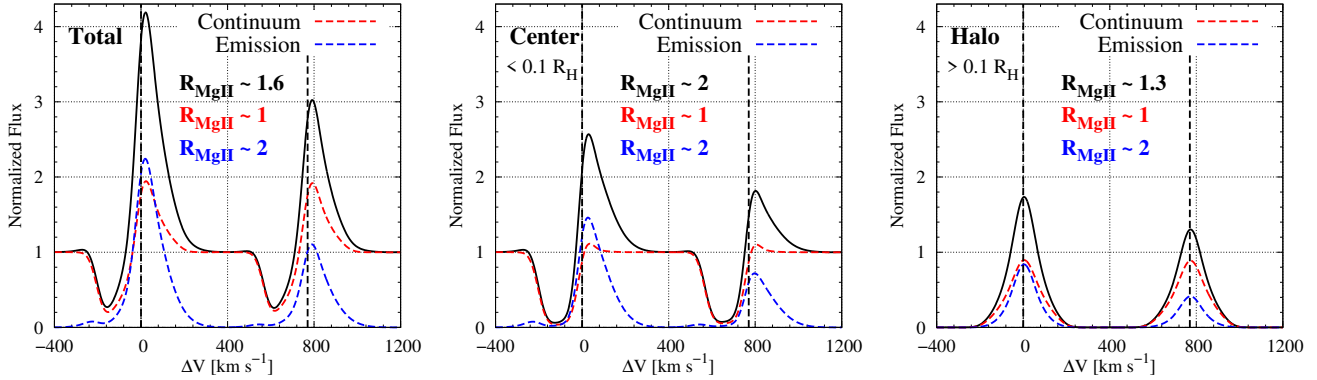


Figure 23. The total integrated spectrum (left), central spectrum escaping at projected radii $R_p < 0.1 R_H$ (center), and halo spectrum ($R_p > 0.1 R_H$; right panel). The incident radiation consists of a flat continuum and Gaussian emission with $\sigma_{\text{emit}} = 100 \text{ km s}^{-1}$ and equivalent width $\text{EW} = 5 \text{ \AA}$. v_{exp} , N_{MgII} , and f_c are fixed at 200 km s^{-1} , 10^{15} cm^{-2} , and 100, respectively. Spectra are shown as normalized flux with the flat continuum being unity. The black solid line represents the total escaping spectrum of the incident radiation, whereas the red and blue dashed lines show the escaping spectrum of only the flat continuum and the Gaussian emission, respectively. The values of R_{MgII} indicated in each panel mark the doublet ratio of each emission part in the corresponding color. R_{MgII} of the total and center spectra with the continuum is the ratio of Mg II K and H emission features over the continuum, which is identical to the emission EW ratio of Mg II in Eq. (13). R_{MgII} of the spectra without the continuum is the double ratio of the emission case in Eq. (5).

5.2.2 Mg II doublet ratio & N_{MgII}

In order to study the dependence of R_{MgII} on N_{MgII} with the joined intrinsic spectrum, Fig. 24 shows R_{MgII} as a function of N_{MgII} in the slow outflow and inflow ($0 \text{ km s}^{-1} < |v_{\text{exp}}| < 500 \text{ km s}^{-1}$) regime. The star marks and open circles represent the smooth medium and the clumpy medium with $f_c = 20, 50$, and 100. In the top panel for the total integrated spectrum, at $N_{\text{MgII}} < 10^{14} \text{ cm}^{-2}$, the doublet ratio of the total spectrum $R_{\text{MgII,Total}}$ is ~ 2 regardless of other parameters. In this low N_{MgII} regime, the in situ emission mainly contributes to the formation of $R_{\text{MgII,Total}}$. In other words, the in situ emission dominates the emission features of the escaping spectrum, and the effect of scattering is relatively negligible in the total spectrum.

At high column densities ($N_{\text{MgII}} > 10^{14} \text{ cm}^{-2}$), the doublet ratio becomes $R_{\text{MgII,Total}} < 2$ since the scattering of the flat continuum is sufficient to make the emission features with $R_{\text{MgII,Total}} \sim 1$ as discussed in the previous section and shown in the right panel of Fig. 22.

In the bottom panel of Fig. 24, the profile of the halo doublet ratio $R_{\text{MgII,Halo}}$ shows a clear trend comparing that of $R_{\text{MgII,Total}}$; $R_{\text{MgII,Halo}}$ declines with increasing N_{MgII} . In the low N_{MgII} regime, $R_{\text{MgII,Halo}}$ is > 2 because the halo spectrum is composed of scattered photons. The ratio of scattering rate of the K and H lines at $N_{\text{MgII}} < 10^{14} \text{ cm}^{-2}$ is higher than unity as shown in the right panel of Fig. 22 since the optical depth of the K line $\tau_K \sim 2\tau_H$. Therefore, when the in situ emission with the intrinsic doublet ratio 2 undergoes scattering, the doublet ratio of scattered photons is > 2 . We will discuss this further below.

For large N_{MgII} , however, the contribution of scattered photons of the flat continuum leads to $R_{\text{MgII}} < 2$ – as seen in the example shown in Fig. 22 above. As a result, the Mg II doublet ratios of both the total and halo spectra become less than 2 at $N_{\text{MgII}} > 10^{14} \text{ cm}^{-2}$ as shown by Fig. 24.

Fig. 25 shows the halo doublet ratio for various intrinsic equivalent widths of the in situ emission EW_{int} at $v_{\text{exp}} = 100 \text{ km s}^{-1}$. The overall $R_{\text{MgII,Halo}}$ increases with

increasing EW_{int} and does not strongly depend on f_c . In the high N_{MgII} regime, $R_{\text{MgII,Halo}}$ is ~ 1 for $\text{EW}_{\text{int}} = 0$ and 2 for $\text{EW}_{\text{int}} = 100 \text{ \AA}$, i.e., fully determined by whether the spectrum is dominated by the in situ emission or the flat continuum.

From the above findings, one can construct a simple analytical model to predict the doublet ratio given an intrinsic equivalent width and Mg II column density. As the halo is composed of scattered photons, the ratio of scattered K and H photons determines $R_{\text{MgII,Halo}}$. In the optically thin regime ($\tau_0 < 1$), the ratio of scattered K and H line photons is ~ 2 since the scattering fraction is $1 - \exp(-\tau_0) \approx \tau_0$ and $\tau_{0,K} = 2\tau_{0,H}$. Here, τ_K and τ_H are the optical depth near the K and H transition, respectively⁴. In the optically thick regime ($\tau_0 > 1$), however, the continuum absorption is saturated, and most K and H photons undergo scattering. The scattering fraction in the medium with optical depth τ is given by

$$f_{\text{scat}} = 1 - e^{-\tau}. \quad (14)$$

Therefore, the ratio of the K and H lines' scattering fractions given by

$$\frac{f_{\text{scat,K}}}{f_{\text{scat,H}}} = \frac{1 - e^{-\tau_K}}{1 - e^{-\tau_H}} = 1 + e^{-\tau_H} \quad (15)$$

where in the last step we used $\tau_K \approx 2\tau_H$.

To estimate $R_{\text{MgII,Halo}}$ analytically using the scattering fractions above, one requires the doublet ratio near the K and H lines of the intrinsic radiation. The scattering geometry for our simulation has a Hubble-like outflow where the outflow velocity is proportional to the distance from the central source. This – and the fact that Mg II scattering in the Lorentzian part is negligible – implies that photons in the

⁴ Note that throughout this work, we refer to τ as the optical depth of the K line unless specified otherwise.

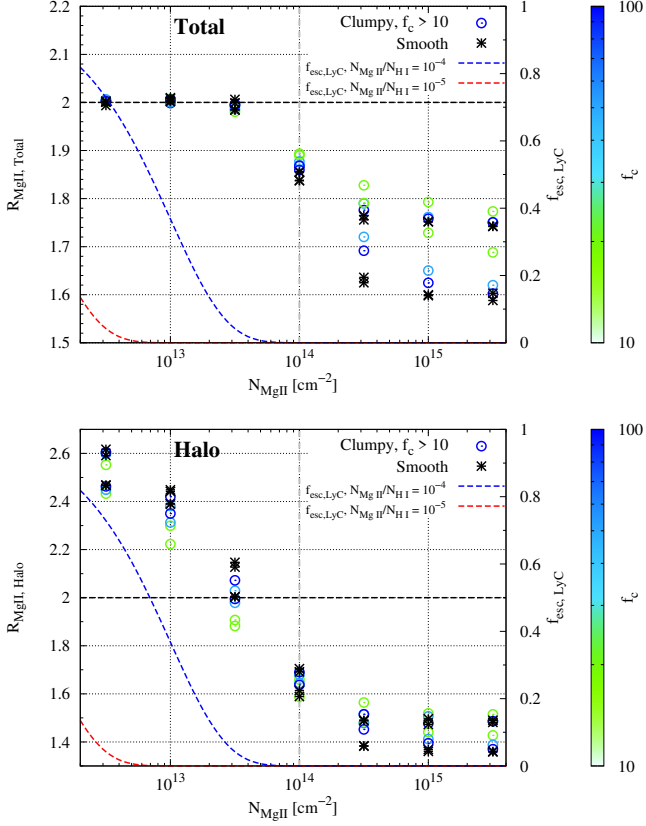


Figure 24. R_{MgII} as a function of N_{MgII} ($=f_c N_{\text{MgII,cl}}$ for clumpy medium) considering the flat continuum and in situ emission with the intrinsic equivalent width $\text{EW}_{\text{int}} = 5 \text{ \AA}$ as the incident radiation like the spectrum in Fig. 23. The star marks and open circles represent the smooth and clumpy media for $f_c > 10$. The colors of the circles indicate the values of covering factor f_c , according to the color bar on the right side. The top and bottom panels are for the doublet ratio of the total integrated spectrum $R_{\text{MgII,Total}}$ and halo spectrum $R_{\text{MgII,Halo}}$, respectively. In the top panel, because of the existence of the continuum in the total spectrum (see the left panel of Fig. 23), $R_{\text{MgII,Total}}$ is the doublet ratio of Mg II emission feature, which is the ratio of $|\text{EW}_{\text{emis}}|$ the K and H photons over the continuum in Eq. (13). In the bottom panel, Eq. (5) for the doublet ratio of the emission case is adopted to calculate $R_{\text{MgII,Halo}}$ because of the halo spectrum without the continuum (see the right panel of Fig. 23). The blue and red dashed lines are the profile of the LyC escape fraction $f_{\text{esc,LyC}}$ as a function of N_{MgII} assuming the Mg II fraction $f_{\text{MgII/HI}} = N_{\text{MgII}}/N_{\text{HI}} \sim 10^{-4}$ and 10^{-5} , respectively. Generally, $R_{\text{MgII,Total}}$ and $R_{\text{MgII,Halo}}$ decrease with increasing N_{MgII} .

velocity range from $-v_{\text{exp}}$ to 0 km s^{-1} undergo scattering. In this velocity range, the intrinsic doublet ratio is given by

$$R_{\text{MgII,int}} = \frac{\int_{\lambda_K - \Delta\lambda_K}^{\lambda_K} F_i(\lambda) d\lambda}{\int_{\lambda_H - \Delta\lambda_H}^{\lambda_H} F_i(\lambda) d\lambda}, \quad (16)$$

where $F_i(\lambda)$ is the intrinsic radiation and $\Delta\lambda_{\text{K,H}} = v_{\text{exp}} \lambda_{\text{K,H}}/c$. This implies that for our fiducial choice of $v_{\text{exp}} = 100 \text{ km s}^{-1}$, $R_{\text{MgII,int}}$ is 1, 1.38, 1.55, and 2 for $\text{EW}_{\text{int}} = 0 \text{ \AA}$ (a flat continuum), 5 \AA , 10 \AA , and ∞ (Mg II emission without a continuum), respectively.

The intrinsic radiation with EW_{int} normalized by the con-

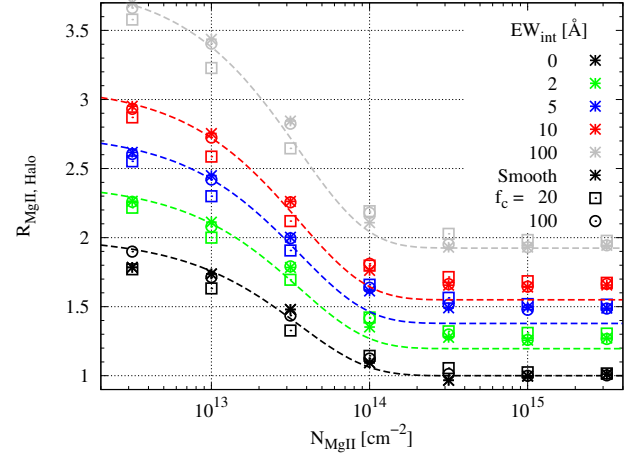


Figure 25. $R_{\text{MgII,Halo}}$ for various intrinsic equivalent width EW_{int} as a function of N_{MgII} at $v_{\text{exp}} = 100 \text{ km s}^{-1}$. The colors represent $\text{EW}_{\text{int}} = 0$ (black), 2 (green), 5 (blue), 10 (red), and 100 (gray). The dashed lines show the relation between $R_{\text{MgII,Halo}}$ and N_{MgII} noted in Eq. (19). The shapes of points present the smooth medium (star) and the clumpy media with $f_c = 20$ (square) and 100 (circle). The blue points correspond to $R_{\text{MgII,Halo}}$ at $v_{\text{exp}} = 100 \text{ km s}^{-1}$ in the bottom panel of Fig. 24. v_{exp} is fixed at 100 km s^{-1} .

tinuum flux F_c is given by

$$F_i(\lambda)/F_c = 1 + \frac{\text{EW}_{\text{int}}}{3} [2G(\lambda, \lambda_K, \sigma_{\text{src}}) + G(\lambda, \lambda_H, \sigma_{\text{src}})], \quad (17)$$

where $G(x, \mu, \sigma) = \exp(-(x - \mu)^2/2\sigma^2)/\sqrt{2\pi\sigma^2}$ is a Gaussian profile with mean μ and variance σ^2 .

Therefore, adopting Eq. (16) and (17), we can write the intrinsic doublet ratio

$$R_{\text{MgII,int}} = \frac{6\Delta\lambda_K + 2\text{EW}_{\text{int}}\text{erf}(v_{\text{exp}}/\sqrt{2}\sigma_{\text{src}})}{6\Delta\lambda_H + \text{EW}_{\text{int}}\text{erf}(v_{\text{exp}}/\sqrt{2}\sigma_{\text{src}})}. \quad (18)$$

Thus, R_{MgII} in the halo is given by

$$R_{\text{MgII,Halo}} = R_{\text{MgII,int}} \frac{f_{\text{scat,K}}}{f_{\text{scat,H}}} = R_{\text{MgII,int}} (1 + e^{-\overline{\tau}_H}). \quad (19)$$

Here, $\overline{\tau}_H$ is the average optical depth of the K line from $-v_{\text{exp}}$ to 0 km s^{-1} . Using σ_v in Eq. (1) and assuming the homogeneous medium with uniform number density and a Hubble-like outflow, $\overline{\tau}_H$ is given by

$$\overline{\tau}_H = \left(\frac{N_{\text{MgII}}}{3.6 \times 10^{13} \text{ cm}^{-2}} \right) \left(\frac{v_{\text{exp}}}{100 \text{ km s}^{-1}} \right)^{-1}. \quad (20)$$

Fig. 25 shows that the halo doublet ratio $R_{\text{MgII,Halo}}$ can be well described by Eq. (19). Only for $N_{\text{MgII}} \geq 10^{14} \text{ cm}^{-2}$ small differences can be found due to multiple scatterings.

Note that the dashed lines in Fig. 24 represent LyC escape fraction $f_{\text{esc,LyC}}$ as a function of N_{MgII} assuming Mg II fractions = 10^{-4} and 10^{-5} . Specifically, the figure shows that $R_{\text{MgII,Total}} < 2$ at $f_{\text{esc,LyC}} \sim 0$ (top panel) and $R_{\text{MgII,Halo}}$ decreases with decreasing $f_{\text{esc,LyC}}$ (bottom panel). This illustrates that the Mg II doublet ratio is a sensitive proxy for $f_{\text{esc,LyC}}$. Hence, the Mg II doublet ratio can be a powerful tool to indicate LyC leakage and estimate the LyC escape fraction. In § 6.2, we will discuss this in detail and test further $R_{\text{MgII,Halo}}$ as a tracer of LyC escape.

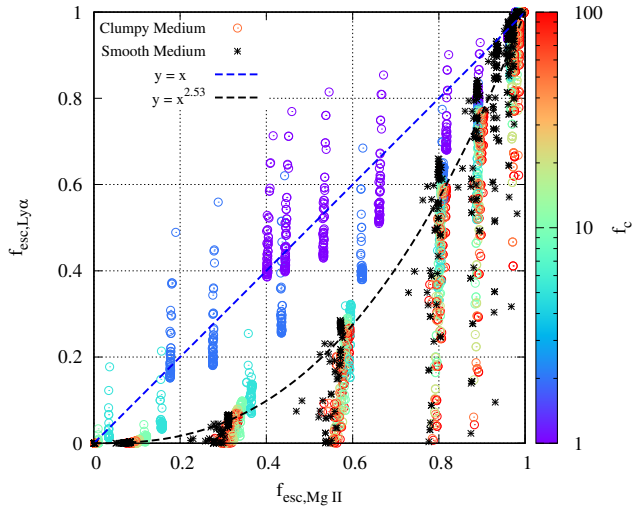


Figure 26. Escape fractions of Mg II and Ly α , $f_{\text{esc,MgII}}$ and $f_{\text{esc,Ly}\alpha}$, of the clumpy medium (color open circles) and the smooth medium (black star marks). The colors of the circles are for various f_c following the color bar on the right side. The blue and black dashed lines represent the function of $f_{\text{esc,Ly}\alpha} = f_{\text{esc,MgII}}$ and $f_{\text{esc,Ly}\alpha} = f_{\text{esc,MgII}}^{2.53}$, respectively. Recall that 2.53 is the $\tau_{\text{d,abs}}$ ratio of Ly α and Mg II. At $f_c < 10$, $f_{\text{esc,Ly}\alpha}$ is comparable to $f_{\text{esc,MgII}}$ because the surface scattering effect for Ly α is stronger than for Mg II due to $N_{\text{HI}} \gg N_{\text{MgII}}$.

6 DISCUSSION

6.1 Mg II & Ly α escape fractions

The escape fraction of radiation is generally given by $f_{\text{esc}} = \exp(-\tau_{\text{d,abs}})$ where $\tau_{\text{d,abs}} = \int ds \sigma_{\text{d,abs}} n_{\text{d}}$; $\sigma_{\text{d,abs}}$ and n_{d} are the dust absorption cross section and dust number density, respectively. Importantly, however, the integral is carried out along the trajectory of the photon and thus is highly non-trivial for resonant line photons.⁵

Specifically, comparing the escape fractions of Mg II and Ly α , we can see three effects at play:

- (i) the dust absorption cross section of Ly α is higher than for Mg II, generally resulting in lower escape fractions. In particular, $\sigma_{\text{d,abs}}^{\text{Ly}\alpha} \approx 2.53 \sigma_{\text{d,abs}}^{\text{MgII}}$ in the Milky Way and even larger differences in low metallicity environments (the ratio is, e.g., 3.8 and 9.3 in the LMC and SMC dust models, respectively; [Draine 2003a,b](#)). Note that this effect alone can affect the escape fraction by orders of magnitude (recall that, e.g., $\exp(-9) \approx 10^{-4}$), for instance, at high- z . We illustrate this point in [Fig. A1](#) and [A2](#) of [Appendix A](#), where we compare escape fractions of Mg II and Ly α using the MW, LMC, and SMC dust models assuming a monochromatic source.
- (ii) in addition, another effect leading to a decrease in Ly α escape fraction is, of course, that the path length l_{path} of Ly α is generally longer than that of Mg II because $N_{\text{HI}} \gg N_{\text{MgII}}$.

⁵ Note that the number of scatterings does not enter directly into f_{esc} , i.e., it is not the case that photons that scatter more necessarily have a lower f_{esc} as often assumed.

It is important to note, though, that while for moderately optically thin systems, photons escape via a ‘single flight’ ([Osterbrock 1962](#)), thus, $l_{\text{path}} \sim R$, i.e., the extent of the system, for extremely optically thick media ($\tau_0 \gtrsim 10^5$; i.e., when Ly α photons escape via excursion) l_{path} is only increased by a factor of $x_{\text{peak}} \approx 6.5(N_{\text{HI}}/10^{19} \text{ cm}^{-2})^{1/3}$ for $T = 10^4 \text{ K}$ ([Adams 1972](#); [Neufeld 1990](#)). Hence, while the number of scatterings (which, for Ly α in this regime, is $\sim \tau_0$) is increased by orders of magnitude, the increase in total path length – and thus dust absorption optical depth – is typically only a factor of few. We show this explicitly in [Fig. 8](#) and [§ 3.1.2](#), where we compare l_{path} of Mg II K and H lines measured from the simulations.

- (iii) Lastly, in a multiphase medium Ly α can undergo surface scatterings off of cold and dense regions, thus preventing the exposure to dust grains ([Neufeld 1991](#); [Hansen & Oh 2006](#); [Gronke et al. 2017](#)). We explicitly show that this effect exists in Mg II RT in [Fig. 19](#) and [§ 4.3.2](#). The effect of scattering becomes strong when the optical depth of the cold region increases. Therefore, as this effect would be weaker for Mg II photons due to $N_{\text{HI}} \gg N_{\text{MgII}}$, it would increase the Ly α escape fraction with respect to Mg II.

We show an overview of escape fractions computed in a range of smooth and clumpy models in [Fig. 26](#) (with the color coding corresponding to different values of f_c). In this figure, all three effects described above can be seen at play. Overall, the Ly α escape fraction is lower than that of Mg II; especially the smooth media simulations (indicated with black star marks) cluster around the $f_{\text{esc,Ly}\alpha} = f_{\text{esc,MgII}}^{2.53}$ curve, i.e., can be explained by the higher dust optical depth for Ly α (point (i) above). However, a substantial part of smooth and clumpy runs with $f_c \gtrsim 10$ show an even lower Ly α escape fraction – due to a longer escape trajectory (point (ii) above). Only a fraction of runs with $f_c \lesssim 10$ shows larger Ly α than Mg II escape fractions since the effect of surface scattering in Ly α RT is stronger than that of Mg II due to $N_{\text{HI}} \gg N_{\text{MgII}}$ (point (iii) above). Here, a higher column density simultaneously causes a longer path length and stronger surface scattering effect, which can decrease and increase f_{esc} , respectively. Thus, the clumpiness (i.e., f_c) is crucial to understanding the relation between f_{esc} of Ly α and Mg II.

Note that interestingly, some observational studies report that they found $f_{\text{esc,MgII}}$ comparable or even smaller than $f_{\text{esc,Ly}\alpha}$ ([Henry et al. 2018](#); [Xu et al. 2023](#)). Given the above discussion, this could be evidence of surface scatterings at play. Note that this can only be achieved if the medium is clumpy with only a few clumps per line-of-sight and the velocity dispersion is not too large ([Laursen et al. 2013](#); [Gronke & Oh 2018](#)). In principle, the ratio of escape fractions can give us interesting insights into the geometry of the scattering medium.

6.2 Mg II as a proxy for LyC leakage

The escape of LyC radiation in order to reionize the Universe is one of the main outstanding puzzles at high- z (see reviews [Robertson et al. 2010](#); [Madau & Dickinson 2014](#); [Eldridge & Stanway 2022](#)). Thus far, only a few individual LyC leakers have been found ([Shapley et al. 2016](#); [Izotov et al. 2016, 2018b](#); [Vanzella et al. 2016, 2018](#); [Rivera-Thorsen et al. 2017, 2019](#); [Kim et al. 2023](#)), and progress comes from survey ob-

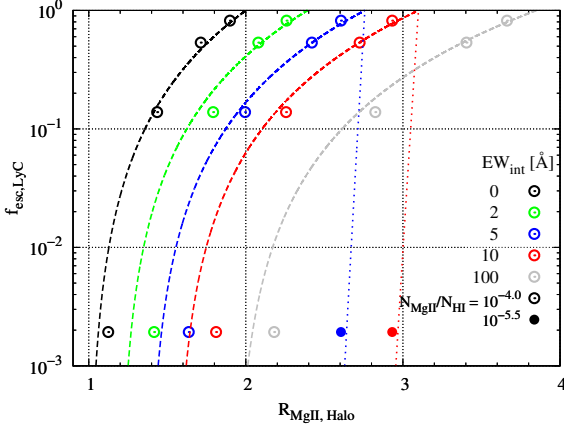


Figure 27. The LyC escape fraction $f_{\text{esc,LyC}}$ as a function of the halo doublet ratio $R_{\text{MgII,Halo}}$ for various intrinsic equivalent widths of the in situ emission $\text{EW}_{\text{int}} = 0$ (the flat continuum), 2, 5, 10, and 100 Å at $v_{\text{exp}} = 100 \text{ km s}^{-1}$. Open and filled circles represent the Mg II fraction $N_{\text{MgII}}/N_{\text{HI}} = 10^{-4}$ and $10^{-5.5}$, respectively. The color dashed (dotted) lines are the analytic solution in Eq. (21) assuming $N_{\text{MgII}}/N_{\text{HI}} = 10^{-4}$ ($10^{-5.5}$). In order to get $f_{\text{esc,LyC}}$ from $R_{\text{MgII,Halo}}$, the intrinsic EW and the Mg II fraction are crucial parameters.

servation (Steidel et al. 2001, 2018; Flury et al. 2022a) and proxy observables. The latter is particularly needed since, already at intermediate redshift, the IGM becomes opaque to ionizing radiation making direct detections of LyC hard to impossible.

Since – as Ly α – the Mg II doublet is susceptible to cold, neutral $\sim 10^4 \text{ K}$ gas, it is a natural proxy for probing ionizing photon escape. This connection has been explored in work by Henry et al. (2018); Chisholm et al. (2020); Izotov et al. (2022); Xu et al. (2023) who suggest that a doublet ratio of $R_{\text{MgII}} < 2$ represents low LyC escape fractions. Their argument is based on the fact that the optical depth of the K line is two times greater than that of the H line, leading to $R_{\text{MgII}} < 2$ for larger optical depths, whereas, for negligible amounts of scattering, one would observe the fiducial value of $R_{\text{MgII}} \sim 2$.

Later, Katz et al. (2022) tested this relationship between R_{MgII} and LyC escape fraction using cosmological hydrodynamical simulation post-processed with Mg II radiative transfer. They concluded that the Mg II doublet ratio could be used as an indicator of LyC leakers for galaxies in the optically thin regime.

However, as pointed out above, there are other important physical mechanisms – mainly strong ($|v| \gtrsim 700 \text{ km s}^{-1}$) kinematics (§ 3.2.3), dust (§ 3.1.3), and scattered stellar continuum (§ 5) – that influence strongly the emergent doublet ratio, and thus the inferred LyC escape fraction.

To recap: we showed in Fig. 7 & § 3.2.3 how in- or out-flows close to or exceeding the doublet separation can in- or decrease R_{MgII} , respectively. Furthermore, for intermediate optical depths ($0.5 \lesssim \tau \lesssim 10$), the path lengths of the H and K lines are different, leading to different dust attenuation and thus a decreased R_{MgII} (cf. § 3.1.3). And lastly, we showed in § 5 that scattered stellar continuum can also lower the doublet ratio.

Because of the restricted range of parameters, the former

two effects can influence R_{MgII} ; we focus here on the latter one. However, we do want to point out that also the other effects can play a role and lead to a potentially wrongly inferred $f_{\text{esc,LyC}}$. We discuss the effect of strong kinematics on the doublet ratio further in § 6.4.

In § 5, we showed that the doublet ratio of from a pure flat continuum ($\text{EW}_{\text{int}} = 0$) is generally < 2 , even approaching ~ 1 in the limit where both K and H lines are very optically thick ($\tau_0 > 10$). Generally, this reduction of R_{MgII} is also present with $\text{EW}_{\text{int}} > 0$ as the emergent spectrum is a composition of the flat continuum ($R_{\text{MgII}} < 2$) as well as the Gaussian part ($R_{\text{MgII}} \sim 2$). Note that this effect is generally at play for $\tau_0 \gtrsim 10$, i.e., column densities $N_{\text{MgII}} \gtrsim 10^{14} \text{ cm}^{-2}$. Consequently, at this high N_{MgII} , where the LyC escape $f_{\text{esc,LyC}} \approx 0$ (cf. Fig. 24), $R_{\text{MgII}} < 2$ due to the contribution of the continuum pumping. Albeit for somewhat different reasons, it is, therefore, consistent with the picture of the pioneering observational work quoted above, which suggested R_{MgII} as a proxy for LyC leakage.

On top of the previously explored $R_{\text{MgII}} < 2$ proxy for LyC escape, in § 5.2.2, we highlight an additional measure to constrain the column density and, thus, ionizing photon escape: the doublet ratio in the halo. As this observable only consists of scattered radiation, it follows a similar trend for $N_{\text{MgII}} \gtrsim 10^{14} \text{ cm}^{-2}$, i.e., there $R_{\text{MgII,Total}} \sim R_{\text{MgII,Halo}} < 2$. However, for smaller column densities – that is, in the LyC escape relevant regime – the integrated doublet ratio flattens to ~ 2 whereas the halo part shows $R_{\text{MgII,Halo}} > 2$ (cf. Fig. 25). This is because, in this regime, the lines are not saturated (i.e., $\tau_0 < 1$).

These results suggest a novel ‘smoking gun’ signature for ionizing photon escape: if $R_{\text{MgII,Halo}} > 2$, the column densities are low ($N_{\text{MgII}} \lesssim 10^{13.5} \text{ cm}^{-2}$) implying $f_{\text{esc,LyC}} \gtrsim 0.2$ (for $N_{\text{MgII}}/N_{\text{HI}} \sim 10^{-4}$; cf. Fig. 24 which shows a clear $N_{\text{MgII}} - R_{\text{MgII,Halo}}$ correlation). Naturally, the exact numbers do depend on, e.g., the intrinsic equivalent width of the line (cf. Fig. 25).

We show the relation between $R_{\text{MgII,Halo}}$ and $f_{\text{esc,LyC}}$ explicitly in Fig. 27 for a suite of our smooth and clumpy models. Here, we show $f_{\text{esc,LyC}}$ as a function of the halo R_{MgII} for various $\text{EW}_{\text{int}} = 0$ (flat continuum), 2, 5, 10, and 100 Å (cf. Eq. (17)). We also show how the correlation changes when considering different Mg II abundances. It is clear from Fig. 25 that independent of on (non) multiphase structure, the radiative transfer models follow a clear $R_{\text{MgII,Halo}} - f_{\text{esc,LyC}}$ trend – which is shifted to higher R_{MgII} for larger EW_{int} .

From the equations derived in § 5.2.2 for the doublet ratio, we can write down a simple formulation for this trend. Rewriting Eq. (19) to give N_{MgII} as a function of $R_{\text{MgII,Halo}}$, and adopting $f_{\text{esc,LyC}} = \exp(-\tau_{\text{LyC}}) \approx \exp[-N_{\text{HI}}/(1.6 \times 10^{17} \text{ cm}^{-2})]$, one can obtain

$$f_{\text{esc,LyC}} \approx \exp \left[-2.2 \frac{N_{\text{MgII}}}{3.6 \times 10^{13} \text{ cm}^{-2}} \left(\frac{f_{\text{MgII/II}}}{10^{-4}} \right)^{-1} \right]. \quad (21)$$

Here, N_{MgII} is the Mg II column density, which can be analytically estimated using the halo doublet ratio (cf. Eq. (19)) and is then by

$$\frac{N_{\text{MgII}}}{3.6 \times 10^{13} \text{ cm}^{-2}} = -\ln \left(\frac{R_{\text{MgII,Halo}}}{R_{\text{MgII,int}}} - 1 \right) \left(\frac{v_{\text{exp}}}{100 \text{ km s}^{-1}} \right) \quad (22)$$

where $R_{\text{MgII,int}} \approx 2$ is the fiducial doublet ratio (cf. § 2.3).

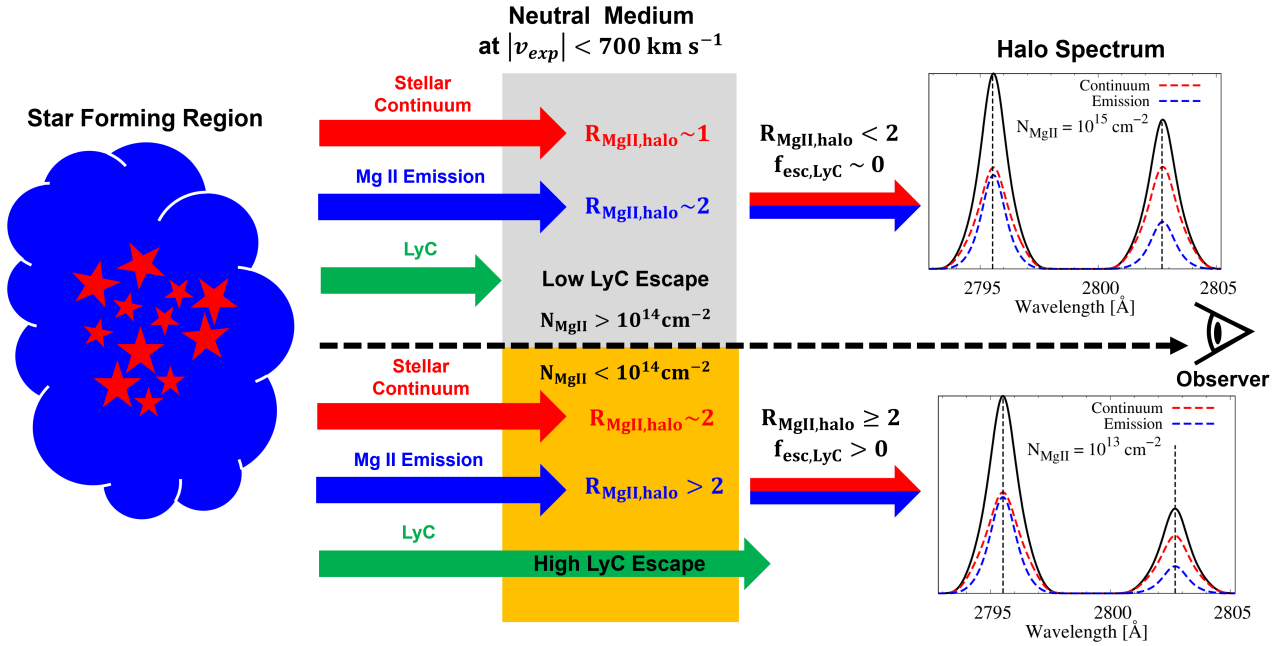


Figure 28. Schematic illustration to demonstrate the halo doublet ratio of Mg II lines $R_{\text{MgII,Halo}}$ as a tracer of LyC escape. A small doublet ratio $R_{\text{MgII}} < 2$ can represent the low LyC escape fraction as shown in Fig. 27. On the left side, a star-forming region emits Mg II in situ emission (blue), stellar continuum (red), and LyC (green). Intrinsically, the doublet ratio is two for recombination or collisional excitation. The gray and orange neutral media divided by the black dashed line represent $N_{\text{MgII}} > 10^{14} \text{ cm}^{-2}$ and $< 10^{14} \text{ cm}^{-2}$, respectively, with moderate ($|v_{\text{exp}}| < 700 \text{ km s}^{-1}$) kinematics. The upper and bottom right panels are the halo spectra at $N_{\text{MgII}} = 10^{15}$ and 10^{13} cm^{-2} , respectively, with the black solid lines indicating the total spectrum and the red (blue) dashed lines just the contribution of the stellar continuum (the in situ emission). The spectra in the upper panel are identical to the halo spectra in the right panel of Fig. 23. In the high N_{MgII} regime ($> 10^{14} \text{ cm}^{-2}$), the doublet ratios of the halo spectra from the in situ emission and stellar continuum are ~ 2 and ~ 1 (also see Fig. 23 & § 5.2). In the low N_{MgII} regime, $R_{\text{MgII,Halo}}$ is higher than 2, as discussed in § 5.2 and shown in Fig. 25.

Eq. (21) reproduces our radiative transfer simulations well (shown as dashed lines in Fig. 27 and can be used to convert observed halo doublet ratios to ionizing escape fractions. This can, in principle, also be applied for high redshifts (where the direct detection of ionizing photons is impossible). However, note that for very low magnesium abundances $f_{\text{MgII/II}} < 10^{-4.5}$, Mg II scattering is negligible due to small $N_{\text{MgII}} (< 10^{13} \text{ cm}^{-2})$ at the canonical N_{HI} for LyC ($1.6 \times 10^{17} \text{ cm}^{-2}$) as shown in Fig. 27.

A visual summary of the discussed relation and our new proxy of ionizing photon escape $R_{\text{MgII,Halo}}$ is shown in Fig. 28. There we show schematically the process leading to low or high LyC escape and the corresponding Mg II halo spectrum.

6.3 Connection to other resonant lines

In this study, we focused on the resonant Mg II and Ly α lines. However, also other resonant lines are commonly studied in astrophysics. For instance, Hayes et al. (2016) reported the detection of an extended O VI nebula with a size larger than the Ly α counterpart. They speculate in their work that this could be due to the scattering of O VI photons in the hot CGM at the temperature of several 10^5 K. Furthermore, Berg et al. (2019) noted that the scattering with C IV causes the profile of C IV emission to be broader than non-resonant He II emission. Those studies show that metal doublets are

affected by radiative transfer processes and thus carry additional information about the gas properties within them.

The behavior and physical properties of scattered metal doublets are similar to Ly α because of the atomic physics of Mg II, C IV, O VI, N V, and S IV atoms, which have one electron in the outer orbit. We described the atomic physics of Mg II in detail in § 2.1, and analogous arguments apply for the other metal doublets. For instance, C IV $\lambda\lambda$ 1549, 1551, O VI $\lambda\lambda$ 1032, 1038, N V $\lambda\lambda$ 1239, 1243, and S IV $\lambda\lambda$ 1393, 1402 have the same atomic structure composed of two transitions, K ($S_{1/2} - P_{3/2}$) and H ($S_{1/2} - P_{1/2}$). Furthermore, due to their resonant nature, the doublets of highly ionized atoms can undergo scatterings before escaping the system. It is also important to note that the ratio of all the oscillator strengths is ~ 2 , implying that the intrinsic doublet ratio is 2 when the emission lines originate from the collisional excitation and recombination. This canonical ratio also implies the same difference in scattering optical depths as described here for Mg II and the associated physical processes discussed.

The main differences between other resonant lines lie in the energy level as well as in the velocity separation between the K and the H line. In Table 2, we list a selection of Ly α and metal resonance doublets commonly used in astrophysics. One can see that the ionization energy ranges from 13.6 eV to 138 eV, i.e., probing temperatures from several 10^3 K to several 10^5 K. This implies that multiwavelength access to these emission lines can constrain the multiphase nature of the CGM – as often already done in absorption line studies

Table 2. Atomic data of Ly α and metal resonance doublets. λ_K and λ_H are atomic line center wavelength of K and H lines (second and third columns). f_K and f_H are oscillation strengths of K and H lines (fourth and fifth columns). $\Delta V_{K,H}$ is the velocity separation of the K and H lines (sixth column). E_{ion} is the ionization energy of the atoms (seventh column). A is the ionization energy to create atoms, e.g., the Mg I ionization energy in the case of Mg II. (eighth column). n/n_H is the fraction of the atom in the solar metallicity (ninth column).

Atom	λ_K^a	λ_H^a	f_K	f_H	$\Delta V_{K,H}^b$	E_{ion}^c	$E_{\text{ion}}^c{}^d$	$\log(n/n_H)$
Ly α	1215.668	1215.674	0.278	0.139	1.3	13.6	–	–
Mg II	2796.4	2803.5	0.608	0.303	760	15.0	7.64	–4.46*
C IV	1548.2	1550.8	0.190	0.0952	500	64.5	47.9	–3.61 [†]
O VI	1031.9	1037.6	0.133	0.0660	1660	138	114	–3.31 [†]
N V	1238.9	1242.8	0.157	0.0782	970	97.9	77.5	–4.07 [†]
Si IV	1393.8	1402.8	0.513	0.255	1926	45.1	33.5	–4.46*

a: vacuum wavelength in Å, b: velocity separation of K and H lines $\Delta V_{K,H} \sim (\lambda_K - \lambda_H)c/\lambda_K$ in km s^{-1} , c, d: ionization energy in eV, *: Holweger (2001), [†]: Grevesse & Sauval (1998)

(e.g., Fox et al. 2007, 2009; Crighton et al. 2015; Rubin et al. 2015; Mas-Ribas et al. 2017; or review by Tumlinson et al. 2017).

It is also evident from Table 2 that the velocity separation of the K and H lines varies between 1.3 km s^{-1} for Ly α and 1657 km s^{-1} for O VI. As we discussed already in § 2.1, this separation for Ly α is too small to be observed. However, for the other lines, this means that our conclusions drawn in § 3.2 have to be rescaled from $\sim 760 \text{ km s}^{-1}$ for Mg II to the respective doublet separation $\Delta V_{K,H}$, which can yield interesting constraints on galactic flows. However, higher column density ($> 10^{14} \text{ cm}^{-2}$) is required to utilize the doublet ratio of other lines (O VI, C IV, and N V) to indicate the strong outflow/inflow, since the oscillation strengths of the three doublets are 3–4 times less than Mg II. We will discuss other metal lines as a tracer of the galactic flows in the next section.

6.4 Metal doublet ratios as a probe of strong outflows

Galactic winds are a cornerstone in our theory of galaxy formation and evolution, but their energetics and extents are still debated (for reviews see, e.g., Veilleux et al. 2005, 2020; Rupke 2018).

As we show in § 3.2.3 for the example of Mg II, a strong change in the doublet ratio can be due to strong kinematics, i.e., larger than the doublet separation $\Delta V_{K,H}$; specifically outflows leading to $R_{\text{MgII}} < 2$ and inflows to $R_{\text{MgII}} > 2$. Although, in this work, we also discuss other mechanisms to alter the doublet ratio, such as scattering of the continuum photons, which can also decrease R_{MgII} , it is important to note that for all these processes, the doublet ratio is always higher than unity (see, e.g., Figures 7 and 20). Thus, a doublet ratio of less than unity is clear evidence of the strong outflows with velocities at least approaching $\Delta V_{K,H}$.

Table 2 summarizes the atomic data of Mg II and the three doublets of highly ionized atoms, C IV, O VI, N V, and Si IV with columns showing the velocity separation of the K & H lines, ionization energy, and the fraction of atom in the solar metallicity. Those three doublets have high ionization energies, $> 60 \text{ eV}$, and thus are more relevant for probing for a hot medium with $T > 10^5 \text{ K}$.

The emission of C IV doublet is a potentially good tracer of hot wind & CGM with $T \sim 10^5 \text{ K}$ because the C IV doublet has the smallest separation ($\sim 500 \text{ km s}^{-1}$) and strongest oscillation strength (~ 0.19) of three doublets of highly ionized atoms in Table 2. In Fig. 7, the Mg II doublet ratio significantly varies when the outflow/inflow velocity is higher than the velocity separation and $N_{\text{MgII}} \gtrsim 10^{14} \text{ cm}^{-2}$. Adopting the atomic data in Table 2, the C IV ratio becomes less than 2 when the outflow velocity $> 500 \text{ km s}^{-1}$ and a C IV column density $\gtrsim 3 \times 10^{14} \text{ cm}^{-2}$. The literature, Kafatos et al. (1985); Michalitsianos et al. (1988, 1992), reported that the ratio of C IV $\lambda 1549$ and $\lambda 1551$ is less than 1 in the IUE (International Ultraviolet Explorer; Boggess et al. 1978) spectra of symbiotic stars because of the strong outflow $> 600 \text{ km s}^{-1}$. This C IV ratio is too small to be explained by the scattering of the continuum. Consequently, these previous studies suggest the potential of the C IV doublet ratio as the indicator of the hot wind $> 500 \text{ km s}^{-1}$.

6.5 Spatially varying Mg II emission

As mentioned in the introduction, the spatially extended emission halo obtained by IFS such as MUSE, KCWI, and HETDEX allows us to investigate the spatial variation of Ly α (Claeysens et al. 2019; Leclercq et al. 2020; Guo et al. 2023a) and Mg II (Chisholm et al. 2020; Burchett et al. 2021; Dutta et al. 2023; Guo et al. 2023b). Additionally, polarized Ly α emission has been observed in spatially extended Ly α nebulae (Hayes et al. 2011; You et al. 2017; Kim et al. 2020), providing compelling evidence of scattering effects (Dijkstra & Loeb 2008; Eide et al. 2018; Chang et al. 2023). Given the similarity in atomic physics between Mg II and Ly α , it follows that Mg II emission is also subject to polarization through scattering. Using our radiative transfer code, we can study how the spectra, surface brightness, and even polarization pattern change in space.

Fig. 29 shows as an example the projected images of Mg II and Ly α for various column densities, N_{HI} & N_{MgII} . Note that here, we adopt a Gaussian point spread function with width $\sigma = 0.1R_H$ leading to an extended bright core in the central region. As expected, the SB profile of Mg II becomes more extended with increasing N_{MgII} because of the increased

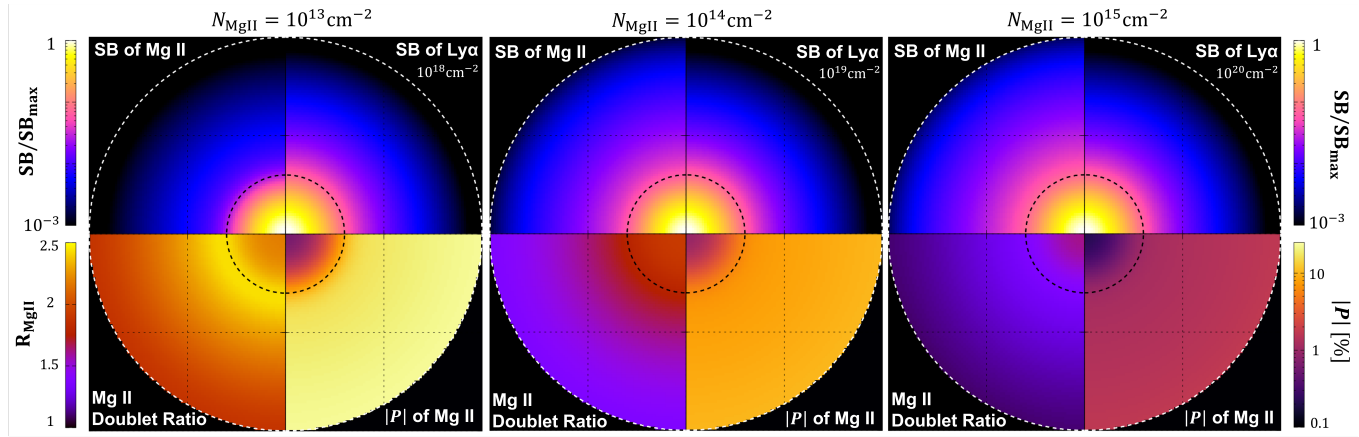


Figure 29. Projected images for three $N_{\text{MgII}} = 10^{13} \text{ cm}^{-2}$ (left), 10^{14} cm^{-2} (center), and 10^{15} cm^{-2} (right panel). v_{exp} , f_c , and $\tau_{\text{d,abs}}$ are fixed at 200 km s^{-1} , 100, and 0, respectively. The incident radiation consists of the flat continuum and the in situ emission with $\sigma_{\text{src}} = 100 \text{ km s}^{-1}$ and $\text{EW}_{\text{int}} = 5 \text{ \AA}$. Each panel is composed of four patches of the projected images, Mg II surface brightness (top left), Ly α surface brightness (top right), a doublet ratio R_{MgII} (bottom left), and a degree of polarization of Mg II (bottom right). $N_{\text{MgII}}/N_{\text{HI}} = 10^{-5}$ is assumed to get Ly α surface brightness. The seeing effect with the radius $0.1R_{\text{H}} = 10 \text{ kpc}$ is adopted as an angular scale at $z \approx 3$ is $\sim 7.855 \text{ kpc arcsec}^{-1}$ (Wright 2006). The black and white dashed lines represent the projected radius $0.2R_{\text{H}}$ and R_{H} , respectively. The inner region of the black dashed circle in the top patches is strongly affected by the seeing; typically, two times the radius for seeing (20 kpc $\sim 2 \text{ arcsec}$) but strongly dependent on the spatial resolution of the instrument and redshift. The bright core and the unpolarized feature in this inner region mainly originate from directly escaping photons at the central source.

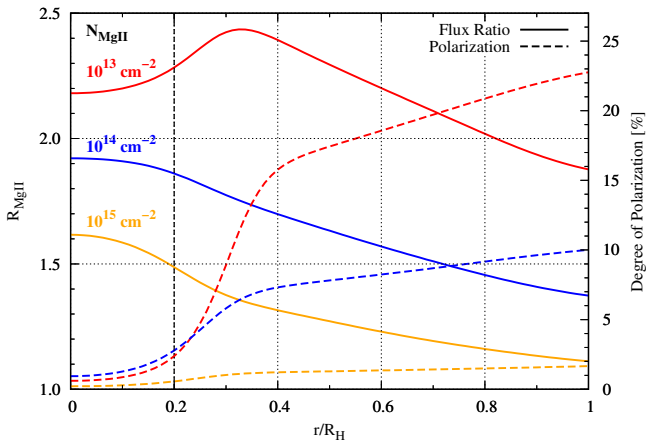


Figure 30. The doublet ratio R_{MgII} (solid) and the degree of polarization $|P|$ (dashed line) as a function of the projected radius r/R_{H} . The profiles are extracted from the projected images in Fig. 29. Each color represent $N_{\text{MgII}} 10^{13}$ (red), 10^{14} (blue) and 10^{15} cm^{-2} (orange).

scattering rate. The overall R_{MgII} decreases with increasing N_{MgII} because of the contribution of the continuum as discussed in § 5.2 (cf. Fig. 24). The degree of polarization $|P|$ of Mg II also decreases with increasing N_{MgII} since the multiple scattering process decreases the strength of polarization (Chandrasekhar 1960; Chang et al. 2017; Seon et al. 2022; Chang et al. 2023).

Fig. 30 shows the profiles of R_{MgII} and $|P|$ as a function of the projected radius r_p/R_{H} for three $N_{\text{MgII}} = 10^{13}$, 10^{14} , and 10^{15} cm^{-2} . When $N_{\text{HI}} = 10^{13} \text{ cm}^{-2}$, R_{MgII} increases until $\sim 0.3r/R_{\text{H}}$ and the peak value of R_{MgII} is higher than 2. In

this low N_{HI} , the scattering of the in situ emission causes the high doublet ratio $R_{\text{MgII}} > 2$ near $0.2r/R_{\text{H}}$ as shown in the right panel of Fig. 24. At $N_{\text{HI}} = 10^{14}$ and 10^{15} cm^{-2} , R_{MgII} decreases with increasing r/R_{H} . Since the outflow velocity in our sphere geometry is proportional to the radius, the outer Mg II halo mainly causes the scattering of the flat continuum. Thus, R_{MgII} in the outer halo is smaller than in the inner region.

Fig. 30 shows the dependence on N_{MgII} of $|P|$, which increases radially outward. In the inner region with $r/R_{\text{H}} < 0.2$, $|P|$ is less than 5 % because seeing effects spread unpolarized photons directly escaping from the central source. However, the outer halo is strongly polarized over 10% at $N_{\text{MgII}} < 10^{15} \text{ cm}^{-2}$. Thus, if Mg II emission mainly comes from scattering, Mg II is strongly polarized ($>10\%$). In the case of high $N_{\text{MgII}} = 10^{15} \text{ cm}^{-2}$, if it is not strongly polarized, the evidence of the scattering is imprinted on the spectral profile.

In § 6.2, we discussed $R_{\text{MgII,Halo}}$ as an indicator of LyC escape since the halo spectrum is composed of Mg II photon undergoing scattering. However, in cases where intrinsic Mg II emission is spatially extended, distinguishing scattered Mg II photons becomes challenging from an observational perspective. Consequently, the polarization of Mg II can serve as a valuable tool for estimating the halo doublet ratio of Mg II, $R_{\text{MgII,Halo}}$. Therefore, the measurement of the doublet ratio in polarized Mg II nebulae can serve as an analogous quantity to $R_{\text{MgII,Halo}}$.

6.6 Probing the ‘clumpiness’ of the CGM through resonant lines

Many radiative transfer studies focus on the effect of column density and kinematics on emergent properties. However, also the ‘clumpiness’ of the structure plays a crucial role in shap-

ing them – and given most astrophysical systems (such as the ISM and CGM) are multiphase, one cannot neglect this property in our studies.

The specific parameter governing radiative transfer through a clumpy medium is f_c , the mean number of clumps per line-of-sight (Hansen & Oh 2006). Previous studies have focused on Ly α radiative transfer through a clumpy medium and have found that, in general, the observable information (e.g., spectrum, surface brightness, escape fraction, polarization) is different from those in the smooth medium (e.g., Neufeld 1991; Hansen & Oh 2006; Laursen et al. 2013; Duval et al. 2014; Gronke et al. 2016; Chang et al. 2023). However, if f_c is greater than some critical number of clumps $f_{c,\text{crit}}$ (which is a function of the column density and the kinematics), a ‘phase transition’ occurs, and the emergent observables of a clumpy medium are the same as the ones of a homogeneous medium (Gronke et al. 2017; Chang et al. 2023).

In § 4.3.1, we extend these previous studies and investigate the radiative transfer of Mg II in a clumpy, multiphase medium. We find that akin to Ly α , a critical number of clumps exists, above which the escaping Mg II spectrum is close to the homogeneous one. We also provide an analytic estimate for this $f_{c,\text{crit}}$ in Eq. (10) (as well as update the Ly α ones; Eq. (8)) and show that it reproduces the simulated results reasonably well.

This provides a potentially interesting probe to study the clumpiness of the CGM. As most Ly α spectra are well fit using homogeneous models (see, e.g., Verhamme et al. 2008; Karman et al. 2017; Gronke 2017), this can be interpreted as $f_c > f_{c,\text{crit}}$ in these systems (Gronke et al. 2017). Such a clumpy CGM is supported by other observables such as quasar absorption line studies (e.g., Crighton et al. 2015; Lan & Fukugita 2017) – as well as by theoretical models showing that cold clumps naturally fragment in a hot environment (McCourt et al. 2018; Liang & Remming 2020; Gronke et al. 2022).

However, importantly, all these probes can only provide lower limits on the ‘clumpiness’ or the mean number of clumps, i.e., the smallest scale or characteristic size of this cold gas is unknown. As we show in § 4.3.1 (cf. Fig. 18), Mg II usually has a different $f_{c,\text{crit}}$ compared to Ly α . This implies that, in principle, one could use a combination of these two lines to provide both an upper and lower bound to f_c and thus constrain the ‘clumpiness’ of the CGM. This could be, for instance, possible for a static medium with $N_{\text{HI}} = 10^{20.5} \text{ cm}^{-2}$ and $N_{\text{MgII}} = 10^{15} \text{ cm}^{-2}$ for which the critical covering factors are $f_c \sim 20$ and ~ 100 for Ly α and Mg II, respectively (see Fig. 17). Thus, if for such a medium a double peaked Ly α profile, but a single peaked Mg II profile is observed, the f_c can be constrained to lay between these two values. Naturally, this prediction is still quite theoretical and would have to be further specified using more complex kinematics and gas structures.

7 CONCLUSION

Resonant lines provide us with an important window into the low surface brightness regime and, thus, allow us to study high redshift objects as well as the dim outskirts of galaxies. As these fields are the focus of many future instruments, telescopes, and surveys – observationally, progress is rapid,

and we now know already, e.g., much more about the galactic ecosystem than a decade ago. To interpret this flood of data, it is therefore important that this development is accompanied by theoretical progress.

This work extended our Monte Carlo radiative transfer code in Chang et al. (2023) to include Mg II doublet. Since the atomic structures of Mg II & Ly α with their H ($S_{1/2} - P_{1/2}$) and K ($S_{1/2} - P_{3/2}$) transitions, are identical, we could implement Mg II scattering based on the atomic physics of Ly α (§ 2).

Our simulation code ‘RT-scatter’ supports arbitrary 3D gas configurations and kinematics as input. It supports both a Cartesian grid as well as a multiphase ‘clumpy’ medium with many ($\geq 10^9$) clumps. As for the latter, a ‘brute force’ method would be memory intensive; we implement ‘subgrid’ clumps that can exist within the cells. The code furthermore supports the calculation of the polarization behavior (adopting the numerical method in Seon et al. 2022) and dust scattering and extinction using the MW as well as the SMC and LMC dust models in Draine (2003a,b) (see Appendix A). Notably, after the submission of this paper, Seon (2023) appeared, which also studies Mg II radiative transfer. The author focuses on spherical and cylindrical geometries with a uniform density. Hence, the two studies are highly complementary.

With this code, we study the joined Mg II and Ly α escape in both homogeneous (§ 3) and clumpy (§ 4) media. Our main focus is the emergent Mg II lines. In particular, we systematically study (i) the Mg II doublet ratio in various environments, (ii) the general spectral shape, and (iii) the Mg II escape fraction. Apart from the scattering geometry, we also vary the intrinsic source between a monochromatic light, a Gaussian emission, and a flat continuum to study how the observables’ dependence on it.

Our main conclusions are the following:

- Because typically H I column densities in neutral media are much greater than Mg II column densities, the emergent Mg II spectra differ from Ly α spectra, even though the atomic physics of the two lines are similar. As N_{HI} & N_{MgII} increases in the outflow, the spectral peak of Ly α gets redshifted while the peak of Mg II is always near the systematic velocity (Fig. 9). In the dusty medium, the scattered red wings of Ly α and Mg II show opposite effects, i.e., are weakened and strengthened, respectively (Fig. 11).
- In general, the Mg II escape fraction $f_{\text{esc,MgII}}$ is higher than the Ly α escape fraction $f_{\text{esc,Ly}\alpha}$ because $N_{\text{HI}} \gg N_{\text{MgII}}$ and the dust optical depth of Ly α is at least ~ 2.53 times that of Mg II (see § 3.2 and Fig. 5 as well as the discussion in § 6.1). In addition, the higher column density causes a longer path length, which induces more dust extinction. However, in a moderately clumpy medium, when an incident photon meets an optically thick clump, the photon suffers scattering on the surface of the clump with a shorter path length. It is surface scatterings that increase escape fractions (see § 4.3 and Fig. 15). The effect of these surface scatterings is stronger for Ly α than in Mg II photons – again due to $N_{\text{HI}} \gg N_{\text{MgII}}$. In summary, when the covering factor $f_c < 10$ and $N_{\text{HI}} > 10^{20} \text{ cm}^{-2}$ ($N_{\text{MgII}} > 10^{14.5} \text{ cm}^{-2}$), $f_{\text{esc,Ly}\alpha} \sim f_{\text{esc,MgII}}$ due to the surface scattering (see § 6.1 and Fig. 26). In conclusion, the Ly α and Mg II escape fractions are correlated in a non-trivial fashion (cf. § 6.1 for discussion on f_{esc}).
- In a clumpy medium, a ‘critical covering factor’ $f_{c,\text{crit}}$ above

which the radiative transfer of multiphase matches the one through a homogeneous medium also exists for Mg II. However, generally $f_{c,crit}$ for Mg II and Ly α do not match (see § 4.3.1 and Fig. 18). We provide analytic solutions of $f_{c,crit}$ as a function of v_{exp} , and column densities in Eq. (8) and (10) for Ly α and Mg II, respectively. The differing $f_{c,crit}$ values can be used to probe the clumpiness of the CGM, which we discuss in § 6.6.

- The doublet ratio of Mg II, R_{MgII} , can be a tracer for strong in- or outflows. The ratio can be de- or increased from its intrinsic doublet ratio of ~ 2 due to outflowing and inflowing media, respectively, if $|v_{exp}| > 700 \text{ km s}^{-1}$ and $N_{MgII} > 10^{14} \text{ cm}^{-2}$ (see Fig. 13). This is because of the fact that if the kinematic velocity of the scattering medium is larger than the velocity separation of Mg II doublet, $\sim 750 \text{ km s}^{-1}$, K/H photons are scattered by the H/K transition of the outflowing/inflowing Mg II atom (see Fig. 10). However, this trend weakens at the clumpy medium with low f_c (see Fig. 20). While we also discuss other effects that alter R_{MgII} (see points below), strong outflows are the only ones that can lead to $R_{MgII} < 1$. This can be used as a complementary probe for the energetics of galactic winds (cf. § 6.4).
- A particularly interesting case is the Mg II line formation due to scattered stellar continuum photons. In this scenario, R_{MgII} is lowered from its intrinsic value of 2, and N_{MgII} determines R_{MgII} (see § 5). Assuming a flat continuum, the Mg II emission appears by scattering of Mg II leading to a P-Cygni-like profile (Fig. 21); the strength of the emission depends on N_{MgII} . In the low N_{MgII} regime ($< 10^{14} \text{ cm}^{-2}$), the scattering rate of photons near the K transition is less than unity and two times higher than near the H transition. In the high N_{MgII} regime ($> 10^{14} \text{ cm}^{-2}$), both scattering rates of photons near the K and H transition are close to unity. Thus, R_{MgII} decreases with increasing N_{MgII} (Fig. 22).
- We also study the most general and realistic emission case and combine in-situ Gaussian Mg II emission and a stellar continuum contribution. Also, in this scenario, the doublet ratio R_{MgII} on N_{MgII} as well as the intrinsic equivalent width of the in situ emission EW_{int} (see § 5.2 and Fig. 24). Here, we also propose a more sensitive measure of the gas properties, the doublet ratio of the halo $R_{MgII,Halo}$. Since the halo photons are only composed of scattered photons, $R_{MgII,Halo}$ is a less ‘contaminated’ probe and can be used to constrain, e.g., the cold gas column density. This is particularly interesting for the constraint of ionizing photons (cf. discussion in § 6.2). We find that the halo double ratio $R_{MgII,Halo} \geq 2$ is a clear proxy for ionizing photon escape. For this purpose, we provide an analytic fit relating the column density (§ 5.2, Eq. 19) as well as the ionizing escape fraction (Eq. 21) with $R_{MgII,Halo}$. We show that those solutions match our simulated results well.

We expect that other metal resonance doublets in the UV regime, O VI $\lambda\lambda$ 1032, 1038, N V $\lambda\lambda$ 1239, 1243, and C IV $\lambda\lambda$ 1549, 1551, can show similar behavior and trends as discussed here for Mg II. They can, therefore, provide interesting constraints on the warm CGM with $T \gtrsim 10^5 \text{ K}$. We plan to investigate the scattering processes of other metal doublets in future work. Furthermore, we hope to adopt our simulated results shown here to model and analyze the observations of spatially extended Mg II emission.

ACKNOWLEDGEMENTS

The authors thank the anonymous referee for a detailed report, which significantly improved the quality of the work. The authors also thank Hee-Won Lee and Kwang-II Seon for their insightful comments that greatly contributed to the completion of this work. MG thanks the Max Planck Society for support through the Max Planck Research Group.

DATA AVAILABILITY

Data related to this work will be shared on reasonable request to the corresponding author.

REFERENCES

- Adams T. F., 1972, *ApJ*, **174**, 439
 Adams T. F., 1975, *ApJ*, **201**, 350
 Ahn S.-H., Lee H.-W., Lee H. M., 2001, *ApJ*, **554**, 604
 Ahn S.-H., Lee H.-W., Lee H. M., 2002, *ApJ*, **567**, 922
 Arrigoni Battaia F., Hennawi J. F., Prochaska J. X., Cantalupo S., 2015, *ApJ*, **809**, 163
 Arrigoni Battaia F., Hennawi J. F., Prochaska J. X., Oñorbe J., Farina E. P., Cantalupo S., Lusso E., 2019, *MNRAS*, **482**, 3162
 Bacon R., et al., 2010, in McLean I. S., Ramsay S. K., Takami H., eds, Society of Photo-Optical Instrumentation Engineers (SPIE) Conference Series Vol. 7735, Ground-based and Airborne Instrumentation for Astronomy III. p. 773508 ([arXiv:2211.16795](https://arxiv.org/abs/2211.16795)), doi:10.1117/12.856027
 Berg D. A., Chisholm J., Erb D. K., Pogge R., Henry A., Olivier G. M., 2019, *ApJ*, **878**, L3
 Boggess A., et al., 1978, *Nature*, **275**, 372
 Bouché N., et al., 2016, *ApJ*, **820**, 121
 Burchett J. N., Rubin K. H. R., Prochaska J. X., Coil A. L., Vaught R. R., Hennawi J. F., 2021, *ApJ*, **909**, 151
 Byrohl C., Gronke M., 2020, *A&A*, **642**, L16
 Byrohl C., Nelson D., 2022, *arXiv e-prints*, p. [arXiv:2212.08666](https://arxiv.org/abs/2212.08666)
 Cai Z., et al., 2019, *ApJS*, **245**, 23
 Cantalupo S., Arrigoni-Battaia F., Prochaska J. X., Hennawi J. F., Madau P., 2014, *Nature*, **506**, 63
 Cardelli J. A., Clayton G. C., Mathis J. S., 1989, *ApJ*, **345**, 245
 Chandrasekhar S., 1960, Radiative transfer
 Chang S.-J., Lee H.-W., Yang Y., 2017, *MNRAS*, **464**, 5018
 Chang S.-J., Yang Y., Seon K.-I., Zabludoff A., Lee H.-W., 2023, *ApJ*, **945**, 100
 Chen Y., et al., 2020, *MNRAS*, **499**, 1721
 Chisholm J., Prochaska J. X., Schaerer D., Gazagnes S., Henry A., 2020, *MNRAS*, **498**, 2554
 Chisholm J., et al., 2021, The First Observations of the Ionizing Luminosity of Galaxies within the Epoch of Reionization, JWST Proposal. Cycle 1, ID. #1871
 Churchill C. W., Charlton J. C., 1999, *AJ*, **118**, 59
 Claeysens A., et al., 2019, *MNRAS*, **489**, 5022
 Crighton N. H. M., Hennawi J. F., Simcoe R. A., Cooksey K. L., Murphy M. T., Fumagalli M., Prochaska J. X., Shanks T., 2015, *MNRAS*, **446**, 18
 Dijkstra M., 2014, *Publ. Astron. Soc. Australia*, **31**, e040
 Dijkstra M., Loeb A., 2008, *MNRAS*, **391**, 457
 Dijkstra M., Gronke M., Venkatesan A., 2016, *ApJ*, **828**, 71
 Dijkstra M., Prochaska J. X., Ouchi M., Hayes M., eds, 2019, Lyman-alpha as an Astrophysical and Cosmological Tool Saas-Fee Advanced Course Vol. 46, doi:10.1007/978-3-662-59623-4_1.
 Draine B. T., 2003a, *ARA&A*, **41**, 241
 Draine B. T., 2003b, *ApJ*, **598**, 1017

- Draine B. T., Lee H. M., 1984, *ApJ*, **285**, 89
- Dutta R., et al., 2023, *MNRAS*, **522**, 535
- Duval F., Schaerer D., Östlin G., Laursen P., 2014, *A&A*, **562**, A52
- Eide M. B., Gronke M., Dijkstra M., Hayes M., 2018, *ApJ*, **856**, 156
- Eldridge J. J., Stanway E. R., 2022, *ARA&A*, **60**, 455
- Faucher-Giguere C.-A., Oh S. P., 2023, *arXiv e-prints*, p. [arXiv:2301.10253](https://arxiv.org/abs/2301.10253)
- Faucher-Giguere C.-A., Kereš D., Dijkstra M., Hernquist L., Zal-darriaga M., 2010, *ApJ*, **725**, 633
- Flury S. R., et al., 2022a, *ApJS*, **260**, 1
- Flury S. R., et al., 2022b, *ApJ*, **930**, 126
- Fox A. J., Ledoux C., Petitjean P., Srianand R., 2007, *A&A*, **473**, 791
- Fox A. J., Prochaska J. X., Ledoux C., Petitjean P., Wolfe A. M., Srianand R., 2009, *A&A*, **503**, 731
- González Lobos V., et al., 2023, *A&A*, **679**, A41
- Grevesse N., Sauval A. J., 1998, *Space Sci. Rev.*, **85**, 161
- Gronke M., 2017, *A&A*, **608**, A139
- Gronke M., Dijkstra M., 2016, *ApJ*, **826**, 14
- Gronke M., Oh S. P., 2018, *MNRAS*, **480**, L111
- Gronke M., Dijkstra M., McCourt M., Oh S. P., 2016, *ApJ*, **833**, L26
- Gronke M., Dijkstra M., McCourt M., Oh S. P., 2017, *A&A*, **607**, A71
- Gronke M., Oh S. P., Ji S., Norman C., 2022, *MNRAS*, **511**, 859
- Guo Y., et al., 2020, *ApJ*, **898**, 26
- Guo Y., et al., 2023a, *arXiv e-prints*, p. [arXiv:2309.06311](https://arxiv.org/abs/2309.06311)
- Guo Y., et al., 2023b, *Nature*, **624**, 53
- Hansen M., Oh S. P., 2006, *MNRAS*, **367**, 979
- Hayes M., Scarlata C., Siana B., 2011, *Nature*, **476**, 304
- Hayes M., Melinder J., Östlin G., Scarlata C., Lehnert M. D., Mannerström-Jansson G., 2016, *ApJ*, **828**, 49
- Hayes M. J., Runnholm A., Gronke M., Scarlata C., 2021, *ApJ*, **908**, 36
- Hennawi J. F., Prochaska J. X., 2013, *ApJ*, **766**, 58
- Henry A., Berg D. A., Scarlata C., Verhamme A., Erb D., 2018, *ApJ*, **855**, 96
- Heney L. G., Greenstein J. L., 1941, *ApJ*, **93**, 70
- Hill G. J., et al., 2021, *AJ*, **162**, 298
- Holweger H., 2001, in Wimmer-Schweingruber R. F., ed., American Institute of Physics Conference Series Vol. 598, Joint SOHO/ACE workshop “Solar and Galactic Composition”. pp 23–30 ([arXiv:astro-ph/0107426](https://arxiv.org/abs/astro-ph/0107426)), doi:10.1063/1.1433974
- Hummels C. B., et al., 2019, *ApJ*, **882**, 156
- Izotov Y. I., Schaerer D., Thuan T. X., Worseck G., Guseva N. G., Orlitová I., Verhamme A., 2016, *MNRAS*, **461**, 3683
- Izotov Y. I., Schaerer D., Worseck G., Guseva N. G., Thuan T. X., Verhamme A., Orlitová I., Fricke K. J., 2018a, *MNRAS*, **474**, 4514
- Izotov Y. I., Schaerer D., Worseck G., Guseva N. G., Thuan T. X., Verhamme A., Orlitová I., Fricke K. J., 2018b, *MNRAS*, **474**, 4514
- Izotov Y. I., Chisholm J., Worseck G., Guseva N. G., Schaerer D., Prochaska J. X., 2022, *MNRAS*, **515**, 2864
- Kafatos M., Michalitsianos A. G., Fahey R. P., 1985, *ApJS*, **59**, 785
- Karman W., et al., 2017, *A&A*, **599**, A28
- Kasen D., Branch D., Baron E., Jeffery D., 2002, *ApJ*, **565**, 380
- Katz H., et al., 2022, *MNRAS*, **515**, 4265
- Kim E., Yang Y., Zabludoff A., Smith P., Jannuzi B., Lee M. G., Hwang N., Park B.-G., 2020, *ApJ*, **894**, 33
- Kim K. J., et al., 2023, *arXiv e-prints*, p. [arXiv:2305.13405](https://arxiv.org/abs/2305.13405)
- Kulkarni G., Keating L. C., Haehnelt M. G., Bosman S. E. I., Puchwein E., Chardin J., Aubert D., 2019, *MNRAS*, **485**, L24
- Lan T.-W., Fukugita M., 2017, *ApJ*, **850**, 156
- Laursen P., Sommer-Larsen J., Razoumov A. O., 2011, *ApJ*, **728**, 52
- Laursen P., Duval F., Östlin G., 2013, *ApJ*, **766**, 124
- Leclercq F., et al., 2020, *A&A*, **635**, A82
- Leclercq F., et al., 2022, *A&A*, **663**, A11
- Li Z., Steidel C. C., Gronke M., Chen Y., 2021, *MNRAS*, **502**, 2389
- Liang C. J., Remming I., 2020, *MNRAS*, **491**, 5056
- Lujan Niemeyer M., et al., 2022a, *ApJ*, **929**, 90
- Lujan Niemeyer M., et al., 2022b, *ApJ*, **934**, L26
- Madau P., Dickinson M., 2014, *ARA&A*, **52**, 415
- Martin C., Moore A., Morrissey P., Matuszewski M., Rahman S., Adkins S., Epps H., 2010, in McLean I. S., Ramsay S. K., Takami H., eds, Society of Photo-Optical Instrumentation Engineers (SPIE) Conference Series Vol. 7735, Ground-based and Airborne Instrumentation for Astronomy III. p. 77350M, doi:10.1117/12.858227
- Mas-Ribas L., et al., 2017, *ApJ*, **846**, 4
- Mathis J. S., 1990, *ARA&A*, **28**, 37
- McCourt M., Oh S. P., O’Leary R., Madigan A.-M., 2018, *MNRAS*, **473**, 5407
- Michalitsianos A. G., Kafatos M., Fahey R. P., Viotti R., Cassatella A., Altamore A., 1988, *ApJ*, **331**, 477
- Michalitsianos A. G., Kafatos M., Meier S. R., 1992, *ApJ*, **389**, 649
- Michel-Dansac L., Blaizot J., Garel T., Verhamme A., Kimm T., Trebitsch M., 2020, *A&A*, **635**, A154
- Neufeld D. A., 1990, *ApJ*, **350**, 216
- Neufeld D. A., 1991, *ApJ*, **370**, L85
- Osterbrock D. E., 1962, *ApJ*, **135**, 195
- Ouchi M., Ono Y., Shibuya T., 2020, *ARA&A*, **58**, 617
- Prochaska J. X., Kasen D., Rubin K., 2011, *ApJ*, **734**, 24
- Prochaska J. X., et al., 2013, *ApJ*, **776**, 136
- Ranjan A., et al., 2022, *A&A*, **661**, A134
- Rickards Vaught R. J., Rubin K. H. R., Arrigoni Battaia F., Prochaska J. X., Hennawi J. F., 2019, *ApJ*, **879**, 7
- Rivera-Thorsen T. E., et al., 2017, *A&A*, **608**, L4
- Rivera-Thorsen T. E., et al., 2019, *Science*, **366**, 738
- Robertson B. E., Ellis R. S., Dunlop J. S., McLure R. J., Stark D. P., 2010, *Nature*, **468**, 49
- Rubin K. H. R., Prochaska J. X., Ménard B., Murray N., Kasen D., Koo D. C., Phillips A. C., 2011, *ApJ*, **728**, 55
- Rubin K. H. R., Hennawi J. F., Prochaska J. X., Simcoe R. A., Myers A., Lau M. W., 2015, *ApJ*, **808**, 38
- Rupke D., 2018, *Galaxies*, **6**, 138
- Salim S., Narayanan D., 2020, *ARA&A*, **58**, 529
- Schroetter I., et al., 2021, *MNRAS*, **506**, 1355
- Seive T., Chisholm J., Leclercq F., Zeimann G., 2022, *MNRAS*, **515**, 5556
- Seon K.-i., 2023, *arXiv e-prints*, p. [arXiv:2310.17908](https://arxiv.org/abs/2310.17908)
- Seon K.-i., Draine B. T., 2016, *ApJ*, **833**, 201
- Seon K.-i., Kim C.-G., 2020, *ApJS*, **250**, 9
- Seon K.-i., Song H., Chang S.-J., 2022, *ApJS*, **259**, 3
- Shapley A. E., Steidel C. C., Strom A. L., Bogosavljević M., Reddy N. A., Siana B., Mostardi R. E., Rudie G. C., 2016, *ApJ*, **826**, L24
- Smith A., Kannan R., Garaldi E., Vogelsberger M., Pakmor R., Springel V., Hernquist L., 2022, *MNRAS*, **512**, 3243
- Sobolev V. V., 1960, *Moving Envelopes of Stars*, doi:10.4159/harvard.9780674864658.
- Steidel C. C., Pettini M., Adelberger K. L., 2001, *ApJ*, **546**, 665
- Steidel C. C., Erb D. K., Shapley A. E., Pettini M., Reddy N., Bogosavljević M., Rudie G. C., Rakic O., 2010, *ApJ*, **717**, 289
- Steidel C. C., Bogosavljević M., Shapley A. E., Kollmeier J. A., Reddy N. A., Erb D. K., Pettini M., 2011, *ApJ*, **736**, 160
- Steidel C. C., Bogosavljević M., Shapley A. E., Reddy N. A., Rudie G. C., Pettini M., Trainor R. F., Strom A. L., 2018, *ApJ*, **869**, 123
- Travascio A., et al., 2020, *A&A*, **635**, A157
- Tumlinson J., Peebles M. S., Werk J. K., 2017, *ARA&A*, **55**, 389
- Vanzella E., et al., 2016, *ApJ*, **825**, 41
- Vanzella E., et al., 2018, *MNRAS*, **476**, L15

- Veilleux S., Cecil G., Bland-Hawthorn J., 2005, *ARA&A*, **43**, 769
 Veilleux S., Maiolino R., Bolatto A. D., Aalto S., 2020, *A&ARv*, **28**, 2
 Verhamme A., Schaerer D., Maselli A., 2006, *A&A*, **460**, 397
 Verhamme A., Schaerer D., Atek H., Tapken C., 2008, *A&A*, **491**, 89
 Verhamme A., Orlitová I., Schaerer D., Hayes M., 2015, *A&A*, **578**, A7
 Weng S., et al., 2023, *MNRAS*, **523**, 676
 Wisotzki L., et al., 2016, *A&A*, **587**, A98
 Wisotzki L., et al., 2018, *Nature*, **562**, 229
 Wright E. L., 2006, *PASP*, **118**, 1711
 Xu X., et al., 2023, *ApJ*, **943**, 94
 Yoo J. J., Lee H.-W., Ahn S.-H., 2002, *MNRAS*, **334**, 974
 You C., et al., 2017, *ApJ*, **834**, 182
 Zabl J., et al., 2021, *MNRAS*, **507**, 4294
 Zheng Z., Miralda-Escudé J., 2002, *ApJ*, **578**, 33
 van de Voort F., Springel V., Mandelker N., van den Bosch F. C., Pakmor R., 2019, *MNRAS*, **482**, L85

APPENDIX A: ESCAPE FRACTION BY DIFFERENT DUST MODELS

Fig. A1 shows the escape fractions of Mg II and Ly α , denoted as $f_{\text{esc,MgII}}$ and $f_{\text{esc,Ly}\alpha}$, respectively, as a function of the dust absorption optical depth $\tau_{\text{d,abs}}$ of Mg II. Three different dust models are considered: Milky Way (MW), Large Magellanic Cloud (LMC), and Small Magellanic Cloud (SMC) dust models, as described in Draine (2003a,b). The ratio of $\tau_{\text{d,abs}}$ between Ly α and Mg II, $\tau_{\text{d,abs}}(\text{Ly}\alpha)/\tau_{\text{d,abs}}(\text{MgII})$, is 2.53, 3.79, and 9.26 for the MW, LMC, and SMC dust models, respectively. $f_{\text{esc,Ly}\alpha}$ decreases with increasing $\tau_{\text{d,abs}}(\text{Ly}\alpha)/\tau_{\text{d,abs}}(\text{MgII})$.

Fig. A2 shows a comparison between $f_{\text{esc,Ly}\alpha}$ and $f_{\text{esc,MgII}}$, assuming $N_{\text{MgII}}/N_{\text{HI}} = 10^{-5.5}$. Since the path length of Ly α is typically larger than that of Mg II due to the significantly higher column density of H I compared to Mg II (i.e., $N_{\text{HI}} \gg N_{\text{MgII}}$), $f_{\text{esc,Ly}\alpha}$ is generally smaller than $f_{\text{esc,MgII}}^\beta$, where β is $\tau_{\text{d,abs}}(\text{Ly}\alpha)/\tau_{\text{d,abs}}(\text{MgII})$ for each dust model. However, it is important to note that in a clumpy medium, the trend can be changed, as discussed in Fig. 26 and § 6.1.

This paper has been typeset from a $\text{\TeX}/\text{\LaTeX}$ file prepared by the author.

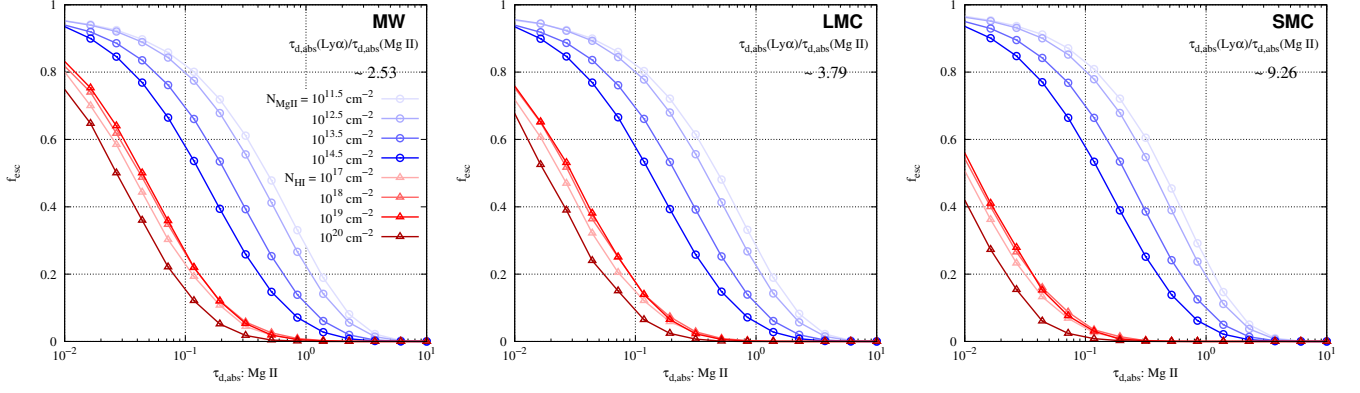


Figure A1. Escape fractions f_{esc} of Mg II (blue) and Ly α (red) for three types of dust models: MW (left), LMC (center), and SMC (right). The model composed of a central source and homogeneous medium considers the monochromatic source ($\sigma_{\text{src}} = 0 \text{ km s}^{-1}$), the static medium ($v_{\text{exp}} = 0 \text{ km s}^{-1}$), and the thermal speed as the random motion of scattering medium ($\sigma_{\text{R}} = v_{\text{th}}$). The x -axis is the dust absorption optical depth of Mg II near 2800 Å. The shade of color represents various N_{HI} & N_{MgII} assuming $N_{\text{MgII}}/N_{\text{HI}} = 10^{-5.5}$.

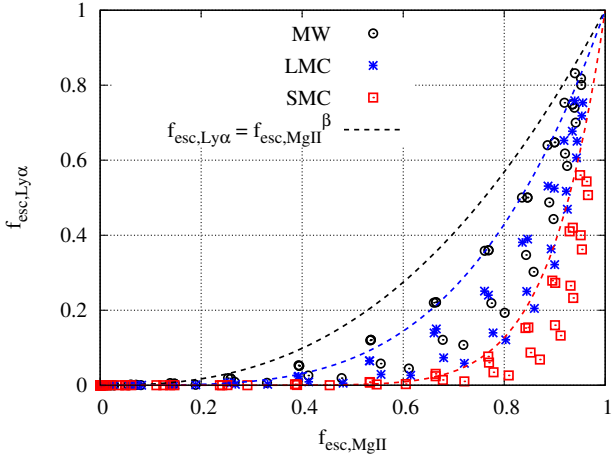


Figure A2. f_{esc} of Mg II and Ly α , $f_{\text{esc,MgII}}$ and $f_{\text{esc,Ly}\alpha}$ in Fig. A1. The colors represent the dust models: MW (black), LMC (blue), and SMC (red). The dashed lines represent $f_{\text{esc,Ly}\alpha} = f_{\text{esc,MgII}}^\beta$, where β is the ratio of dust absorption optical depth of Ly α and Mg II, $\tau_{\text{d,abs}}(\text{Ly}\alpha)/\tau_{\text{d,abs}}(\text{Mg II})$, shown in Fig. A1. β is 2.53, 3.79, and 9.26 for the MW, LMC, and SMC dust models, respectively.